

On the dynamics of the flagellar beat under load

Dissertation

zur Erlangung des Grades
des Doktors der Naturwissenschaften
der Naturwissenschaftlich-Technischen Fakultät
der Universität des Saarlandes

von
Christian Ruloff

Saarbrücken
2018



Tag des Kolloquiums: 18.10.2018

Dekan: Prof. Dr. G. Kickelbick

Berichterstatter: Prof. Dr. Ch. Wagner

Prof. Dr. R. Seemann

Vorsitz: Prof. Dr. R. Pelster

Akad. Mitarbeiter: Dr. A. Tschöpe

Abstract

Eukaryotic flagella are lash-like cell appendages that can actively bend in order to serve different purposes, from cell propulsion to fluid transport. A remarkable phenomenon which can be observed for beating flagella is stable synchronisation, although a central internal clock seems to be missing. By exposing the biflagellate microswimmer *Chlamydomonas reinhardtii*, whose flagella are termed *cis* and *trans* depending on their proximity to the cell's eyespot, to controlled fluid flow, we determine the phase-dependent load response of the flagellar beat which is thought to play an important role for synchronisation. Over a certain range, the beating frequency changes linearly with the applied load. If the external load exceeds a certain threshold, the flagellar beat comes to a halt. This threshold depends on the direction of the applied load and if the load is gradually increased from zero to maximum or vice versa, revealing a more or less pronounced hysteresis for *cis*- and *trans*-flagellum, individually. For intermediate load, we find two previously unknown, dynamic beating modes of *C. reinhardtii*'s flagella which occur only if the flow direction is opposite to the swimming direction with one of these new beating modes being almost exclusive to the *cis*-flagellum. In general, we observe a different behaviour of *cis*- and *trans*-flagellum under load. At last, we find that the capability for flagellar synchronisation depends on the strength and the direction of the applied load.

Zusammenfassung

Eukaryotische Flagellen sind fadenartige Zellausstülpungen, die sich aktiv verbiegen können und von der Fortbewegung von Zellen bis hin zum Flüssigkeitstransport unterschiedlichen Zwecken dienen. Ein erstaunliches Phänomen, das man bei schlagenden Flagellen beobachten kann, ist deren stabile Synchronisation, wiewohl ein zentraler Taktgeber zu fehlen scheint. Indem wir *Chlamydomonas reinhardtii*, einen Mikroschwimmer, dessen Flagellen abhängig von ihrer Nähe zum Augenfleck als *cis*- und *trans*-Flagellum bezeichnet werden, kontrollierten Flüssen aussetzen, können wir die Lastantwort des Flagellenschlags, welche eine wichtige Rolle für die Synchronisation spielt, bestimmen. In einem gewissen Bereich ändert sich die Frequenz des Flagellenschlags linear mit der angelegten Last. Überschreitet die Last einen bestimmten Schwellenwert, der sowohl von der Richtung der angelegten Last als auch davon abhängt, ob die Last schrittweise von Null auf das Maximum erhöht wird oder umgekehrt, so kommt der Flagellenschlag zum Erliegen. Ebenso zeigen *cis*- und *trans*-Flagellum eine mehr oder weniger stark ausgeprägte Hysterese. Im Bereich mittlerer Last finden wir zwei bisher unbekannte, dynamische Schlagmoden, sofern die Zelle entgegen der Flussrichtung schwimmt, wobei eine Schlagmode fast ausschließlich für das *cis*-Flagellum beobachtet werden konnte. Außerdem hängt die Fähigkeit zur Synchronisation des Flagellenschlags sowohl von der Richtung als auch von der Stärke der angelegten Last ab.

Eidesstattliche Versicherung

Hiermit versichere ich an Eides statt, dass ich die vorliegende Arbeit selbstständig und ohne Benutzung anderer als der angegebenen Hilfsmittel angefertigt habe. Die aus anderen Quellen oder indirekt übernommenen Daten und Konzepte sind unter Angabe der Quelle gekennzeichnet. Die Arbeit wurde bisher weder im In- noch im Ausland in gleicher oder ähnlicher Form in einem Verfahren zur Erlangung eines akademischen Grades vorgelegt.

Ort, Datum

Christian Ruloff

Contents

1 Eukaryotic flagella	1
Life at low Reynolds number and the scallop theorem	2
The model organism <i>Chlamydomonas reinhardtii</i>	3
The structure of the eukaryotic flagellum	5
A closer look at synchronisation mechanisms	7
Previous work	9
Dynamics of the flagellar beat under load	10
2 Materials and methods	13
2.1 Algae cultivation and culture handling	14
2.2 Micropipettes apparatus for flagellar dynamics experiments	15
Device control toolbox for measurement automation	15
Microscope and illumination	16
Micropipettes	16
Image acquisition	18
Pressure controller calibration	19
2.3 Design, fabrication, and calibration of the microfluidics chip	21
Navier-Stokes equations for homogeneous, incompressible fluids	21
Pressure driven flow in a rectangular duct	22
Microfluidics chip design	23
Microfluidics fabrication	26
Microfluidics calibration	28
3 Flagellar beating under load	33
3.1 Phase-dependent load response of the eukaryotic flagellum	33
3.1.1 Data evaluation	34
Cell body tracking	34
Full flagellar tracking	35
Phase-dependent tracking performance	38
3.1.2 Measurement protocol	39
Quality standards	40
3.1.3 Principle component analysis and limit cycle representation	40
Flow induced changes in phase speed and amplitude	43
3.1.4 Theoretical model for flagellar oscillations	44
3.1.5 Phase speed susceptibility and amplitude susceptibility	47
3.1.6 Efficiency of the flagellar beat	49
3.1.7 Comparison of eukaryotic flagella with a combustion engine	50

3.2	Dynamic modes of flagellar beating	50
	Tremor-like beating	52
	Chiral beating	54
3.2.1	Data evaluation	54
	Minimal flagellar tracking	54
	Processing of tracking data	55
	Determination of the flagellar beating frequency	56
3.2.2	Measurement protocol	58
3.2.3	The change in beating frequency under load	59
3.2.4	Phase diagram of the dynamic beating modes	62
3.2.5	Stalling behaviour of the flagellar beat under high load	65
	<i>Cis</i> - and <i>trans</i> -flagellum differ in stalling behaviour	66
	Hysteresis of flagellar stalling	67
3.3	Flagellar synchronisation	69
	Phase slip dynamics	71
	Load-dependent flagellar coupling	72
	Flagellar synchronisation of nearby swimming cells	73
3.4	Discussion	76
	High-precision flagellar tracking is required	76
	A more realistic model for flagellar beating	77
	The load response is phase-dependent	77
	Load direction and strength dictate beating frequency and stalling	78
	Hysteresis in flagellar stalling due to different stalling states	78
	Previously unknown flagellar beating modes emerge under load	79
	External load influences flagellar synchronisation	79
	Hydrodynamic interactions dominate over intracellular coupling	80
	Conclusion	80
4	Outlook	81
	Dynamic response of the flagellar beat to sudden load	81
	Variation of hydrodynamic interactions	82
	Influence of basal body movement on synchronisation	83
	Experiments with mutants of <i>C. reinhardtii</i>	84
	Technical enhancements to the experimental setup	84
	Bibliography	85

List of author's publications

- ▷ G. S. KLINDT *, C. RULOFF *, C. WAGNER, AND B. M. FRIEDRICH
Load Response of the Flagellar Beat
Physical Review Letters, 117 (2016)
* equal contribution
- ▷ G. S. KLINDT, C. RULOFF, C. WAGNER, AND B. M. FRIEDRICH
In-phase and anti-phase flagellar synchronization by waveform compliance and basal coupling
New Journal of Physics, 19 (2017), p. 113052
- ▷ D. FLORMANN, O. AOUANE, L. KAESTNER, C. RULOFF, C. MISBAH, T. PODGORSKI,
AND C. WAGNER
The buckling instability of aggregating red blood cells
Scientific Reports, 7 (2017), p. 7928

1

Eukaryotic flagella

In nature, it is the ability to move that, besides minor other biological facts, separates living creatures from dead objects. From microorganisms to animals and human beings, they all need to be able to, e.g., flee from predators, search for food, or simply move things around in order to survive. To serve this purpose, humans are equipped with arms, legs, and hands, and some animals have pads, while others have fins, just to name a few. Even down to the microscale, evolution has equipped these organisms with a slightly different yet comparable versatile tool called eukaryotic flagella or cilia [2]. These are 10–100 μm long, lash-like cell appendages which can actively bend with a beating frequency of 10–100 Hz [43] in order to serve different purposes, from cell propulsion to fluid transport [9]. Their cytoskeletal core, the axoneme, is a complex machine on a very small scale which has been conserved throughout evolution [27, 95]. Unicellular microorganisms like algae, protozoa, and sperm use eukaryotic flagella for cell propulsion, while cilia can be found in plants and animals, and thus humans, as well, mainly with the purpose of fluid transport. It is noteworthy that, besides the so far mentioned active flagella, non-motile cilia and flagella, whose purpose is the transduction of a multitude of stimuli [80, 83], exist as well.

Flagella and cilia can be found at various places in the human body, from ependymal cilia in the brain to cilia in the respiratory tract or the reproduction system [55, 77]. The term flagellum is usually used for long cilia and if only a small number is referred to, while the term cilia is used if the cell appendages are relatively short and occurring collectively, usually within the scope of cilia carpets on epithelial surfaces. In this case, collections of cilia phase-lock to a common frequency due to long-range hydrodynamic interactions [45, 63, 67, 88, 104, 128, 129] leading to spatio-temporal synchronisation pattern. These pattern are called metachronal waves by which mechanical work can be applied to the surrounding fluid enabling efficient fluid transport [31], e.g., in order to pump cerebrospinal fluid in the brain [137], transport mucus in the airways [71, 114] and expel pathogens [23], or establish circulating flows during embryonic development leading to the left-right asymmetry in the mammalian body plan [26, 89, 90]. This coordinated beating can be observed despite active noise [39, 78, 99].

Paramecium [85, 85] and *Volvox* [19, 20], so called microswimmer, are also equipped with a multitude of flagella which they use for cell propulsion (fig. 1.1.(a–b)). However, multiple flagella are not necessary for microorganism to swim. Sperm

cells are usually equipped with only a single flagellum beating in a whip-like fashion while *Chlamydomonas reinhardtii* (fig. 1.1.(c)), a unicellular green alga, has two eukaryotic flagella [82] beating in a breaststroke-like manner [119]. These breaststrokes are perfectly synchronised for long time periods, only occasionally interrupted by phase slips during which the flagella lose their synchrony and the cell changes its swimming direction. This behaviour is astonishing given the fact that an internal clock for synchronisation is missing.

Basically, the beating flagellum is a micro-mechanical oscillator. A dynamic instability in the collective dynamics of $10^4 - 10^5$ molecular dynein motors, which are regularly spread along the flagellar axoneme, and elastic, cross-linking filaments generates regular bending waves [12, 24, 57, 87]. These waves can be observed even in the case of isolated flagella in the presence of *adenosine triphosphate* (ATP) [4, 11, 14, 37, 54]. In this context, isolated means that the cell body and the membrane around the flagellum have been chemically removed. The self-organised motor dynamics, the regulation mechanisms of the motor [105, 115, 116], and the way they respond to external forces are subject to both recent publications [49] and this work.

Life at low Reynolds number and the scallop theorem. In order to better understand the fundamental difference between swimming as we know it and swimming on the microscale, consider the following example: A fish swimming in water uses its tail fin for propulsion. Taking a closer look at the exact moving pattern of the fin, we directly see that it is symmetric in time, i.e., we cannot distinguish if a recording of the moving fin is played back regularly or in reverse. If we now downscale the fish to a swimmer of only several micrometer in size which is swimming with a velocity of several micrometer per second, but retain water as the surrounding medium, time-reversible strokes do not lead to any movement of this downscaled fish anymore.

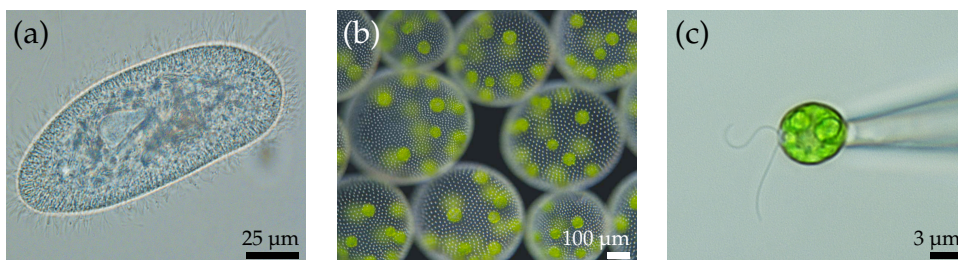


Fig. 1.1: (a) Brightfield image of *Paramecium caudatum*, taken from [69] (modified), (b) darkfield image of *Volvox carteri*, taken from [47] (modified), and (c) brightfield image of *Chlamydomonas reinhardtii*, taken by the author himself.

Another example is the scallop which generates net propulsion by slowly opening its shells, immediately followed by rapidly closing them again, thus pushing water backward and, consequently, the scallop forward. During the subsequent opening of its shells, the scallop floats through the water due to inertia. However, a microswimmer performing this kind of motion would simply move forward during the closing of the shells, but return to its original position on opening the shells again. On the microscale, inertia does not play a role at all and viscous forces govern the equations of motion.

The Reynolds number, a dimensionless quantity which can be derived from the Navier-Stokes equations via nondimensionalisation, is defined as the ratio between inertial forces and viscous forces. For microswimmers of characteristic size $l = 10 \mu\text{m}$ which are swimming at a velocity $u = 100 \mu\text{m/s}$ in a fluid of density $\rho = 1000 \text{kg m}^{-3}$ and viscosity $\mu = 1 \text{mPa s}$, the Reynolds number, defined as $Re = \rho lu / \mu$, typically in the order of $Re = 10^{-3}$. On the microscale, we are in the low Reynolds number regime where inertia is negligible [32, 71] while viscous forces govern the fluid flow [125]. This means that as soon as the swimming motion stops, the swimmer stops immediately as well.

In the regime of low Reynolds number, the Navier-Stokes equations—the equations which describe fluid flow—simplify to the time reversible Stokes equations. Therefore, it is mandatory for microorganisms to break this time-reversibility by non-reciprocal shape changes in order to gain net propulsion [7, 120], e.g., by means of periodic bending waves [9, 16, 44]. This requirement is also known as the scallop theorem [101], named for the impossibility of a microscale scallop to swim in the low Reynolds number regime.

The model organism *Chlamydomonas reinhardtii*. Over the last decades, the unicellular green alga *C. reinhardtii* has become the model system when it comes to addressing fundamental biological questions like “How do cells move?” or more specific physical questions like “How do microswimmers synchronise their flagellar beat?” [36, 39–41, 66, 73, 103, 108, 111]. *C. reinhardtii* is $\approx 8 \mu\text{m}$ in size and has a slightly prolate shape. With its two flagella, which are $\approx 10 \mu\text{m}$ in length, *Chlamydomonas reinhardtii* is an ideal candidate for studying synchronisation on a single-cell level. Performing a breaststroke-like beating pattern, see fig. 1.2 and [107], at frequencies of $\approx 50 \text{Hz}$, *C. reinhardtii* swimming speed lies between $30 \mu\text{m/s}$ and $110 \mu\text{m/s}$, depending on the strain. Both flagella are beating in slightly different planes which leads to a rotation about the swimming direction with 2Hz . *Chlamydomonas reinhardtii* is equipped with a light-sensing organelle, the so called eyespot. The flagellum closest to the eyespot is called *cis*-flagellum, the other one is termed *trans*-flagellum. The eyespot can indirectly control the Ca^{2+} concentration in the flagella. In general, the cell responds to this light stimulus and

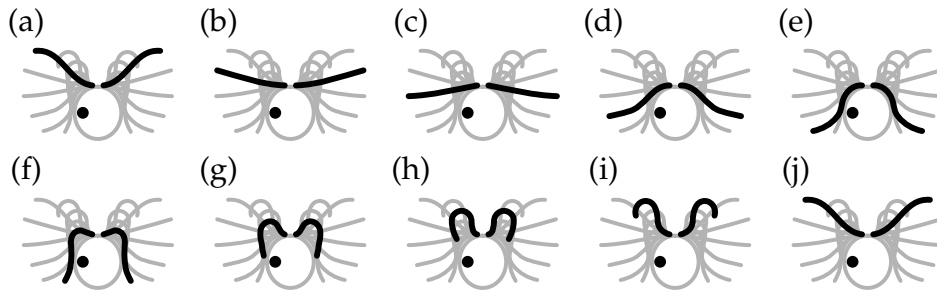


Fig. 1.2: The breaststroke-like beating pattern of *Chlamydomonas reinhardtii*'s eukaryotic flagella consists of the so called power stroke (a–e) during which the cell moves forward, immediately followed by the so called recovery stroke (f–j) during which the cell moves a bit backward again. The position of the eyespot (black dot) defines the *cis*-flagellum which is closest to the eyespot, and the *trans*-flagellum.

the altered Ca^{2+} concentration with an identical change in beating frequency of both flagella [109], also known as photoresponse. Albeit the frequency response is identical, the flagellar waveform changes differently for *cis*- and *trans*-flagellum [60]. This has direct consequences for the swimming paths of *C. reinhardtii*, also known as phototaxis [6]: If the signal at the eyespot is constant, the cell is swimming towards the light source. If the cell is not heading towards a light source, the signal at the eyespot is varying due to the rotation about the long axis which leads to a modulation of the Ca^{2+} concentration. Consequently, the change in flagellar waveform leads to a change in beating strength of the *trans*-flagellum [50], reorientating the cell towards the direction of the inclining light signal. However, under strong illumination conditions, *Chlamydomonas reinhardtii* shows a so called photoshock response [96, 110] when both flagella change their waveform to one similar to the waveform observed for sperm cells, thus pushing the cell backwards and away from the light.

The swimming path of *Chlamydomonas reinhardtii* can be divided into periods when both flagella are beating in synchrony, leading to straight and fast propulsion [9], adjoined by phases of asynchronous beating where the orientation of the cell body is changing dramatically. To obtain synchrony out of an asynchronous state, the cell body is rocking back and forth, inducing hydrodynamic friction forces leading to re-synchronisation [34]. Beating in synchrony is important for the cell to swim straight and fast [99], hence the ability to desynchronise permits steering.

The beating pattern itself can be divided into two parts: the power stroke and the recovery stroke, see fig. 1.2. During the power stroke, the flagella are fully stretched, reaching out towards the front of the cell body and are then pulled back to the tail of the cell. Throughout this motion, the interaction with the surrounding fluid is highest leading to forward propulsion. The beat cycle is completed by a recovery stroke during which the flagella are drawn back close to the cell body returning

to the starting point of the power stroke. To do so, the flagella are significantly bend and pulled back close to the cell body. In principle, the flagella move in opposite direction compared to the power stroke, but here, the interaction with the surrounding medium is less compared to the power stroke. Therefore, the cell moves back, but just a little bit. Due to this asymmetry, the cell gains net propulsion in a two-step-forward-one-step-backward kind of motion.

The structure of the eukaryotic flagellum. The flagellum of sperm cells or algae is fundamentally different from the flagellum found in bacteria like *E. coli* or *B. subtilis*. They are equipped with prokaryotic flagella which are in fact rigid, hollow cylinders build up by proteins in a helical fashion. The flagellar beating is driven by a rotary motor at the basal end of the flagellum which is embedded into the cell membrane [72, 127]. The motor itself consists of protein rings located around a rod. The protein rings act as a proton pump where hydrogen ions move down a electro-chemical potential. This movement rotates the protein ring and, consequently, rotates the flagellum which is connected to the rod by means of a hook-like structure. As long as all motors of all flagella are rotating counter-clockwise, a stable, helical bundle is formed generating linear net propulsion out of rotation. If enough motors change their rotation direction to clockwise, the bundle disassembles and the bacterium tumbles.

Eukaryotic flagella are neither a hollow cylinder nor do they have a central motor. The motile core of the flagellum, the axoneme, consists of a central pair of single protein filaments, so called microtubules, surrounded by nine cylindrically arranged microtubule doublets, and is surrounded by the cell membrane [3, 95], see fig. 1.3. The outer doublets and the central pair are connected by means of central spokes made of polypeptides, while subsequent microtubule doublets are interconnected by nexin linker [87]. Dynein motor proteins, which are regularly distributed in between the doublets, render the eukaryotic flagellum an active organelle [87, 88]. Two kinds of dynein motor proteins, called inner and outer arms, are fixed on one side to one microtubule doublet, but can change their configuration by means of ATP hydrolysis [79], thus walking along the subsequent microtubule doublet.

Therefore, subsequent microtubules would in fact slide along each other [3, 13, 15, 122]. Since the flagella are anchored at the basal body [30, 117], and nexin linker interconnect the microtubules [17], this suppressed sliding generates stresses and strains in the flagellum and, consequently, bends it. This bending and the accompanying deformation of the axoneme mechanically feeds back to the dynein motors by altering their attachment and detachment rates, thus influencing the further motor activity. In turn, new stresses and strains are generated in the flagellum, and its shape changes again.

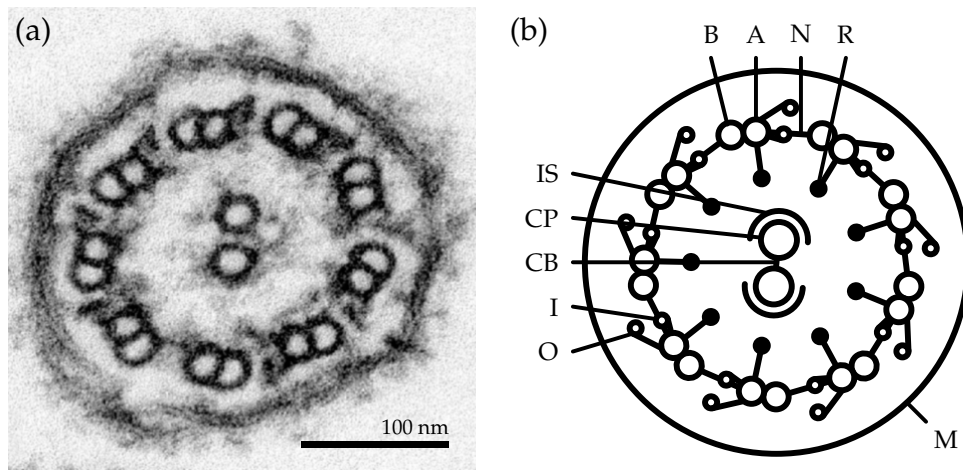


Fig. 1.3: (a) Electron micrograph of the flagellum of *C. reinhardtii*, taken from [95] with overlays inserted by the author, and (b) a sketch of the cross-section of a flagellum: The nine microtubule doublets, each composed of the A tubule (A) and the B tubule (B), surround the central pair (CP). The central pair is interconnected by the central bridge (CB) and shielded by the inner sheath (IS). Radial spokes (R) connect the microtubule doublets to the central pair. Inner (I) and outer dynein arm (O) are attached to the A tubule and walk along the B tubule while nexin fibres (N) link A tubule and B tubule. The entire flagellum is enclosed in the membrane (M).

In general, increased motor activity on one side leads to bending in one direction, hence alternating axonemal bending requires switching between both sides twice per beat [118]. Albeit the mechanism of sliding to bending conversion is well established, the detailed mechanism of how dynein motors are controlled and coordinated remains unknown. In the literature, three different but not mutually exclusive models have been proposed [5]: If the dynein motors were normal-force-controlled, the detachment rate of the dynein motors depends on the transverse forces arising through bending [74, 75]. If the motors were sliding-controlled, motors are regulated by means of forces acting parallel to the microtubules. Sliding forces on one side of the flagellum dominating the sliding forces on the opposing side in a tug-of-war sense lead to a collective detachment on one side and, consequently, to flagellar bending [14, 24, 57, 105]. Finally, if dynein motors were curvature-controlled, the local curvature regulates the motor activity in a similar way to sliding control, yet the opposing sign of the curvature on opposing sides results in a comparable reciprocal inhibition [13, 17, 84].

Recently, a fourth control mechanism has been suggested which does not depend on the curvature directly but on its time derivative. While the previously mentioned models fail for some conditions, this control mechanism model, validated by experiments with reactivated flagella of *C. reinhardtii* cells [8, 54], might serve as a universal model for feedback controlled dynein motors [115, 116].

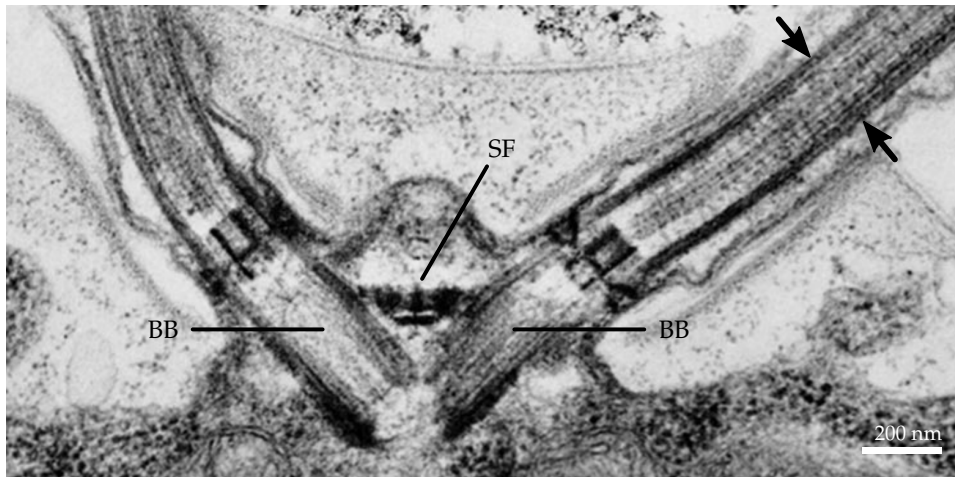


Fig. 1.4: Electron micrograph of the basal body (BB) of *C. reinhardtii* including the proximal part of its flagella. This picture was taken from [106] with overlays inserted by the author. The distal striated fibres (SF), which interconnect the flagellar bases, are known to shorten on increasing Ca^{2+} concentration [112]. The arrows, inserted by the author, shall just indicate at which position the picture in (a) could have been captured.

The multitude of beating patterns, ranging from whip-like motion of the flagella of sperm cells to breaststroke-like beating of *C. reinhardtii*'s flagella and chiral beating of the cilia carpet of *Paramecium*, is thought to depend on the concrete internal structure of the flagellum: In *Paramecium*, the central pair can rotate which leads to an out-of-plane beating—also known as chiral beating [92]. If orientation of the central pair is fixed, the resulting anisotropic bending rigidity restricts flagellar beating to one plane [22, 38].

Stellate fibres [124] anchor each flagellum to its corresponding basal body which is in turn connected to the cell's nucleus [124]. As shown in fig. 1.4, both basal bodies are interconnected by 300 nm long and 75 nm thick contractile fibres, so called distal striated fibres [106], that can change their length up to 50 nm [106] within milliseconds due to the Ca^{2+} modulated contractile protein centrin [52, 81, 112, 138]. The distal striated fibres might, besides being another candidate for setting the bending plane [54, 81], also have an impact on flagellar synchronisation: If the flagella are out-of-sync, the fibres might rhythmically contract to re-sync the flagellar beat.

A closer look at synchronisation mechanisms. Since the eukaryotic flagellum is a micro-mechanical oscillator, we can take a closer look at synchronisation mechanisms by studying synchronicity of the simplest kind of oscillators, meaning harmonic oscillators. A perfect, classical example for harmonic oscillators are pendulum clocks.

In the late 17th century, the Dutch physicist Christiaan Huygens observed that two pendulum clocks, which are hanging next to each other, will, within 30 minutes, synchronise in such a way that their pendula swing in opposite direction. The root cause for their synchronisation—synchronisation by exchange of sound pulses—remained unclear until recently [91]. Among other things, Huygens himself proposed that the pendula couple by the surrounding air, yet this theory could be proven wrong experimentally soon after. Another example for spontaneous synchronisation, both in-phase and anti-phase, can be observed for metronomes that are standing on the potentially movable beam [94]. Here, synchronisation is mediated by slight movements of the beam that feed back on the metronomes.

A simple analogy for the beating flagella would be the picture of metronomes on a supporting beam, immersed in a fluid like honey. We can use the knowledge on how this classical system synchronises to understand the synchronisation mechanism of coupled flagella: Since the flagella are fixed by their basal bodies to the cell body or the epithelial surface, flexibility in the basal bodies or cross-connections between the basal bodies, e.g., the distal striated fibres in *C. reinhardtii* [30], may lead to synchronised flagellar beating. However, albeit proven wrong in the classical example of pendulum clocks, since the surrounding medium has changed from air to a liquid, hydrodynamic interactions, here in the low Reynolds number regime, have been suggested to cause synchronisation [44]: The flagellum sets the surrounding medium in motion which in turn influences the beating of the second flagellum, and vice versa. Recently, it was experimentally proven that this mechanism indeed leads to synchronisation of the flagellar beat [41]. Using two individual, micropipettes-fixed somatic cells of *Volvox*, it could be shown that the synchronisation strength between their flagella decreases when their relative distance is increased [21]. The emergence of metachronal waves on the surface of *Volvox* cells [20] as well as the synchronised beating of nearby swimming sperm cells [136] support the theory of direct hydrodynamic synchronisation [46, 93].

Without further knowledge, both synchronisation mechanisms—hydrodynamic interactions and basal body coupling—might be, not mutually exclusively, responsible for flagellar synchronisation. Yet, the distal striated fibres connecting both basal bodies of *Chlamydomonas reinhardtii*'s flagella have proven to be a prerequisite for in-phase synchronisation [132] and experiments exposing *C. reinhardtii* to a strong oscillatory flow [103] revealed that the hydrodynamic coupling is not strong enough to force synchronisation. Especially the influence of the striated distal fibers, fibres that connect the bases of the flagella to each other, is worth investigating since even an isolated flagella apparatus, i.e., basal body and flagella, but no cell body, is able to show synchronised flagellar beating [54].

Previous work. Flagellar beating and especially their underlying synchronisation mechanism is a lively area of research since years. In order to put this work into context, I will provide a short overview of the most influential publications.

- ▷ **Noise and synchronisation in pairs of beating eukaryotic flagella [39]:** In this work, single *Chlamydomonas reinhardtii* cells are fixed by means of micropipettes in order to investigate the flagellar beat. Using high-speed video microscopy, movies of fixated cells are recorder for up to 3 min, thus providing good statistics on the dynamics of the flagellar beat. The synchronisation periods in *C. reinhardtii*'s eukaryotic flagella are interrupted by phase slips. In this work, the authors show that a low-dimensional stochastic model which is basically the stochastic Adler equation for the flagellar phase difference, can indeed predict the phase slip dynamics, the average length of the periods during which the flagella of *C. reinhardtii* beat in synchrony as well as the intrinsic phase lag during in-phase synchronised beating. Here, the magnitude of noise in the system is defined by intrinsic fluctuations of the flagellar beat itself. The flagellar coupling strength is in good agreement with expected values in case of sole hydrodynamic interactions between the flagella.
- ▷ **Flagellar synchronization independent of hydrodynamic interactions [34], Cell-body rocking is a dominant mechanism for flagellar synchronization in a swimming alga [36]:** In the first, theoretical work, a three-sphere toy model swimmer mimicking *C. reinhardtii* is developed. Two spheres, revolving on circular trajectories, represent the flagella while the third, equally-sized sphere represents the cell body. Local hydrodynamic friction forces due to the motion of the swimmer itself lead to synchronisation of the sphere-modelled flagella. However, this model works in the case of restrained motion of the swimmer due to, e.g., micropipettes fixation, as long as a certain flexibility at the flagellar base is allowed. In the follow up publication, the theory was validated by high-speed recordings of free swimming *C. reinhardtii*.
- ▷ **Flagellar synchronization through direct hydrodynamic interactions [21]:** In this work, the authors show that flagella can indeed synchronise by means of hydrodynamic interactions. Therefore, two somatic cells, isolated from *Volvox carteri* colonies, were individually fixed by micropipettes, kept at a certain distance, and recorded using high-speed imaging. Each somatic cell has two flagella which beat in perfect synchrony and are thus treated as an entity. However, differences in beating frequency exist for individual cells. Since each flagellar pair belongs to an individual cell, intracellular biochemical as well as elastic or mechanical coupling are eliminated. Both in-phase and anti-phase configurations were realised. On close proximity, robust synchrony occurs, despite the intrinsic differences in beating frequency. Precise tracking of the flagella reveals a characteristic shift in the flagellar waveform due to hydrodynamic

interactions, hence supporting synchronisation mechanisms based on waveform compliance. The interflagellar coupling strength, determined by means of these experiments, is in good agreement with predictions based on hydrodynamic interactions.

- ▷ **Hydrodynamics versus intracellular coupling in the synchronization of eukaryotic flagella [103]:** Single, micropipettes-held *C. reinhardtii* cells are exposed to controlled, oscillating flows. In order to test for the basal body, specifically the distal striated fibres, being responsible for synchronisation, both wild-type *C. reinhardtii* and the mutant *vfl3*, who has defective distal striated fibres, are investigated. Hydrodynamic forces, necessary to phase lock the flagellar beat to the oscillatory flow, are more than an order of magnitude larger than they can be found in physiological conditions. The fact that the mutant shows no in-phase synchronisation highlights that the elasticity of the distal striated fibres, or other elastic structures in the basal body, are crucial for synchronisation.

The current research in the field of flagellar synchronisation is pretty controversial, as this literature overview, sorted by the year of publication, shows: Some claim they have found the source of flagellar synchronisation in hydrodynamic interactions, others prove them partially wrong, later others support hydrodynamic interactions again and finally, distal striated fibres at the flagellar bases are thought to be the most probable candidate leading to synchronisation. However, there are more than enough good arguments that both hydrodynamic interactions and basal body coupling are responsible for synchronisation, yet under different conditions.

Dynamics of the flagellar beat under load. In this work, we want to provide some insights into this topic. Therefore, we teamed up with Gary S. Klindt and Benjamin M. Friedrich from the Max Planck Institute for the physics of complex systems in Dresden to investigate flagellar dynamics and synchronisation in a both experimental and theoretical project, which led to two publications, see [65, 66]. In order to understand flagellar synchronisation better, we focused on the load response of the flagellar beat which is a critical point for synchronisation due to hydrodynamic interactions. Hydrodynamic interactions, i.e., in this case the ability of one flagellum to influence the motion other flagella, consequently means that fluid is set in motion which then feeds back on the beating of the other flagella and vice versa. Albeit having a certain stiffness, the eukaryotic flagellum is indeed a flexible object. An external fluid flow, be it induced by another flagellum or a simple background flow, is in fact a mechanical force acting on the flagellum and possibly deforming it. Thereby, it could alter the shape of the flagellar beat as well as have an effect on the speed of the flagellar motion depending on the direction of the flow with respect to the current motion of the flagellum within the beat cycle.

Additionally, we found that flagella show interesting responses if they are exposed to fluid flow conditions far away from what they are faced with in nature. In nature, the cell would simply travel with the streamline of the fluid flow leading to almost no forces or shear on the flagella, yet here, in our highly artificial case, the cell is not flushed away by the strong flow rather than held in place by means of micropipettes. Therefore, the molecular motors and the entire flagellar structure have to work under previously unknown conditions which led to new and surprising shape and frequency responses: we observed a load-dependent response in flagellar beating frequency up to stalling of the flagellar beat, and a hysteretic behaviour between entering and leaving the stalling state due to two different kinds of flagellar stalling which we also observed. Furthermore, we found two previously unknown flagellar beating modes which we call tremor-like beating and chiral beating, the latter being almost exclusive to the *cis*-flagellum. Additionally, all of these effects strongly depend on the load direction and whether we are observing a *cis*- or a *trans*-flagellum, respectively.

By gaining more knowledge on this manifold, dynamic response of the flagellar beat to different load conditions, we imagine to be able to get new insights on how the molecular motors inside the eukaryotic flagellum power and regulate the flagellar beat.

2

Materials and methods

Chlamydomonas reinhardtii cells are very motile if they have been cultivated under optimal conditions. In order to observe its two flagella over a long time to investigate the influence of a constant, homogeneous flow on the flagellar beating, individual *C. reinhardtii* cells are fixed by means of micropipettes. Micropipettes are tiny glass capillaries which are used, e.g., for in-vitro fertilisation, to study the viscoelastic properties of red blood cells [56], or—like in this work—to attach algae on its tip for reliable fixation and orientation [108]. When working with living cells, maintaining optimal conditions throughout the entire measurement is mandatory, and being fixed by means of micropipettes is certainly not an optimal condition. Over time, cell viability is reduced and mostly, cells die after approximately 1 h. Therefore, automation, realised by the author in terms of a device control toolboxes written in MATLAB[®], is the key factor to avoid delays or errors due to user input and to perform the measurements as fast and as reliable as possible.

A micropipettes' setup, developed by the author from scratch as a set-top addition to an inverted microscope, is used to keep single *Chlamydomonas reinhardtii* cells in place. Then, the cell was placed inside a specifically designed and fabricated microfluidics channel in order to impose a certain hydrodynamic load on the flagella of *C. reinhardtii*. This means that the flagella are exposed to a certain flow velocity which is controlled by means of a pressure controller. Since changes in pressure propagate in the fluid at the speed of sound, the settling time is very low. Yet, in order to relate pressure to flow velocity, knowledge of the hydraulic resistance and, therefore, calibration is mandatory. However, controlling the flow velocity directly by means of a syringe pump is not an alternative. Albeit calibration is not required in this case, compressibility of, e.g., the connection tubes or even the fluid itself, no matter how small, significantly slows down the equilibration of the flow velocity. Thus, its settling time is in the order of minutes instead of milliseconds. Using high-speed image acquisition, flagellar dynamics are recorded with high temporal resolution. As a future use-case, the setup is designed by the author to host a second micropipette enabling interaction and synchronisation measurements between two nearby swimming cells as well.

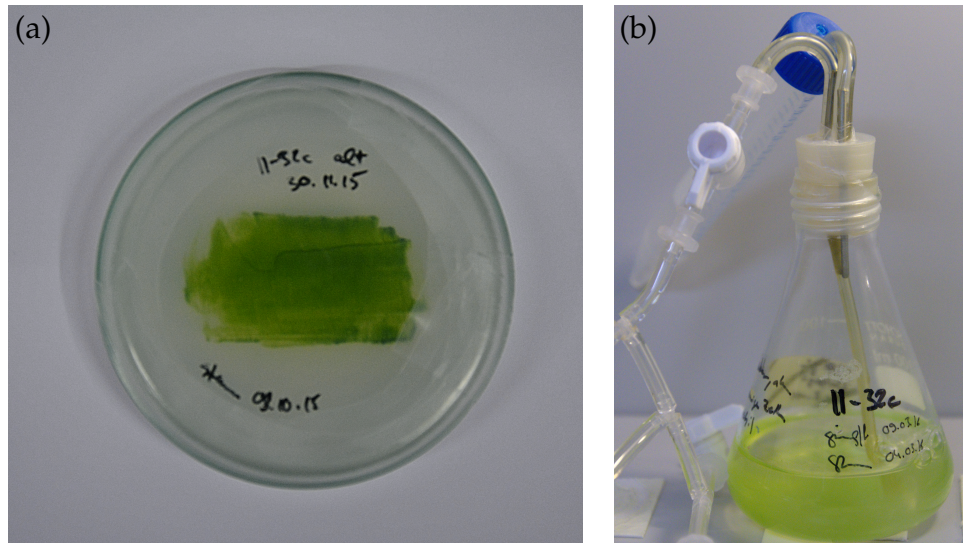


Fig. 2.1: Cultivation of *C. reinhardtii* on solid medium (a) and in liquid medium under constant air bubbling (b).

2.1 Algae cultivation and culture handling

C. reinhardtii were cultivated on agar-solidified *tris(hydroxymethyl)aminomethane acetate phosphate* (TAP) medium [42], see fig. 2.1.(a), using a day/night cycle of 16h/8h. Over daytime, the ambient temperature is 24 °C due to the illumination of two compact fluorescent lamps (11 W, 2700 K, 630 lm). During the night period, the ambient temperature drops to 21 °C. Prior to experiments, cells were remobilised and allowed to grow for one to two days in liquid TAP medium under constant air bubbling by means of the same day/night cycle, see fig. 2.1.(b). In this work, the wild type strain SAG 11-32c mt- of *C. reinhardtii* was used.

Since no antibiotics are used during cultivation, extensive care has to be taken to ensure cell viability—from working under a laminar flow hood to sterilising the equipment by means of autoclavation and alcohol. In order to check on a macroscopic scale if the culture is in good shape, the liquid culture is poured into a Petri dish to form an approximately 5 mm thick layer and left untouched for several minutes. In a healthy culture, usually after less than five minutes, pattern formation due to bioconvection occurs [58, 98, 130]. Bioconvection itself is a dynamic process induced by algae swimming against gravity and to regions of optimal illumination. As a result, the generated flows form complicated pattern. These pattern are supposed to optimise both gas and nutrient mixing, and permit light to enter deeper layers of the culture. To some degree, a healthy culture tries to keep itself healthy. Exemplary pattern of bioconvection are shown in fig. 2.2.(a–c).

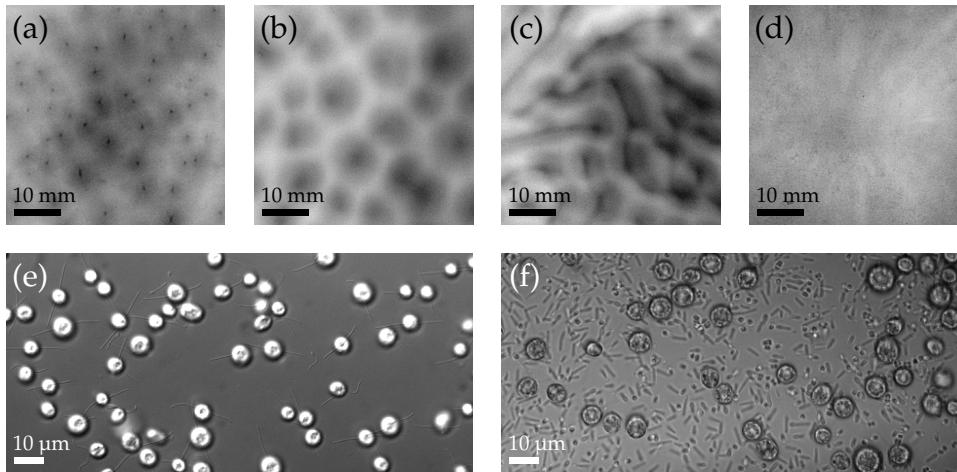


Fig. 2.2: Different cultures of the identical strain of *C. reinhardtii* show pronounced localisation of cells due to bioconvection if culture conditions are good (a–c). Here, dark regions correspond to high microswimmers concentration while the concentration is low in light regions. The pattern shown in (b) usually transitions to a more connected pattern as shown in (c) over time. For comparison, a culture in bad condition shows no bioconvection induced pattern formation at all (d). (e) shows a culture with no contamination at all (DIC image), (f) a culture with strong bacterial contamination (brightfield image).

On the contrary, a culture in bad condition shows no significant pattern formation, see fig. 2.2.(d). Good cultures are inspected microscopically in order to check for any bacterial contamination, see fig. 2.2.(d–e). Only cultures which show both bioconvection and have no visible contaminations are cleared for experiments. Cells are extracted from regions of highest cell concentration because here, they are expected to be the most motile.

All measurements were performed during the 9th and 14th hour of daytime. In order to avoid phototactic response, red light brightfield illumination at an intensity of $\approx 8 \text{ nW}/\mu\text{m}^2$ was used. Prior to experiments, *C. reinhardtii* were allowed to acclimatise for at least 20 min to ensure characteristic behaviour [73].

2.2 Micropipettes apparatus for flagellar dynamics experiments

Device control toolbox for measurement automation. In order to reliably perform the desired measurements, the entire setup got fully automated by the author. Using MATLAB[®]'s object-oriented programming support, I developed classes for every type of device in the setup which enable each of them to be represented as an individual object, exposing the device's specific capabilities in terms of methods which are associated to the object, and thus the device, itself. This means that in order to control a certain device, the object representing the respective device has to

be created first. Each generated object holds the features that the device is capable of, e.g. you can set the pressure by calling the *set pressure* method of the object that represents the pressure controller, but you have to call the *set brightness* method of the object representing the illumination unit to control the brightness.

Consolidated control of every device is a big improvement in contrast to using different software from different manufacturers that either lack flexibility or cannot communicate with each other at all. The software developed in this work closes this gap by enabling interactive control of the devices by means of MATLAB®'s command prompt. This enables rapid and easy prototyping and development of measurement protocols as well as real-time adaptation to changes of experimental conditions. Additionally, the developed protocols can be saved as scripts permitting full automation of the measurement procedure. Note that only device drivers for the operating system but almost no additional, device specific software is required, except the software to set the parameter of the high-speed camera due to protocol issues. Yet, the software toolbox can be used to trigger recordings.

Microscope and illumination. Mounted on a damping table (Accurion Halcyonics Vario) to suppress environmental vibrations and disturbances, an inverted microscope (Nikon TE2000-S) equipped with oil-immersion objectives (Nikon Plan Apo VC 60×) served as a basis for the micropipettes setup, see fig. 2.3. For illumination purpose, two brightfield illumination units and one epifluorescence unit are available: The epifluorescence module consists of a mercury lamp and appropriate filter cubes suitable for the fluorescent tracer particles used to visualise the flow profile in the microfluidics for calibration purpose. One brightfield illumination unit is a white light halogen lamp (Schott KL 2500 LCD) solely used in between actual measurements to determine the position of the cell's eyespot. The second brightfield illumination unit (Zett Optics ZLED CLS 9000 MV-R) is a high-power red *light-emitting diode* (LED) which is used for the actual cell measurements. It can be controlled using a serial interface and, since no appropriate MATLAB® code was available, illumination control was entirely implemented from scratch by the author. Now, setting and reading out the strength of the illumination (in percent) as well as toggling the illumination on or off are possible.

Micropipettes. Individual *C. reinhardtii* cells were fixed by means of glass micropipettes with a tip diameter of 2 µm and a cone angle of the taper of 10° (WPI TIP2TW1). By applying a small under-pressure, the cells are trapped at the pipettes' tip, see fig. 2.4. Gentle suction is very important in order to avoid cell damage due to mechanical stress on the cell body. The most reliable method to achieve this goal is using a manually operated syringe that is attached to the micropipettes. On the one hand, using micropipettes with a sharp taper significantly reduces

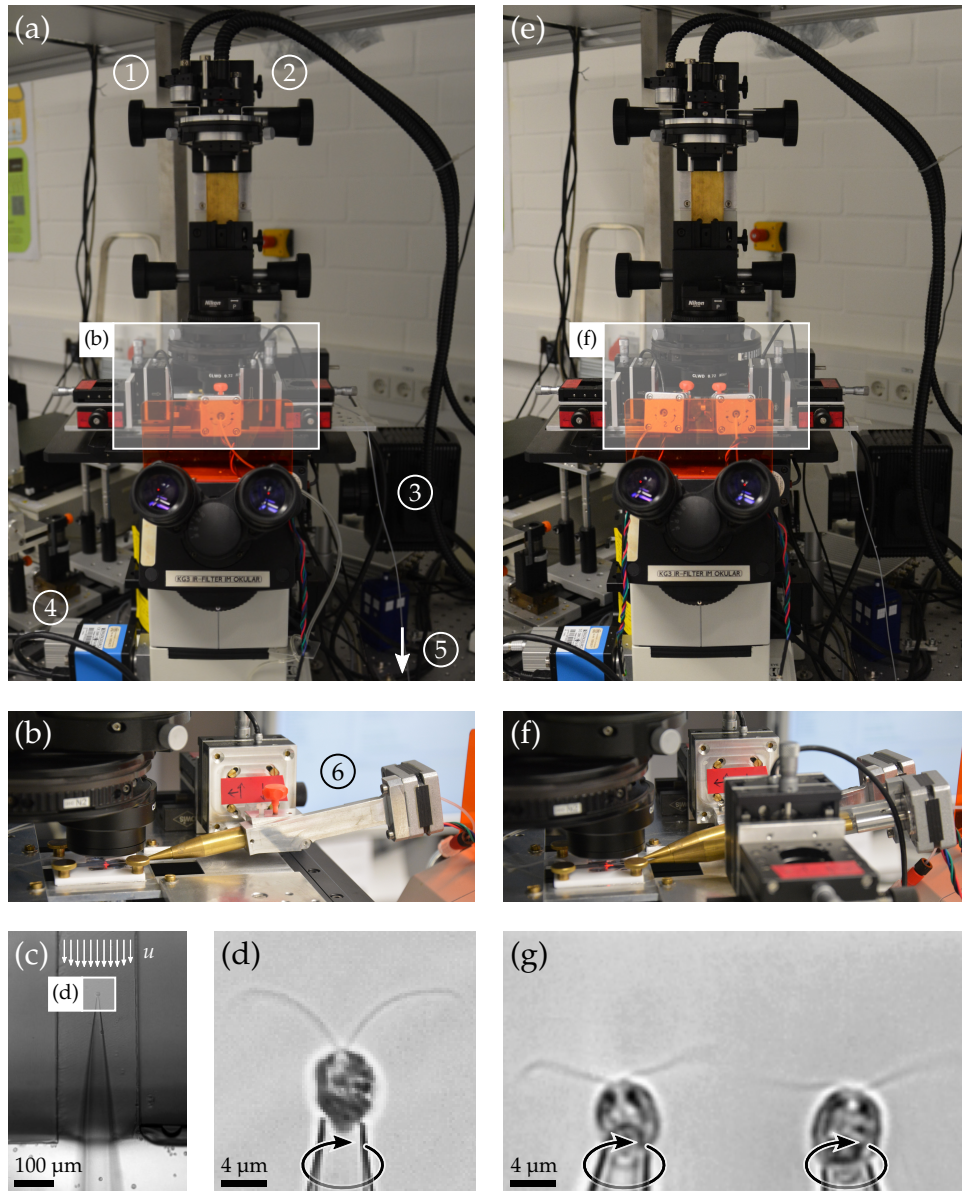


Fig. 2.3: (a–d) illustrate the single micropipettes setup while (e–g) illustrate the twin micropipettes side-by-side configuration: A white light halogen lamp (1) is solely used to determine the *C. reinhardtii*'s eyespot while the high power red LED (2) is used for cell experiments and the mercury arc lamp (3) is used for *micro particle image velocimetry* experiments. All measurements are recorded by means of a high-speed camera (4). To permit both positive and negative flow generation, the fluid reservoir (5) is placed on the floor of the lab. A custom-made micropipettes holder (6) permits high-precision positioning and rotational orientation. (a) and (e) show the entire micropipettes setup while (b) and (f) display a zoom on the micropipettes holder. A micropipette inserted into the sample channel is shown in (c). The micrographs (d) and (g) represent *C. reinhardtii* held in place by means of micropipettes.

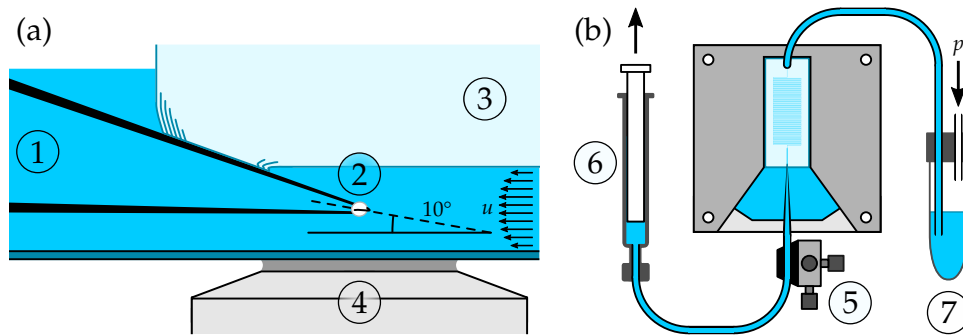


Fig. 2.4: (a–b) A closer look at the micropipettes setup: At the tip of glass micropipettes (1), single *Chlamydomonas reinhardtii* cells (2) are placed in centre of a microfluidics chip (3) and observed using an oil-immersion objective (4). Micropipettes are mounted at an angle of 10° , matching the micropipettes cone angle, using a custom-made holder (5) which permits three dimensional positioning as well as motorised rotational orientation. A manually operated syringe (6) is connected to the micropipettes permitting gently fixation of single *C. reinhardtii* cells. Using a pressure controller, an over-pressure p is applied to the connected fluid reservoir (7), resulting in a flow velocity u in the microfluidic chip.

the probability that flagella stick to the micropipettes [121]. On the other hand, micropipettes with a small cone angle usually have thin side walls and are thus prone to break. Additionally, the taper's cone angle also defines the angle with respect to the sample chamber's ground floor at which the micropipettes have to be mounted in order to certainly place them deep inside the narrow microfluidics channel, see fig. 2.4.(a). Furthermore, micropipettes are gently pressed against the microfluidics chip, hence increasing mechanical stability.

Custom made three axis translational stages carrying the custom designed micropipettes holder, both developed by the author, are used to position the cell in three dimensions, see fig. 2.4.(b). Additionally, one axis can be controlled using a linear piezo stage to either bring the trapped cell into perfect focus (P-622.iCD) or change the inter-pipette distance (P-622.ZCD) with high precision. To reorient the trapped cell so that both flagella are detectable throughout the measurement, micropipettes can be rotated by means of a stepper motor and a rotary encoder. Both stepper motor and rotary encoder are operated by means of a microcontroller (Arduino[®] Mega 2560). Therefore, the existing MATLAB[®] code was modified by the author to link the stepper motor to the encoder permitting computer-aided orientational control by directly setting a certain angle using MATLAB[®]'s command prompt or manually by means of the rotary encoder.

Image acquisition. In order to resolve the motion of *Chlamydomonas*'s flagella, high-speed recordings at 1 kHz are performed using a high-speed camera (Fastec HiSpec 1). Image sequences are saved to the camera's internal memory of 2 GB.

Since data is not stream directly to the PC, the recording performance of the camera is independent of the PC's system performance. Albeit storing to the fast internal memory permits high-speed image acquisition, the amount of data that can be captured at once is limited by the memory size. Thus, it is reasonable to crop the image by choosing a *region of interest* (ROI) to be able to save more images. Additionally, data has to be transferred to the PC before new data can be recorded. The camera allows three different recording modes:

- ▷ *ring mode*: The internal memory is equally divided into 2, 4, 8, or 16 sequences. The size of the ROI defines the recordable number of frames per sequence.
- ▷ *burst mode*: The internal memory is divided into sequences of 1022 images in length. The size of the ROI defines the number of sequences.
- ▷ *single mode*: Images are recorded in a single sequence until the internal memory is full. The size of the ROI defines the recordable number of frames.

Although both the high-speed camera and MATLAB[®] theoretically support GigE Vision, it was not possible to establish a communication. Thus, the camera cannot be controlled using MATLAB[®] directly, but the recording can be externally triggered by means of *transistor–transistor logic* (TTL). Therefore, camera parameter like exposure time, recording mode, framerate, etc., are set using the official software provided by the manufacturer while the recording itself is triggered by a TTL pulse that was generated by means of the Arduino[®] microcontroller and the author's device control, too.

The physical size of a camera pixel is 14 μm leading to a spatial resolution of 233,3 nm in the case of the 60 \times objective used here. Cropping the image to 144 px \times 100 px is on the one hand large enough to capture the cell including their flagella and on the other hand small compared to the resolution of the camera's chip (1280 px \times 1024 px) permitting a recording time of 10 s per sequence (if using the *ring mode* with 16 sequences) or 146 sequences of one second each (if using the *burst mode*).

Pressure controller calibration. A pressure controller (Elvesys[®] Elveflow OB1-MkII) is used to control the flow velocity in the microchannel. Access to basic functions of the pressure controller like setting the desired pressure or retrieving the current pressure is provided by the manufacturer in terms of a *dynamic link library* (dll). MATLAB[®] can load dlls to make their functions available. Yet, calibration of the pressure controller was not provided and thus, was implemented.

In order to reliably apply a certain pressure, calibration of the pressure controller is mandatory and realised as follows: Pressure levels between 0 bar and 2 bar are set and checked for their compliance by means of the internal pressure sensor of

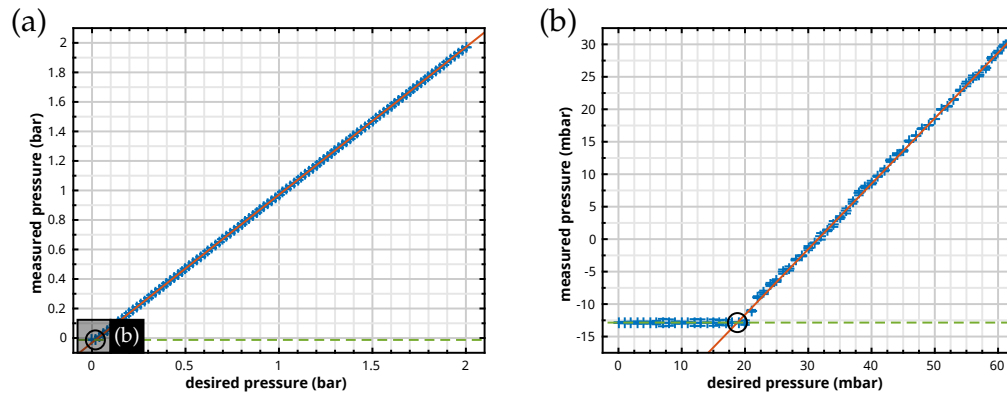


Fig. 2.5: Calibration curve used to reliably set the desired pressure (a) as well as a zoom on the region of low pressure (b). The baseline (green dashed line) is related to the current atmospheric pressure and, thus, has to be determined prior to experiments to guarantee highest precision. Fitting a 3rd-order polynomial to the pressure readings (orange solid line) is used to calibrate the pressure device. The black circle marks the reference point (-12.9 mbar, 19 mbar).

the pressure controller. Fig. 2.5.(a) shows the calibration curve obtained with this method. For a certain range in the low pressure regime up to ≈ 20 mbar, setting a certain pressure returns a constant value which is considered as the baseline (see fig. 2.5.(b), green dashed line). Varying the desired pressure in this range is useless due to undifferentiated readings of the pressure sensor. Therefore, only the range from 20 mbar up to 2 bar is used to model the relationship between the set pressure and its readout value. Due to the slight curvature, a 3rd-order polynomial is used (see fig. 2.5.(b), orange solid line) to obtain the calibration curve. The crossing of the baseline and this calibration curve serves as the reference point for zero pressure. In the exemplary calibration curve shown in fig. 2.5, the reference point is (-12.9 mbar, 19 mbar) which is mapped onto (0 mbar, 0 mbar) by a simply shift. Regular validation of the calibration curve shows only negligible deviations and is thus considered a device-specific property. However, the baseline slightly varies with the current atmospheric pressure and hence has to be determined at least once per measurement day to gain highest precision.

The fluid reservoir is positioned on the floor of the laboratory leading to a height difference of approximately 130 cm between the reservoir and the sample chamber. Due to the hydrostatic pressure difference according to Pascal's law, this leads to a backward flow from the sample channel to the fluid reservoir if no pressure is applied. In order to compensate for this height difference and, consequently, to achieve zero flow in the sample channel, an offset pressure of 130 mbar has to be applied. However, this configuration has the advantage of enabling the generation of backward flow although the pressure controller is only capable of generating over-pressure.

2.3 Design, fabrication, and calibration of the microfluidics chip

Drawing of the microfluidic chips as well as initial microfluidics fabrication was performed in close cooperation with Emmanuel Terriac.

Microfluidics used to generate a homogeneous flow in the channel's central region, i.e., in a region of at least twice the span width of *Chlamydomonas reinhardtii*, are designed and fabricated by means of photo-lithography and *polydimethylsiloxane* (PDMS) replication. Since the flow generation itself is pressure-driven, the flow velocity depends on the microfluidics dimensions which are not known precisely enough to reliably translate applied pressures to flow velocities directly. Thus, fabricated microfluidics are calibrated using *micro particle image velocimetry* (μ PIV).

Navier-Stokes equations for homogeneous, incompressible fluids. Physical phenomena like fluid flow in a tube, air flow around aircrafts, or even the weather can be described by means of the Navier-Stokes equations which can be formulated as a balance of rescaled forces

$$f_{\text{inertia}} = f_{\text{external}} + f_{\text{stress}} \quad (2.1)$$

with $f = F/V$. The stress term f_{stress} is the sum of a contribution $\mu\Delta\mathbf{u}$ due to diffusion and internal forces $-\nabla p$, with μ being the viscosity of the fluid, \mathbf{u} being the vector of fluid velocity, and p being the pressure. Furthermore, inertia $f_{\text{inertia}} = \rho\dot{\mathbf{u}}$ is the sum of the convection term $\rho(\mathbf{u} \cdot \nabla) \cdot \mathbf{u}$ and the variation $\rho\dot{\mathbf{u}}$, with ρ being the fluid density. At last, external forces $f_{\text{external}} = \rho\mathbf{g}$ with \mathbf{g} being body acceleration in general, e.g., gravity, may influence the motion as well. Taking all contributions into account, the Navier-Stokes equations for homogeneous, incompressible fluids read

$$\underbrace{\rho\partial_t\mathbf{u}}_{\text{variation}} + \overbrace{\rho(\mathbf{u} \cdot \nabla) \cdot \mathbf{u}}^{\text{convection}} = \underbrace{f_{\text{external}}}_{\text{external source}} - \overbrace{\nabla p}^{\text{internal source}} + \underbrace{\mu\Delta\mathbf{u}}_{\text{diffusion}} \quad \text{and} \quad \nabla\mathbf{u} = 0. \quad (2.2)$$

If inertial effects dominate over viscous forces, turbulences may occur, but if viscous forces dominate over inertia, the flow is laminar. In order to classify the flow, the Reynolds number $\mathcal{R}e$, a dimensionless quantity defined as the quotient of inertial forces and viscous forces, is used:

$$\mathcal{R}e = \frac{\rho l u}{\mu}. \quad (2.3)$$

The Reynolds number depends both on the fluid specific parameter density ρ and viscosity μ as well as the flow velocity u and the characteristic length scale l . In the

case of water ($\rho = 1000 \text{ kg m}^{-3}$, $\mu = 1 \text{ mPa s}$) flowing at a velocity of $u = 10 \text{ mm/s}$ through a pipe with a diameter of $l = 200 \text{ }\mu\text{m}$ results in a Reynolds number of $Re = 2$. In general, the flow is considered turbulent if $Re > 4000$ and laminar if $Re < 2000$ [51].

Pressure driven flow in a rectangular duct. In the low Reynolds number regime, inertial effects are negligible leading to $\dot{\mathbf{u}} = \mathbf{0}$ and the Navier-Stokes equations for a homogeneous, incompressible Newtonian fluid simplify to the Stokes equations

$$\mathbf{0} = \mathbf{f}_{\text{external}} - \nabla p + \mu \Delta \mathbf{u} \quad \text{and} \quad \nabla \cdot \mathbf{u} = 0. \quad (2.4)$$

Assuming that the fluid flows due to a pressure drop Δp in x -direction through a rectangular channel of length l , width w ($-w/2 \leq y \leq w/2$), and height h ($0 \leq z \leq h$) with $h \leq w$ as sketched in fig. 2.6.(a). Calculations in the case of $h > w$ are realised by rotating the coordinate system in such a way that $h \leq w$ is fulfilled again. The solution to the Stokes equations is a flow profile given by [134, 135, 139]

$$u_x(y, z) = \Delta p \frac{4h^2}{\pi^3 \mu l} \sum_{n, \text{ odd}} \frac{1}{n^3} \left[1 - \frac{\cosh\left(\frac{n\pi y}{h}\right)}{\cosh\left(\frac{n\pi w}{2h}\right)} \right] \cdot \sin\left(\frac{n\pi z}{h}\right). \quad (2.5)$$

Flow profiles for different aspect ratios ϵ —the aspect ratio is the quotient of the width w of a channel and its height h —are visualised in fig. 2.6.(b). If the channel

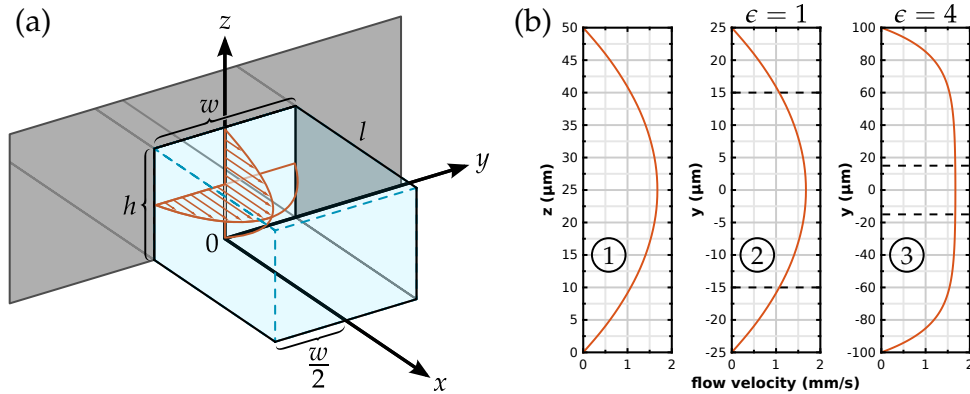


Fig. 2.6: Sketch of a microfluidic channel (a) as well as calculated flow profiles (b) at horizontal centerline $y = 0$ (1) and at vertical centerline $z = h/2$ for an aspect ration of $\epsilon = w/h = 1$ (2) and $\epsilon = 4$ (3), respectively. For an aspect ratio of $\epsilon = 1$, the flow profiles of both horizontal and vertical centerlines are identical. Dashed black lines indicate the maximum span width of *C. reinhardtii*. In this central region, the flow profile in y -direction flattens significantly with increasing ϵ and the imposed flow can be considered homogeneous.

is as high as wide, the flow profiles in both y- and z-direction are identical, see fig. 2.6.(b, 1–2). With increasing ϵ , the central region of the flow profile in y-direction flattens significantly, see fig. 2.6.(b, 3).

The volumetric flow rate Q in a microfluidic channel can be calculated by integrating eq. 2.5 over the channel's cross section:

$$Q = 2 \int_0^{\frac{w}{2}} \int_0^h u_x(y, z) dy dx = \Delta p \cdot \frac{wh^3}{12\mu l} \left[1 - \sum_{n, \text{ odd}} \frac{192}{(n\pi)^5} \frac{h}{w} \tanh\left(\frac{n\pi w}{2h}\right) \right]$$

$$\Leftrightarrow Q = \Delta p \cdot \frac{1}{R}. \quad (2.6)$$

The microfluidic hydraulic resistance R solely depends on the channel's geometrical measures and the fluid viscosity μ . Eq. 2.6 is known as Hagen-Poiseuille's law.

Microfluidics chip design. Volumetric flow rates in microfluidic circuits can be calculated using rules similar to Kirchhoff's circuit laws used in electrostatics. Kirchhoff's circuit laws state that in an electric circuit, the sum of all voltages in a mesh is equal to zero. Furthermore, the sum of all incoming currents at a nodal point is equal to the sum of all outgoing currents. Both conservation laws can be applied to microfluidic circuits by using the similarity between voltage and pressure difference Δp as well as between electric current and volumetric flow rate Q in every channel j . Therefore, Kirchhoff's circuit laws can be rewritten as

$$\underbrace{\sum_j Q_j = 0}_{\text{nodal rule}} \quad \text{and} \quad \underbrace{\sum_j \Delta p_j = 0}_{\text{mesh rule}} \quad (2.7)$$

and the total hydraulic resistance for a parallel connection of microfluidic channels and a serial connection of microfluidic channels read

$$\underbrace{\frac{1}{R} = \sum_j \frac{1}{R_j}}_{\text{parallel connection}} \quad \text{and} \quad \underbrace{R = \sum_j R_j}_{\text{serial connection}} \quad (2.8)$$

respectively. Several constraints for the chip design had to be take into account:

- ▷ Using the full range of the pressure controller of up to 2 bar, the microfluidic channel has to decrease the applied pressure and thus restrict the available volumetric flow rates to the desired range in order to be able reliably set flow velocities up to 12 mm/s.
- ▷ In order to simplify the photolithography procedure, a single layer chip design was chosen so all channels have the same height.

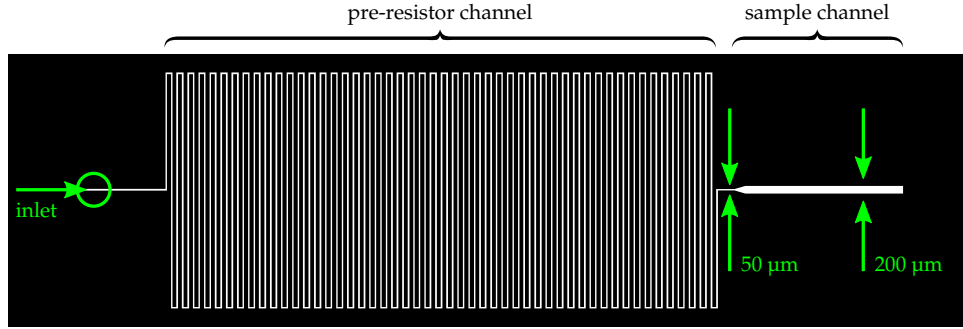


Fig. 2.7: Microfluidics chip design realised as a photo-lithography mask. Black areas protect the underlying photo-resist from exposure to UV light while white areas allow UV light to shine through. The pre-resistor channel on the left is used to significantly reduce the pressure in the sample channel on the right. Indicated channel dimensions (green arrows and text) and the position of the connection hole (green circle) are shown for comprehension purpose and not part of the actual lithography mask.

- ▷ The channel has to be high enough so that the micropipettes fit inside but still low enough so that the pipette is in close contact with the microfluidics chip which improves mechanical stability.
- ▷ Within the uncertainty of micropipettes positioning, variations in flow velocity due to the Poiseuille flow profile perpendicular to the imaging plane should be less than 5%.
- ▷ On the one hand, the aspect ratio ϵ has to be high to guarantee a flat flow profile in the central region of the imaging plane of the channel where the measurements take place. Since the span width of *C. reinhardtii* is approximately 20 μm , a homogenous flow over 30 μm in the centre is more than sufficient.
- ▷ On the other hand, ϵ should not exceed 10 to reliably minimise the potential collapse of the channel during plasma bonding.

In order to satisfy these requirements, the microfluidics chip was realised as a serial connection of two channels as shown in fig. 2.7: The snake-like channel on the left acts as a very high pre-resistor which is used to reduce the applied pressure to the range that is necessary to achieve the desired flow velocity in the actual sample channel on the right. Using the relations given in eq. 2.7, the volumetric flow rate is constant. Therefore, eq. 2.6 can be rewritten to

$$Q = \Delta p / \sum_j R_j \quad (2.9)$$

with $j \in \{\text{pre-resistor channel, sample channel}\}$. Note that Δp is the global pressure difference applied by means of the pressure controller and not the individual pressure drop in each channel, respectively. If the geometrical measures of the

channels are well known, the volumetric flow rate and thus the mean flow velocity in channel j is given by

$$\bar{u}_j = \frac{Q}{w_j h_j}. \quad (2.10)$$

Since the measurements take place in the centre of the microchannel, the important parameter is not the mean velocity but rather the peak velocity. In order to find a relation between both velocities, a closed yet approximated solution for the laminar flow in a rectangular channel is given by [102]

$$u_{x,j}(y, z) = \bar{u}_j \left(1 - \left[\frac{2y}{w_j}\right]^s\right) \left(1 - \left[\frac{2z}{h_j}\right]^r\right) \quad (2.11)$$

with generalised exponents s and r according to [86]

$$s \approx 1.7 + \frac{\epsilon_j^{1.4}}{2} \quad \text{and} \quad r \approx \begin{cases} 2 & , \text{ if } \epsilon_j \geq 3 \\ 2 + 0.3 \left[\epsilon_j^{-1} - \frac{1}{3}\right] & , \text{ if } \epsilon_j < 3 \end{cases} \quad (2.12)$$

and aspect ration $\epsilon_j = w_j/h_j$ of channel j . Integrated eq. 2.11 over the cross-section of the corresponding channel j leads to

$$u_j^{max} = \bar{u}_j \left(\frac{s+1}{s}\right) \left(\frac{r+1}{r}\right). \quad (2.13)$$

Calculations show that if fixing the channel's height to $50 \mu\text{m}$, the requested flow velocity in the sample channel can be achieved by using a pre-resistor channel of $50 \mu\text{m}$ in width and approximately 700 mm in length. A sample channel of $200 \mu\text{m}$ in width results in $\epsilon = 4$ leading to a reasonably flat flow profile in the central region. Additionally, the flow velocity perpendicular to the imaging plane deviates less than 5% from the peak velocity within a range of $\approx 5 \mu\text{m}$ from the centre. The chosen height is large enough so that micropipettes fit inside but can still be brought into slight contact with the microfluidic chip. The parameter aimed at during microfluidics fabrication are summarised and compared to the parameter of actually fabricated microfluidics in tab. 2.1.

The pre-resistor channel is the most prominent contributor to the overall pressure drop. Compared to the resistance of the sample channel, the resistance of the pre-resistor channel is 1000 times higher. Additionally, the connection tube has—albeit its length of $\approx 1,200 \text{ mm}$ —a resistance of only $\approx 3 \cdot 10^{-5} \text{ mPa s}/\mu\text{l}$. Therefore, both the sample channel and the connection tube can be neglected in terms of pressure drop calculations.

Tab. 2.1: Comparison of microfluidics target parameter (design) with the actually realised microfluidic chips A, B, and C. The lengths of the sample channel and the pre-resistor channel solely depend on how precise the chip was cut open and the connection hole was drilled, respectively. Thus, the designed lengths with deviations estimated in a worst-case sense as well as average values ($n_A = 13$, $n_B = 8$, and $n_C = 8$ channels, each measured at more than ten different positions) for both width and height are used to calculate the hydraulic resistances.

type	length (mm)	width (μm)	height (μm)	resistance ($\text{mPa s}/\mu\text{l}$)
<i>pre-resistor channel</i>				
design	704.65	50.00	50.00	—
chip A	— (<4%)	$48 \pm 2\%$	$52 \pm 4\%$	$3 \pm 9\%$
chip B	— (<4%)	$56 \pm 4\%$	$50 \pm 1\%$	$3 \pm 6\%$
chip C	— (<4%)	$58 \pm 2\%$	$52 \pm 4\%$	$2 \pm 12\%$
<i>sample channel</i>				
design	3.50	200.00	50.00	—
chip A	— (<4%)	$206 \pm 1\%$	$52 \pm 4\%$	$0.002 \pm 12\%$
chip B	— (<4%)	$215 \pm 1\%$	$50 \pm 1\%$	$0.002 \pm 4\%$
chip C	— (<4%)	$215 \pm 1\%$	$52 \pm 4\%$	$0.002 \pm 12\%$

Microfluidics fabrication. A multitude of different steps are necessary to fabricate microfluidic devices. The goal in the end is to fabricate a negative master mould from which identical microfluidics can be replicated by means of a mechanically soft elastomeric material, e.g., the transparent, biocompatible polymer *polydimethylsiloxane* (PDMS).

First of all, a photolithography mask with the desired channel geometry has to be drawn and produced, see fig. 2.7. In this case, the mask got printed on a transparent film (by Micro Lithography Services Ltd.) with a precision of $5 \mu\text{m}$. Its quality is a crucial point regarding accuracy of the final microfluidics device. This binary mask acts as a template allowing light to shine through a certain pattern while blocking light in the remaining areas. An *ultraviolet* (UV) lamp is used to project the mask's image onto a silicon wafer. The mask is in physical contact with the wafer and kept in place using a quartz glass plate fixing everything using vacuum suction.

A photoresist—a light sensitive material—is spin-coated on the silicon wafer with the desired thickness, see fig. 2.8.(a). There are two different types of photoresist: positive or negative. Here, the negative photoresist SU-8 is used. Negative means that the photoresist hardens under UV exposure but remains soft if not exposed, see

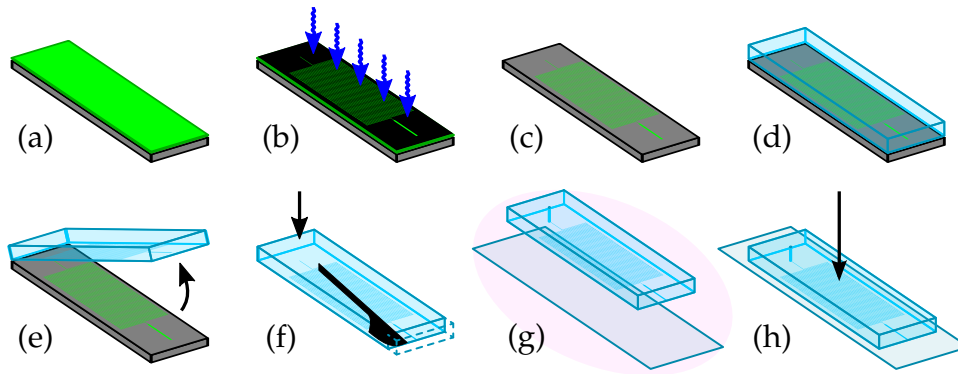


Fig. 2.8: A silicon wafer spincoated with SU-8 photoresist (a) was structured using photolithography (b) to produce a master mould (c). PDMS is used to replicate this mould (d–e), and after drilling the connection hole and cutting the chip open (f), the PDMS chip is bonded to a cover slide by means of plasma activation (g–h).

fig. 2.8.(b). In the subsequent development process, see fig. 2.8.(c), the unexposed parts are removed using *propylene glycol methyl ether acetate* (PGMEA) or acetone. Since only the substrate layer is structured and there is no further etching process involved to structure the silicon wafer, the photoresist that remains on the silicon wafer directly forms the microfluidics mould. A subsequent post-bake-process is performed to guarantee high mechanical resistance. This developed SU-8 pattern acts as the negative mould for microfluidics fabrication. Degassed PDMS is casted on the negative mould, see fig. 2.8.(d), and cured for two days in the oven at 80°C . After this curing step, the PDMS is peeled off the mould releasing the real microfluidics, see fig. 2.8.(e). After the connection hole was drilled and chips were cut open, see fig. 2.8.(f), the PDMS chip and a no.1 cover slide are plasma-activated, see fig. 2.8.(g), and gently pressed together to form strong covalent bonding, see fig. 2.8.(h). To obtain maximum pressure resistance, the final chips are put back into the oven for at least one day at 80°C .

Several moulds were produced showing slight but expected geometrical differences due to the manufacturing process. While the height of all chips is mainly constant due to the homogeneous distribution of the photoresist during the spincoating process, the lateral channel dimensions vary. The main reasons for this kind of imprecision are tiny errors in the photolithography process, e.g., if the contact between the mask and the photoresist is not perfect, if the one-sided printed mask has been placed upside down, due to light diffraction, or overexposure. This error leads to a larger gap between the actual mask and the photoresist and thus to channels being larger than designed.

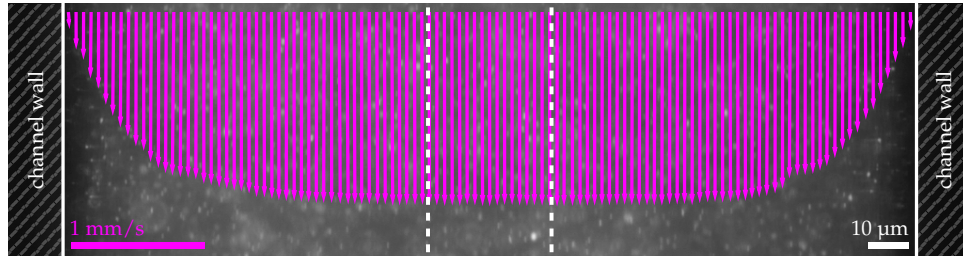


Fig. 2.9: Visualisation of an exemplary μ PIV measurement. Purple arrows are streamline- and time-averaged flow vectors for a fixed pressure drop. Solid white lines indicate channel borders while dashed white lines correspond to the span width of a *C. reinhardtii* cell positioned in the centre of the channel. Here, the flow profile can be considered homogeneous within experimental noise.

Microfluidics calibration. Since all microfluidics' parameter including errors are well known, we can calculate the flow velocity using eq. 2.13. However, in the theoretical description, simplifications were assumed, e.g., the channels are modelled as being straight with constant physical dimensions and no-slip boundary conditions albeit in reality, the pre-resistor channel is snake-like and only the glass surface is indeed slip-free but not the PDMS surface. Therefore, calibration is mandatory to determine the correct relation between applied pressure and obtained flow velocity.

The flow inside the microfluidics channel is visualised by means of tracer particles whose motion are recorded and analysed to deduce the flow field, see fig. 2.9. This technique is known as *particle image velocimetry* (PIV). The signal-to-noise ratio is increased by using fluorescent particles. These particles can be excited using a certain wavelength to emit light at a higher wavelength. Usually, laser sheet illumination is used to excite and thus visualise only particles in a two-dimensional plane. Yet, this kind of illumination is both not applicable nor necessary if using epifluorescence microscopy. Here, we make use of the fact that back-illuminated, high numerical aperture objectives only focus light to the two-dimensional focal plane. Since excitation and emission can be reliably separated by means of appropriate filter sets, only the emitted light of the tracer particles in the focal plane contributes to the recorded images. This modification of PIV is also called *micro particle image velocimetry* (μ PIV) [76].

μ PIV is used to determine the flow profile as a function of the applied pressure. Time series of fluorescent tracer particles with a diameter of $0.5 \mu\text{m}$ (Sigma Aldrich L3280) at a concentration of 1200 ppm are recorded in the sample channel at a frame rate of 1 kHz. These particles are small enough to perfectly follow the flow, large enough to be easily visible, and the volume fraction is low enough so that the particles themselves do not influence the flow. In general, the size of the interrogation window has to be adapted depending on the concentration of the

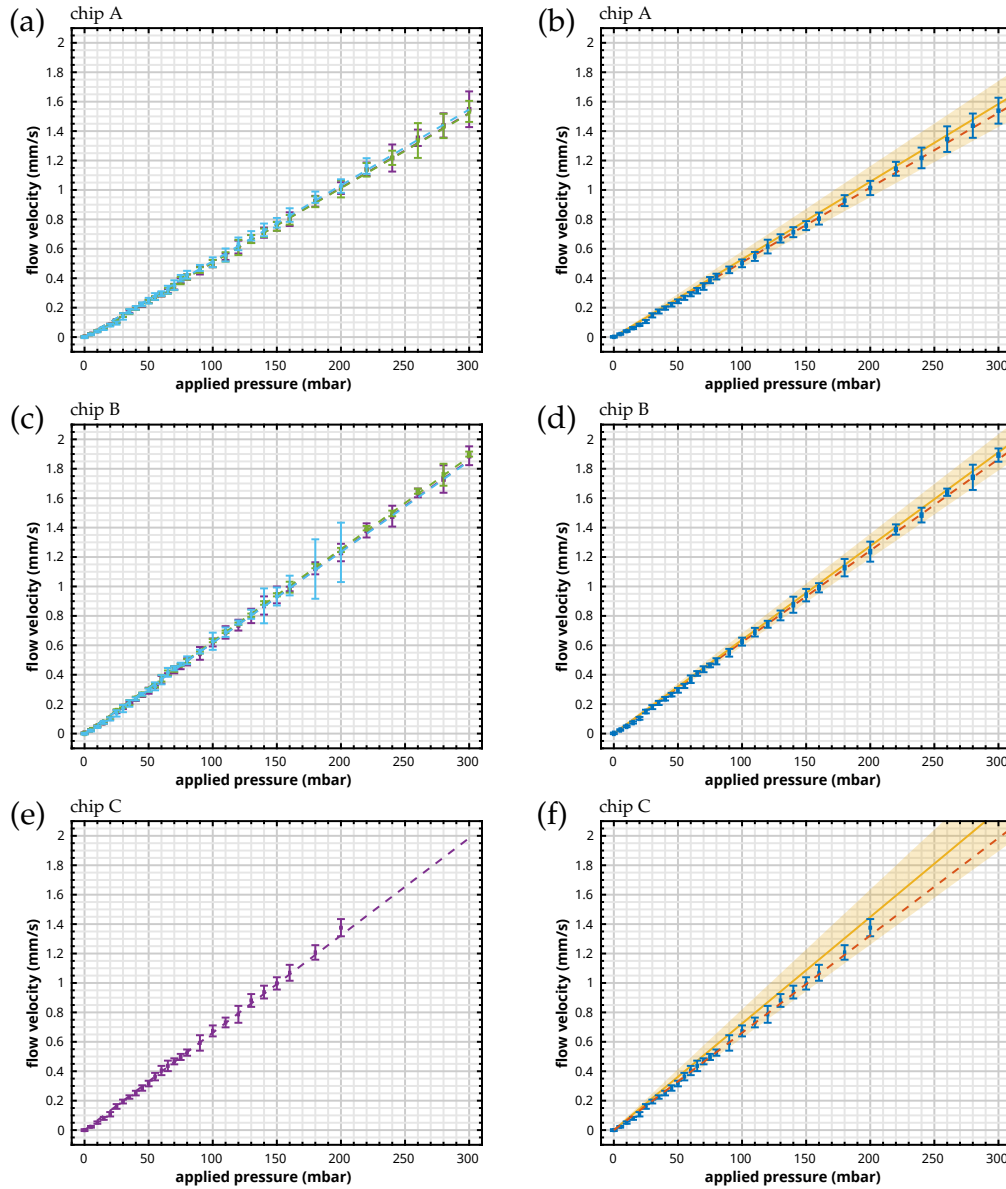


Fig. 2.10: Relation between applied pressure and resulting flow velocity for three microfluidic chips. Results for chip A and B (a, c) are based on three different batches (purple, green, blue), calibrated by means of at least three individual μ PIV measurements (not labelled individually), respectively. Results for chip C (e) are based on six individual measurements (purple, not labelled individually) of only one batch. Linear regressions (dashed lines) to velocity data for individual batches are almost identical. Averaging over all measurements per chip (blue dots, error bars indicate standard deviation), the characteristic calibration curve (orange dashed lines) is obtained for chips A, B, and C, respectively (b, d, e). Yellow shadings visualise the confidence interval (mean \pm s.e.) of theoretical calculations (yellow solid line) based on channel parameter (tab. 2.1) and measured pressure deviations.

tracer particles, the applied flow velocity and the recording frame rate, so that at least the same 15 particles are visible throughout at least two subsequent images [62]. Higher flow velocities would require either larger interrogation windows, resulting in a reduced spatial resolution of the flow profile, or higher frame rates. The latter is often not possible due to the usually very weak fluorescence signal. For a particle concentration of 1200 ppm and interrogation windows of $7\ \mu\text{m} \times 7\ \mu\text{m}$, a frame rate of 1 kHz guarantees reliable detection of flow velocities up to 2–3 mm/s.

The flow profile reconstruction procedure—for which we used the MatPIV [123] implementation—works as follows:

- ▷ Subsequent images form an image pair.
- ▷ Each image is divided into smaller blocks, also called interrogation window, which may overlap, too.
- ▷ Corresponding interrogation windows are cross-correlated pairwise in order to compute the displacement.
- ▷ Since the time between subsequent images as well as the pixel size are known, the result of the cross-correlation is a flow velocity vector in time for each interrogation window, respectively.

The reconstructed, time-averaged flow profile per streamline as shown in fig. 2.9 is similar to the previously calculated flow profile in the centre of a rectangular channel with an aspect ratio of $\epsilon = 4$, see fig. 2.6. Due to the fact that the flow profile is reasonably flat in the central region of the microfluidic channel (dashed lines), flow vectors in this part of the full flow profile are averaged to obtain the maximal flow velocity additionally removing artefacts caused by Brownian motion. Fig. 2.10 shows the calibration result as well as the corresponding theoretical values of actually used chips. Calculations were performed using the optically determined channel geometries averaged over several batches, and the measured viscosity of TAP medium of $\mu = 1\ \text{mPa s} \pm 4\%$. μPIV results were validated using different batches of microfluidics to account for batch related inaccuracies. In comparison to imperfections originating from the initial fabrication process, batch related inaccuracies are small.

In order to quantify how long it takes until the desired flow velocity has evolved, time resolved μPIV measurements of pressure jumps are performed, see fig. 2.11. Here, the pressure is changed almost instantaneously—the response time given by the manufacturer is 9 ms—from 0 mbar to 1800 mbar (corresponding to a flow velocity of about 9 mm/s) or vice versa from 1800 mbar to 0 mbar and the transition from the current pressure to the desired pressure is recorded. This is realised by sending a TTL trigger pulse which has been generated by means of the Arduino®

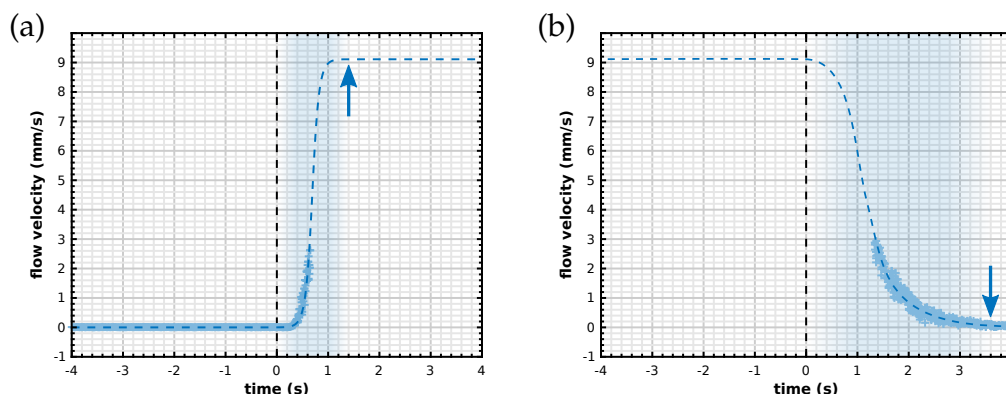


Fig. 2.11: (a) The transition from 0 mbar to 1800 mbar (corresponding to a flow velocity of about 9 mm/s) and (b) vice versa. The dashed black line marks the trigger event when the pressure is changed almost instantaneously. The arrow marks the point in time when the flow reaches its desired velocity, emphasised by the coloured transition. Dashed lines are fits to the flow velocity data. Due to experimental constraints, as discussed in the main text, flow velocities above 3 mm/s could not be visualised.

microcontroller, to the camera, directly followed by setting the desired pressure, either 0 mbar or 1800 mbar. The camera itself is set to record the same amount of frames prior and subsequent to a received trigger event, usually about 10 s, rendering the recorded sequence centred around the trigger event with negligible signal delay. On average, it takes about 1 s to jump from 0 mbar to 1800 mbar and about 4 s to jump from 1800 mbar down to 0 mbar. Consequently, in order to avoid measuring the transition from one flow velocity to the other albeit a measurement under constant flow conditions is desired, waiting times of at least 4 s (in a worst case sense) have to be taken into account.

3

Flagellar beating under load

The eukaryotic flagellum is a very complicated machine on a very small scale. Gaining knowledge on how individual molecular motors which power the flagellar beat is as interesting as it is experimentally difficult. However, by not looking on the individual motor level but on the entire flagellum, we can learn more about how these motors work collectively within the complex structure of a flagellum. The best way to test the performance of a system is to put it under stress.

In a joint project together with Gary S. Klindt and Benjamin M. Friedrich from the Max Planck Institute for the physics of complex systems in Dresden, we investigated the influence of external load on the flagellar beat both experimentally and theoretically. Detailed knowledge on this load response in terms of phase speed and amplitude alteration provides insights into shear flow induced re-orientation of cells, interaction with obstacles and flagellar synchronisation. On the experimental side, we positioned single *Chlamydomonas reinhardtii* cells by means of micropipettes in the centre of a microfluidics chip and exposed the cell, and thus its beating flagella, to different external load conditions. Measurements performed under no flow conditions were used to calibrate the theoretical model that was developed by our collaborators. In this model, flagellar oscillations are representing as a limit cycle oscillator. By comparing the theoretical predictions with experimental results, we were able to estimate the chemo-mechanical efficiency of the flagellar beat. Additionally, the model was able to predict our experimentally observed phenomenon of flagellar stalling. Yet, the model was not able to predict the hysteresis in flagellar stalling which we observed in experiments. Furthermore, in experiments, we discovered two previously unknown dynamic modes of flagellar beating. Finally, we could show that, in general, an external load reduces the synchronisation capabilities of *C. reinhardtii*'s two flagella.

3.1 Phase-dependent load response of the eukaryotic flagellum

Code utilised for full flagellar tracking was developed in close collaboration with Gary S. Klindt from the Max Planck Institute for the physics of complex systems in Dresden in the group of Benjamin M. Friedrich. Our software allows fully automated extraction of C. reinhardtii's cell body and its two flagella with high precision in order to determine the beating frequency, or extract the flagellar shape. Due to the modular design of our

evaluation code, the respective task can be arbitrarily configured and composed to obtain custom evaluation programs. The theoretical model of flagellar oscillations, the evaluation of experimental data using principle component analysis and the limit cycle representation was devised and performed by Gary S. Klindt as well in the context of our joint project [65, 66]. For the sake of completeness, I will only roughly summarise the theory here. As an addition to this summary and for additional information, please consult [64].

3.1.1 Data evaluation

Cell body tracking. Reliably determining the cell body is the crucial first step on the way to fully automated tracking. Albeit the cell is fixed by means of micropipettes and thus cannot swim away any more, cell-cell variance is still present. Furthermore, this step enables accounting for orientational misalignment of the trapped cell. Knowledge of the precise cell body position permits automatic

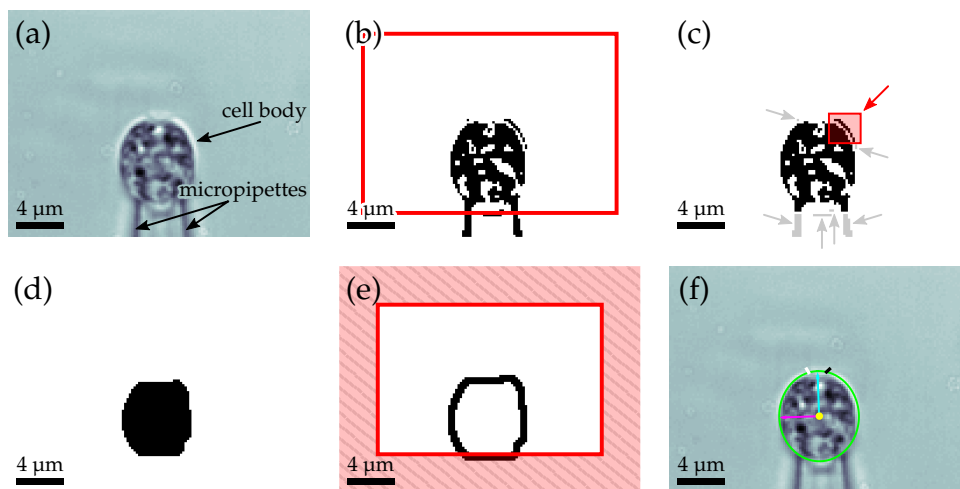


Fig. 3.1: By taking the time-average of each pixel, respectively, an image is calculated in which both the cell body and the micropipettes are still present but no flagella (a). Absolute differences to the overall median pixel value represent the cell body as well as the micropipettes (b). Here, pixels covered by the red frame are set to white introducing cuts to the image. Due to these cuts, the cell body is separated from the micropipettes as good as possible (c). Remains of the micropipettes as well as tiny dirt (marked in grey) or camera noise are removed by means of several morphological opening and closing operations. However, some artefacts might not be removed completely (red box). The filled convex hull of the largest pixel cluster represents the cell body (d). Opening the cell's perimeter at the position of the micropipettes, i.e., setting all pixels outside the red frame to white, removes cell body deformations due to micropipettes fixation (e). (f) shows the result of the fit of an ellipsoid to the cell rim. The position of the centre of mass of the cell (yellow dot), its major axis (light blue arrow) and its minor axis (magenta arrow), the cell rim (green ellipsoid), and the manually set flagellar starting points (black and white lines) are shown.

determination of the flagellar starting points. At last, image preprocessing prior to flagellar tracking depends on reliable masking of the cell body. The steps which are necessary to extract cell body position and orientation are illustrated in fig. 3.1.

First, by taking the time-average of each pixel, respectively, an image is calculated in which only the flagella have been averaged out but both the cell body and the micropipettes are still present (fig. 3.1.(a)). Since most of the image is background data and not the actual cell or the micropipettes, the median of all pixel values represents the value of the image background. Thus, absolute differences to this median pixel value represent either the cell body or the micropipettes. After binarisation (fig. 3.1.(b)), remains of the micropipettes might still disturb the determination of the cell body. Cutting lines (red lines) are introduced to separate the cell body from the micropipettes.

Black pixels which are still connected to the edges of the image most probably represent the micropipettes and have to be removed together with other isolated pixels. Morphological opening and closing operations are used to remove these unwanted pixel clusters (fig. 3.1.(c)). While some artefacts might survive this procedure (red arrow), most of the unwanted pixel clusters (grey arrows) are successfully removed. Taking into account that the cell usually does not have dents, the filled convex hull to the largest pixel cluster, which is supposed to be the cell body, is calculated (fig. 3.1.(d)). Pixels outside the red frame are removed in order to open the calculated cell perimeter (black) and thus remove possible cell deformations due to micropipettes fixation (fig. 3.1.(e)). An ellipsoid (green) as a good approximation to the prolate shape of *C. reinhardtii* is fitted to the cell rim returning its centre (yellow dot) as well as its major axis (light blue arrow), its minor axis (magenta arrow) and thus its orientation (fig. 3.1.(f)). The black and the white line indicate the manually set flagella starting vector of each flagellum, respectively. The orientation of the fitted ellipsoid is corrected in such a way that its major axis is centred with respect to the manually set starting points.

Full flagellar tracking. In order to elucidate the load response of the flagellar beat, information about the full flagellar shape during beating is mandatory. Individual flagella are entirely tracked using an iterative procedure: By taking the time-average of each pixel, respectively, a mean image is calculated from which the current image is subtracted (fig. 3.2.(a)). Since the cell is fixed by means of micropipettes, this procedure removes the cell body as well as the micropipettes, leaving only the flagella and the pulsating vacuole at the basal body location visible.

From a phenomenological point of view, the flagella in the image can be described as regions of similar greyscale level. By calculating the weighted correlation in the environment of each pixel, we can assign two quantities to them: the correlation

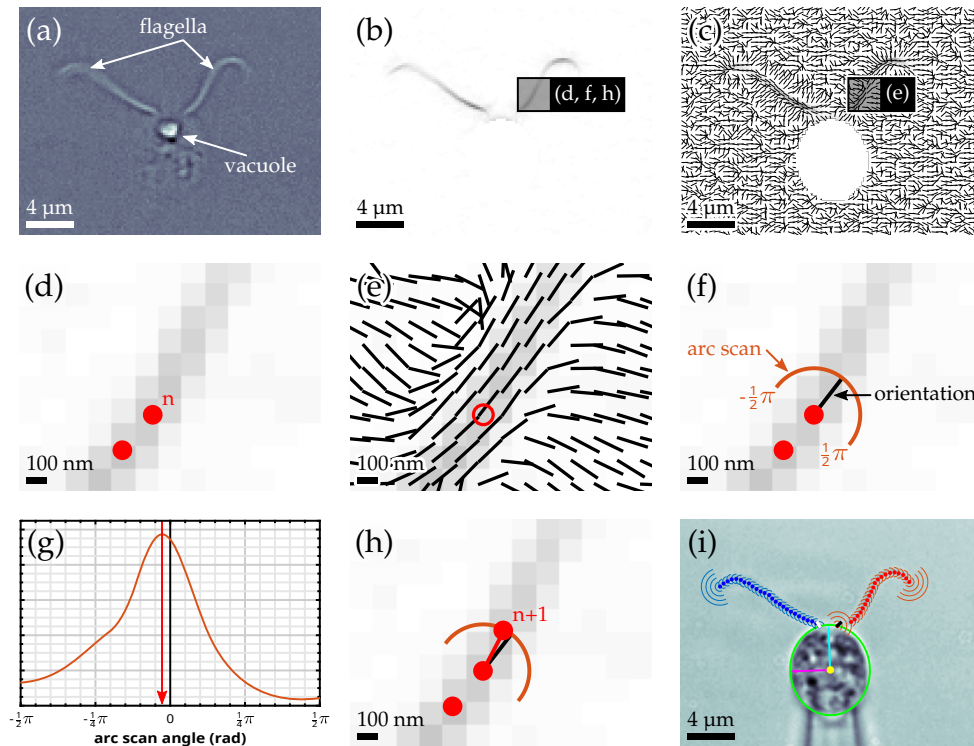


Fig. 3.2: (a) Subtracting the current image from the time-average of each pixel, respectively, both the micropipettes and most of the cell body is successfully removed. (b) Greyscale representation of the magnitude component of the nematic field ranging from zero magnitude (white) to maximal magnitude (black). (c) The orientational component (black lines) is shown as an overlay to the magnitude component for comprehensibility reasons. The iterative arc scan procedure (d–h) works as follows: Starting from an already given flagellar point n (d, red dot) and the corresponding orientation at this point (e, black line), an arc scan is constructed (f, orange half circle). The point of maximal intensity along this arc is determined (g, red arrow) defining the new starting point $n + 1$ for the next iteration (h, red dot). (i) shows the result of both cell body tracking and flagellar tracking.

magnitude (fig. 3.2.(b)) as well as the direction of maximal change in correlation (fig. 3.2.(c)). Since the latter is invariant under rotation about π , we are not dealing with a vector field but rather with a so called nematic field. Consequently, we call this kind of image processing a nematic transform [64]. In both the magnitude component and the orientational component of the nematic field, remains of the cell body are masked using the cell body parameters determined previously, see fig. 3.1. The nematic magnitude can be interpreted as an contrast-enhanced version of the input image while the nematic orientation indicates the direction of connected, underlying structures—here, the flagellum.

Both components of the nematic field are mandatory for the successive, actual flagellar tracking algorithm which is a multi-step, iterative procedure: First, the

orientation at an already given flagellar point (fig. 3.2.(d), red dot marked with n) is read out from the orientational component of the nematic field (fig. 3.2.(e), red circle), defining the centre (fig. 3.2.(f), black line) of a line profile along a half circle, also called arc scan. In case of the first flagellar point, the manually set flagellar starting vectors are used to set the orientation of the first arc scan at the flagellar base. Next, the arc scan with a radius of two pixels (fig. 3.2.(f), orange line) is performed at increments of 1° on the magnitude component of the nematic field leading to a sufficiently high angular resolution. Since the scan radius is additionally quite small, the arc scan profile (fig. 3.2.(g)) results from bicubic interpolation between neighbouring pixels. Thus, the profile is pretty smooth. It is used to extract the subsequent flagellar point by finding the position of highest magnitude (fig. 3.2.(g), red arrow). This point is a candidate for the new flagellar point which is only accepted if the area under the peak—calculated using the full width at half maximum—exceeds an empirically set threshold. If this point is rejected, a new arc scan with a radius increased by two pixels is performed.

The tracking procedure stops if four subsequent arc scans return no new point or if the maximum number of 40 flagellar points ($\approx 18.6 \mu\text{m}$) is reached. If a new point is successfully found (fig. 3.2.(h), red dot marked with $n + 1$), the iterative process (d–h) restarts. The results of both full flagellar tracking and cell body tracking are shown in fig. 3.2.(i).

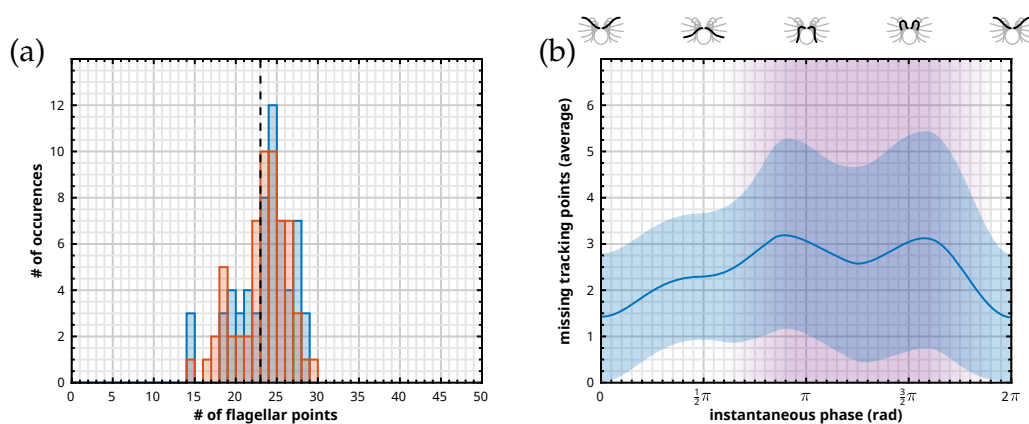


Fig. 3.3: (a) Both *cis*-flagellum (blue) and *trans*-flagellum (orange) have an average length of 23 tracking points (dashed black line) corresponding to $\approx 11 \mu\text{m} \pm 4 \mu\text{m}$ (mean \pm s.e., $n = 61$ flagella). (b) Depending on the current phase of the flagellar beat, between one and four flagellar points are missing on average (blue line). The shaded blue region indicates the mean \pm s.e. of missing flagellar points. During the recovery stroke (lilac area), the flagella come so close to the cell body that they are partially removed by the mask which is actually used to remove only the cell body. Therefore, more flagellar points are missing during the recovery stroke than during the power stroke.

Phase-dependent tracking performance. The performance of the full flagellar tracking code depends on the current phase of the flagellar beat. On average, both *cis*- and *trans*-flagellum are tracked almost entirely with just two missing tracking points. Compared to the average flagellar length of 23 tracking points, see fig. 3.3.(a), the error due to inter- or extrapolation of these few points is negligible. Taking a closer look at the number of missing points as a function of the flagellar phase, more points are missing during the recovery stroke than during the power stroke, see fig. 3.3.(b). The reason for this relation is the fact that during the recovery stroke, parts of the flagella are very close to the cell body. Masking in order to remove the cell body and, thus, increase the contrast of the flagella accidentally removes parts of the flagella as well. This effect is enhanced due to external flow which pushes the flagella even closer to the cell body. Mostly, the distal end of the flagellum remains untracked instead of single points along the flagellum, see fig. 3.4. Therefore, information of the flagellar shape during the recovery stroke is lost and cannot be recovered.

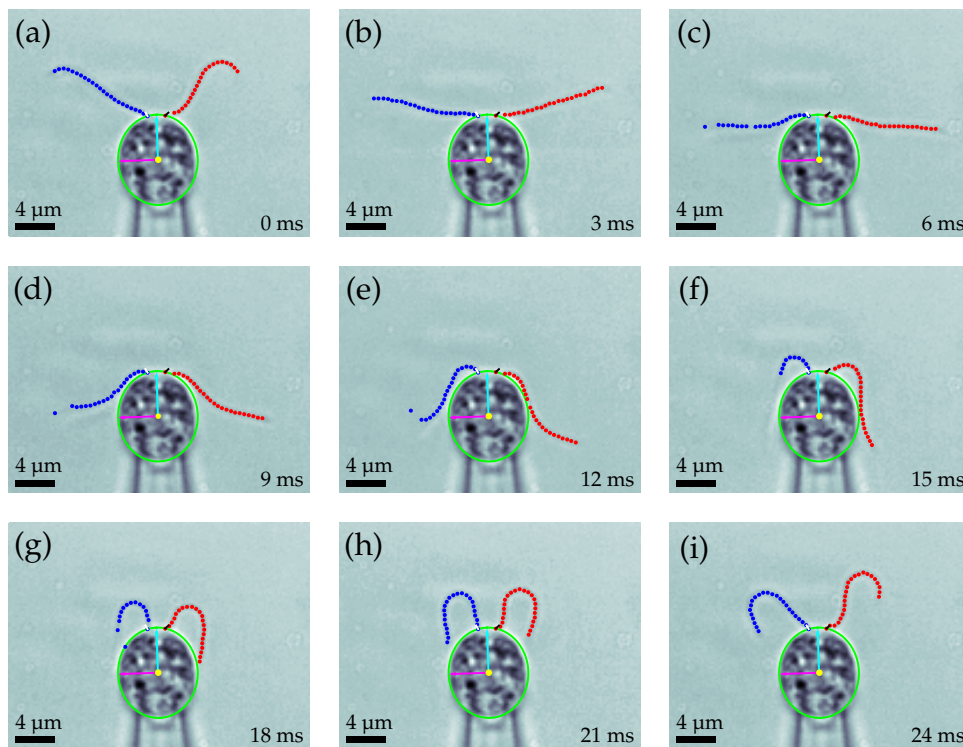


Fig. 3.4: Experimentally determined shapes during one cycle of *C. reinhardtii*'s flagellar beat at intervals of 3 ms. The flagellar beat can be divided into two kinds of strokes, the power stroke (a–e) and the recovery stroke (f–i).

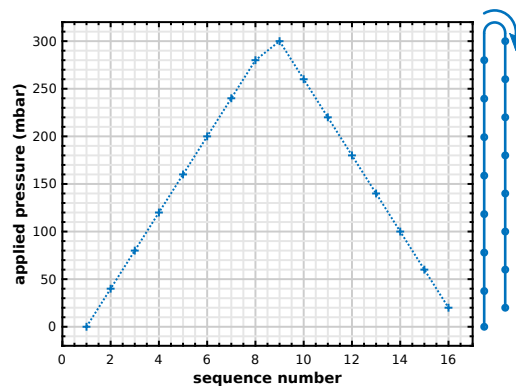


Fig. 3.5: Visualisation of the measurement protocol used for load response experiments which consist of 16 individual sequences, i.e. 16 different applied pressures. The identical pressure ramps are used for all microfluidic chips. Using their individual characteristic calibration curve (see fig. 2.10), applied pressures are translated to flow velocities.

3.1.2 Measurement protocol

Since we focused on moderate flow velocities up to 2 mm/s in order to determine the load response of the flagellar beat, the camera's *ring mode* was used to record 16 different flow conditions subsequently without the need to intermediately transfer data to the PC. In this operation mode, the total camera memory is divided into 16 sequences, and the frame size of the image defines the recording duration available per sequence.

Measurements are performed in a circadian manner, see fig. 3.5: First, the desired pressure, i.e., the desired flow velocity, was set and *Chlamydomonas reinhardtii* were allowed to acclimatise for 30 s to it. This acclimatisation time additionally serves as a guarantee that the desired flow profile due to the applied pressure has already developed. Afterwards, image sequences were recorded for 10 s at a framerate of 1 kHz leading to a recording of approximately 400 beat cycles per flow condition sampled every millisecond. By setting the next pressure, the cycle continues.

In total, recordings of eight sequences of increasing pressure are followed by eight sequences of decreasing pressure without measuring the same pressure twice, i.e., starting with 0 mbar, the pressure was increased in steps of 40 mbar up to 280 mbar, then the next sequence is recorded at 300 mbar followed by reducing the pressure in steps of -40 mbar down to 20 mbar. After all sequences have been recorded and while data is transferred to the connected PC, the location of the eyespot was determined under white light conditions permitting the differentiation between *cis*- and *trans*-flagellum.

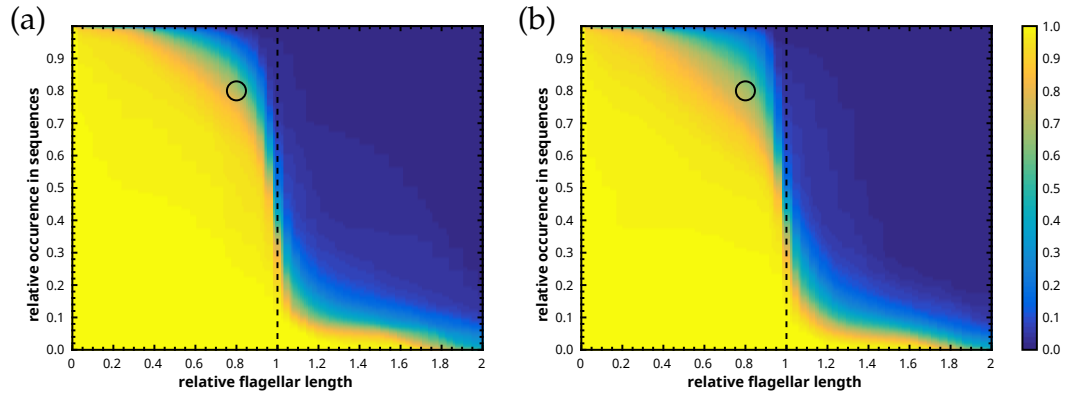


Fig. 3.6: The probability of tracking a flagellum up to a certain length (scaled with the real flagellar length, indicated by the dashed black line, for each flagellum, individually) in a certain number of sequences (scaled with the total number of sequences of the respective measurement) is shown color-coded for *cis*- and *trans*-flagellum, individually. The black circle marks our chosen quality standard.

Quality standards. Preceding evaluation tests with *C. reinhardtii* showed that the cells usually survive micropipettes fixation in combination with the intense illumination, which is necessary for high speed image recordings, for approximately one hour. However, cells might show uncharacteristic behaviour earlier. In general, all cells showing obvious functional defects were discarded. Additionally, in order to reliably identify and discard cells which show a pronounced time dependency, measurement protocols comprise both an increase in flow followed by a subsequent decrease in flow, or vice versa. We restrict our analysis to high quality data sets, i.e., the tracking results must fulfil the following criteria:

- ▷ In over 80% of all frames, at least one flagellum is aligned in such a way that over 80% of the flagellar length is tracked successfully, see fig. 3.6.
- ▷ In over 80% of the time, both flagella have to show in-phase synchronised beating at the natural frequency of ≈ 50 Hz if no external flow is applied.

All of these restrictions reduce the amount of available data sets from more than 36 flagella (of 18 independent single cell experiments) down to $n = 6$ flagella.

3.1.3 Principle component analysis and limit cycle representation

The basic idea is to model the flagellar beat as an phase oscillator [36, 39, 131] meaning that flagellar dynamics are described by the oscillator amplitude $A(t)$ and the constantly increasing oscillator phase $\varphi(t)$. In the case of no external perturbations and no intrinsic fluctuations, the amplitude is constant, i.e., $A(t) = A_0$,

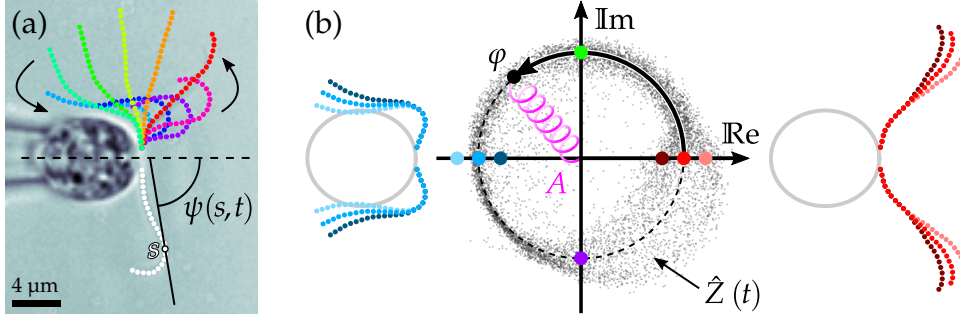


Fig. 3.7: (a) The high-dimensional tangent angle representation $\psi(s, t)$ is processed using principle component analysis to describe the flagellar beat in terms of beating modes $\tilde{\psi}_n(s)$ which contribute by their scores $\beta_n(t)$ to the full flagellar beat description. (b) The flagellar shape $\hat{Z}(t)$ (grey dots) constructed using only the first two scores $\beta_1(t)$ and $\beta_2(t)$ jitters around the reconstructed limit cycle $\bar{Z}(\varphi)$ (dashed black line). While the phase $\varphi(t)$ describes the current position of the flagellum in the course of the beat cycle, the amplitude $A(t)$ describes its current state, i.e., how the shape of the flagellum is altered. An amplitude of $A(t) > 1$ corresponds to a higher overall curvature of the flagellum, while $A(t) < 1$ describes a less curved flagellum.

and the oscillator phase increases at $\dot{\varphi}(t) = \dot{\varphi}_0 (= 2\pi f_0)$. The fact that the flagellar beat is stable in time means that it can be described by a limit cycle.

By means of our tracking algorithm, flagellar shapes are represented as cartesian coordinates. Since the distance between two subsequent data points is constant by design, flagellar shapes can be described solely by their tangent angle $\psi(s, t)$ for each flagellar point $s = 1 \dots S$ at times $t = 1 \dots T$ [105], see fig. 3.7.(a). However, the flagellar motion is a high-dimensional problem. In order to reduce the dimensionality and thus the complexity of description, though preserving the features of the flagellar beating, a principle component analysis is performed [133].

Therefore, the measured tangent angles $\psi(s, t)$ are decomposed by means of singular value decomposition into eigenmodes, or beating modes, $\tilde{\psi}_n(s)$ contributing by their corresponding eigenvalues, or scores, $\beta_n(t)$ more or less significantly to the full flagellar beat description. To account for cell specific deviations of flagellar beating, the time-averaged value $\langle \psi(s, t) \rangle_t = \psi_0(s)$ calculated for the no flow case is subtracted from all tangent angles at all recorded flow velocities:

$$\psi(s, t) - \psi_0(s) = \sum_{n=1}^S \beta_n(t) \tilde{\psi}_n(s) \quad (3.1)$$

In order to be able to compare different data sets, shape modes calculated for one random measurement act as reference modes meaning that the scores of all measurements are calculated based on these reference modes. We find that only the first two modes $\tilde{\psi}_1(s)$ and $\tilde{\psi}_2(s)$ contribute significantly to the tracked flagellar

shape, thus the scores β_1 and β_2 are sufficient to describe the flagellar beat. Both scores are used to construct the complex oscillator variable

$$Z(t) = \beta_1(t) + i\beta_2(t) \quad (3.2)$$

which approximates the full flagellar dynamics by only two parameter: the geometrical phase, or protophase, $\theta = \arctan(\beta_2(t) / \beta_1(t))$ and the corresponding amplitude $A(t) = |Z(t)|$. In general, the protophase θ does not advance at constant speed, hence $\partial_t^2 \theta \neq 0$. Therefore, θ is transformed to the real flagellar phase φ by using a phase reconstruction technique [68] which ensures that $\partial_t \varphi(t) = \text{const.} = \dot{\varphi}$, leading to

$$\hat{Z}(t) = A(t) e^{i\varphi(t)}. \quad (3.3)$$

Experimental noise is averaged out by reconstructing a limit cycle $\bar{Z}(\varphi)$ [78, 133] around which the complex oscillator variable $\hat{Z}(t)$ is fluctuating in time, see fig. 3.7.(b). In order to relate every flagellar shape to a unique phase φ , $\hat{Z}(t)$ is radially projected onto $\bar{Z}(\varphi)$. The result is a time-independent description of the flagellar beat parameterised by the phase φ . The limit cycle calculated in the case of no external flow \bar{Z}_0 represents the reference case and is used to normalise every limit cycle. Consequently, this transformation maps the limit cycle in the case of $u = 0$ mm/s onto the unit circle. Cell-to-cell variances are taken into account by performing this transformation for each cell, individually. Defining the normalised amplitude

$$A(\varphi) = |\bar{Z}(\varphi)| / |\bar{Z}_0|, \quad (3.4)$$

the flagellar shape is given by

$$\hat{Z}(\varphi) = A(\varphi) e^{i\varphi}. \quad (3.5)$$

The phase φ defines the current position of the flagellum in the course of the beat cycle and the amplitude $A(\varphi)$ describes its current state, i.e., how the flagellum deforms under the influence of external flow: If $A(\varphi) > 1$, the overall curvature of the flagellum is increased while in the case of $A(\varphi) < 1$, the flagellum is less curved. Hence, in combination with the additionally observable changes in phase speed $\dot{\varphi}(\varphi)$, the limit cycle $\hat{Z}(\varphi)$ is indeed a measure for deviations from the reference case \bar{Z}_0 .

Note that using this mode decomposition technique, the flagellar beating is, as in previous studies [73, 131], represented by a single moving point. However, in the representation used here, the moving point stands for an entire flagellar shape and not only for a single, fixed point, revolving in real space, on the flagellum itself.

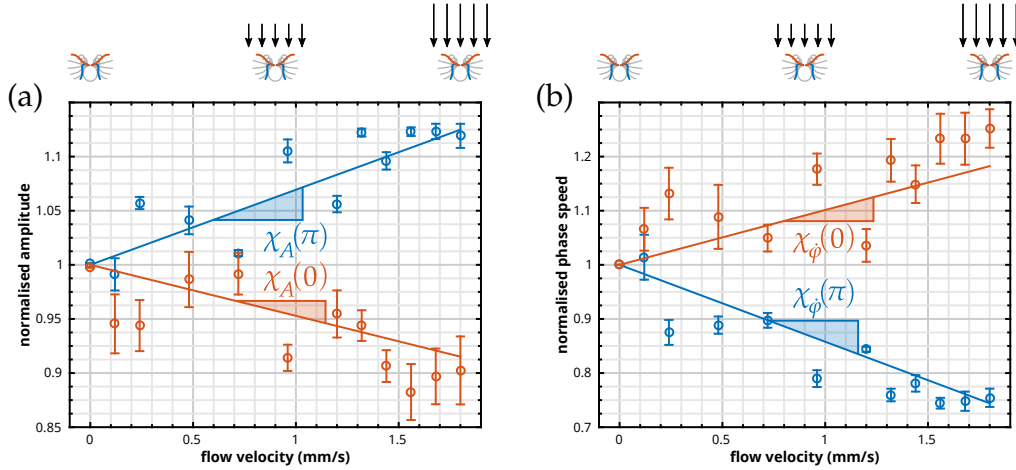


Fig. 3.8: (a) Normalised amplitude $A(\varphi)/A_0(\varphi)$ and (b) normalised phase speed $\dot{\varphi}(\varphi)/\dot{\varphi}_0(\varphi)$ as a function of the external flow velocity u for a flagellar phase during the power stroke (orange) and the recovery stroke (blue), respectively. During the power stroke, the amplitude decreases linearly with increasing flow velocity while the phase speed increases linearly with increasing flow velocity, i.e., the power stroke speeds up and the flagella are less curved. During the recovery stroke, the phase speed decreases linearly with increasing flow velocity while the amplitude increases linearly with increasing flow velocity, i.e., the flagella are more curved and thus closer to the cell body, and the recovery stroke slows down. The slopes of the linear relationships, the susceptibilities $\chi_A(\varphi)$ and $\chi_{\dot{\varphi}}(\varphi)$, characterise the change of amplitude and phase speed as a function of the external flow velocity u , respectively. Underlying experimental data were collected by the author, its evaluation was performed by Gary S. Klindt.

Flow induced changes in phase speed and amplitude. Under external flow conditions, flagellar dynamics are consistently altered. Fig. 3.8 shows the effect of positive external flow $u > 0$ mm/s, i.e., the cell is swimming against the flow. Depending on the current phase during the beat cycle, both phase speed and amplitude change differently. For a fixed φ , individual linear regressions of the normalised phase speed $\dot{\varphi}(\varphi)/\dot{\varphi}_0(\varphi)$ and the normalised amplitude $A(\varphi)/A_0(\varphi)$ as a function of the applied external flow velocity u are performed according to

$$\frac{\dot{\varphi}(\varphi)}{\dot{\varphi}_0(\varphi)} \approx 1 + \chi_{\dot{\varphi}}(\varphi) \cdot u \quad \text{and} \quad \frac{A(\varphi)}{A_0(\varphi)} \approx 1 + \chi_A(\varphi) \cdot u, \quad (3.6)$$

respectively. The slopes of the linear regressions, the phase speed susceptibility $\chi_{\dot{\varphi}}(\varphi)$ and the amplitude susceptibility $\chi_A(\varphi)$, can be used to quantify the influence of external flow.

A susceptibility of $0(\text{mm/s})^{-1}$ implies that the external flow does not have an influence at all. We find that during the power stroke, the phase speed increases leading to $\chi_{\dot{\varphi}}(\varphi = 0) > 0(\text{mm/s})^{-1}$ while during the recovery stroke, the phase speed decreases, i.e., $\chi_{\dot{\varphi}}(\varphi = 0) < 0(\text{mm/s})^{-1}$. Additionally, during the recov-

ery stroke, the flagella are pushed closer to the cell body and, consequently, $\chi_A(\varphi = 0) > 0 (\text{mm/s})^{-1}$. Due to the asymmetry of the flagellar beat, the increase of $\dot{\varphi}$ during the power stroke is not compensated by the decrease of $\dot{\varphi}$ during the recovery stroke and thus, a net increase in phase speed $\dot{\varphi}$ with increasing external flow u is observable.

3.1.4 Theoretical model for flagellar oscillations

The theoretical model described here was developed by Gary S. Klindt and Benjamin M. Friedrich from the Max Planck Institute for the physics of complex systems in Dresden.

In order to predict the measured susceptibilities for phase speed, $\chi_{\dot{\varphi}}(\varphi)$, and amplitude, $\chi_A(\varphi)$, a theoretical model inspired by the analysis technique of the experimental data is presented, see fig. 3.9. This model does not depend on any specific assumptions regarding the detailed mechanisms inside the flagellum, e.g., motor distribution, motor control, or internal structures leading to friction. In principle, this model is applicable to any type of flagellum or cilium whose beating dynamics can be described by means of a limit cycle and, if the cell has more than one flagellum like *C. reinhardtii*, beating is perfectly symmetric. In this case, the flagellar dynamics can be described by only three degrees of freedom: the phase φ and the one-dimensional, scalar amplitude A —both parameters which correspond to the flagellum itself—as well as the position of the cell along its swimming direction, here y . Therefore, the generalised coordinates are $\mathbf{q} = [\varphi, A, y]'$ and the generalised velocities read $\dot{\mathbf{q}} = [\dot{\varphi}, \dot{A}, \dot{y}]'$. The fact that the cell is fixed but exposed to an external flow u is incorporated into the description by setting $\dot{y} = u$.

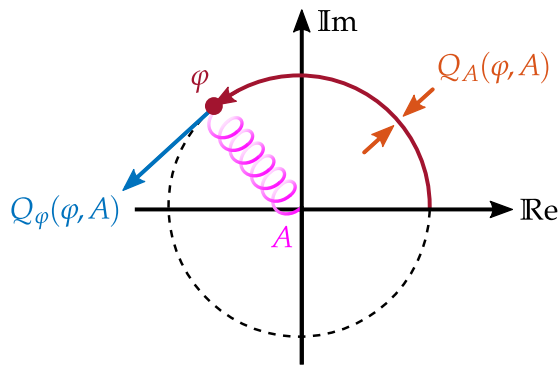


Fig. 3.9: The flagellar beat is described as a limit cycle oscillator with amplitude A and phase φ . Stability of the limit cycle is ensured by the active flagellar amplitude force Q_A which, together with the active flagellar driving force Q_φ , coarse-grains active dynamics of the dynein motors distributed along the microtubules inside the flagellum.

The totally available energy provided by ATP is either dissipated internally due to friction inside the flagellum, or hydrodynamically due to friction between the flagellum and the surrounding fluid. Thus, the dissipation rate reads

$$\mathcal{R} = \mathcal{R}^{(i)} + \mathcal{R}^{(h)} = \left[\mathbf{P}^{(i)} + \mathbf{P}^{(h)} \right]' \dot{\mathbf{q}} \quad (3.7)$$

with $\mathbf{P}^{(i)}$ and $\mathbf{P}^{(h)}$ being the generalised internal friction forces and the generalised hydrodynamic friction forces, respectively. Since friction forces are linearly related to corresponding velocities in the low Reynolds number regime [71],

$$\mathbf{P}^{(i)} = \underline{\underline{\Gamma}}^{(i)}(\varphi, A) \dot{\mathbf{q}} \quad \text{and} \quad \mathbf{P}^{(h)} = \underline{\underline{\Gamma}}^{(h)}(\varphi, A) \dot{\mathbf{q}}. \quad (3.8)$$

In general, the efficiency of the flagellar beat is also effected, e.g., by internal friction due to viscoelastic structures like nexin fibres inside the flagellum or due to incomplete conversion of ATP which can also be modelled as a kind of internal friction. Lacking accurate knowledge on these processes, it is assumed that only a fraction $\eta = \mathcal{R}^{(h)}/\mathcal{R}$ is really transformed into motion leading to

$$\mathcal{R}^{(i)} = \left(\frac{1}{\eta} - 1 \right) \mathcal{R}^{(h)}. \quad (3.9)$$

Consequently,

$$\Gamma_{kl}^{(i)} = \left(\frac{1}{\eta} - 1 \right) \Gamma_{kl}^{(h)} \quad \text{and} \quad \Gamma_{ky}^{(i)} = \Gamma_{yk}^{(i)} = \Gamma_{yy}^{(i)} = 0 \quad \text{for } k, l \in \{\varphi, A\}. \quad (3.10)$$

The total friction matrix finally reads

$$\begin{aligned} \underline{\underline{\Gamma}} &= \underline{\underline{\Gamma}}^{(i)} + \underline{\underline{\Gamma}}^{(h)} \\ \Leftrightarrow \begin{bmatrix} \Gamma_{\varphi\varphi} & \Gamma_{\varphi A} & \Gamma_{\varphi y} \\ \Gamma_{A\varphi} & \Gamma_{AA} & \Gamma_{Ay} \\ \Gamma_{y\varphi} & \Gamma_{yA} & \Gamma_{yy} \end{bmatrix} &= \begin{bmatrix} \frac{1}{\eta} \Gamma_{\varphi\varphi}^{(h)} & \frac{1}{\eta} \Gamma_{\varphi A}^{(h)} & \Gamma_{\varphi y}^{(h)} \\ \frac{1}{\eta} \Gamma_{A\varphi}^{(h)} & \frac{1}{\eta} \Gamma_{AA}^{(h)} & \Gamma_{Ay}^{(h)} \\ \Gamma_{y\varphi}^{(h)} & \Gamma_{yA}^{(h)} & \Gamma_{yy}^{(h)} \end{bmatrix}. \end{aligned} \quad (3.11)$$

Note that no knowledge on internal friction is necessary and the total friction matrix can be computed solely by calculating the hydrodynamic friction forces [64]. Thus, the only free parameter is the efficiency of chemo-mechanical energy conversion η .

To deduce the equations of motion, friction forces $\mathbf{P}(\mathbf{q})$ are balanced by active flagellar driving forces $\mathbf{Q}(\mathbf{q})$ [100]. The latter, which coarse-grain active motor dynamics, are uniquely obtained by experimentally determined limit cycle dynamics

in the absence of flow. Here, $A = A_0$, $\dot{\varphi} = \dot{\varphi}_0$, and the generalised velocities thus read $\dot{\mathbf{q}}_0 = [\dot{\varphi}_0, 0, 0]'$ leading to

$$\begin{aligned} [Q_\varphi, Q_A, Q_y]'_{(\varphi, A_0)} &= [P_\varphi, P_A, P_y]'_{(\varphi, A_0)} \\ &= \underline{\Gamma}_{(\varphi, A_0)} \dot{\mathbf{q}}_0 \\ &= \dot{\varphi}_0 [\Gamma_{\varphi\varphi}, \Gamma_{A\varphi}, \Gamma_{y\varphi}]'_{(\varphi, A_0)}. \end{aligned} \quad (3.12)$$

This calibration step using experimental data is mandatory since no assumptions for active flagellar forces are made. The case of $A \neq A_0$ can be incorporated by introducing an effective amplitude spring κ_A that suppresses amplitude disturbances $\Delta A = (A - A_0)$ and thus guarantees limit cycle stability:

$$Q_A(\varphi, A) = Q_A(\varphi, A_0) - \kappa_A(\varphi) \Delta A. \quad (3.13)$$

Amplitude disturbances ΔA are assumed to decay exponentially with a characteristic relaxation time τ_A , hence

$$\tau_A \dot{\Delta A} = -\Delta A. \quad (3.14)$$

Using stability analysis [64], it can be shown that the amplitude stiffness $\kappa_A(\varphi)$ is defined as

$$\kappa_A(\varphi) = [\Gamma_{AA} - \Gamma_{A\varphi} \Gamma_{\varphi\varphi}^{-1} \Gamma_{\varphi A}] / \tau_A - [\partial_A \Gamma_{A\varphi} - \Gamma_{A\varphi} \Gamma_{\varphi\varphi}^{-1} \partial_A \Gamma_{\varphi\varphi}] \dot{\varphi}_0. \quad (3.15)$$

The only unknown parameter, the relaxation time τ_A , is assumed to not depend significantly on the current flagellar phase φ which is why the previously determined relaxation time $\tau_A = 5.9$ ms [78] was used for all calculations. Exemplary computations of active flagellar driving forces Q_φ and Q_A , and the phase-dependent amplitude stiffness $\kappa_A(\varphi)$ are shown in fig. 3.10. Note that for $\tau_A = 0$ ms, there is no amplitude compliance, i.e., the flagellar waveform does not change due to hydrodynamic load.

Since the cell is fixed by means of micropipettes, amplitude dynamics or phase dynamics do not influence the cell position y . Thus, the model reduces to $\mathbf{q} = (\varphi, A)'$ leading to

$$\begin{aligned} \overbrace{[\dot{\varphi}, \dot{A}] \cdot \begin{bmatrix} \Gamma_{\varphi\varphi}^{(h)} & \Gamma_{\varphi A}^{(h)} \\ \Gamma_{A\varphi}^{(h)} & \Gamma_{AA}^{(h)} \end{bmatrix}}^{\text{flagellar dynamics}}}_{(\varphi, A)} &= \dot{\varphi}_0 \underbrace{\begin{bmatrix} \Gamma_{\varphi\varphi}^{(h)} \\ \Gamma_{A\varphi}^{(h)} \end{bmatrix}}_{\text{experimental calibration term}}_{(\varphi, A_0)} - \eta \left[\begin{array}{c} \text{external} \\ \text{term} \\ \begin{bmatrix} \Gamma_{\varphi y}^{(h)} u \\ \Gamma_{Ay}^{(h)} u \end{bmatrix} \\ + \underbrace{\begin{bmatrix} 0 \\ \kappa_A \Delta A \end{bmatrix}}_{\text{limit cycle stability}} \end{array} \right]_{(\varphi, A)}. \end{aligned} \quad (3.16)$$

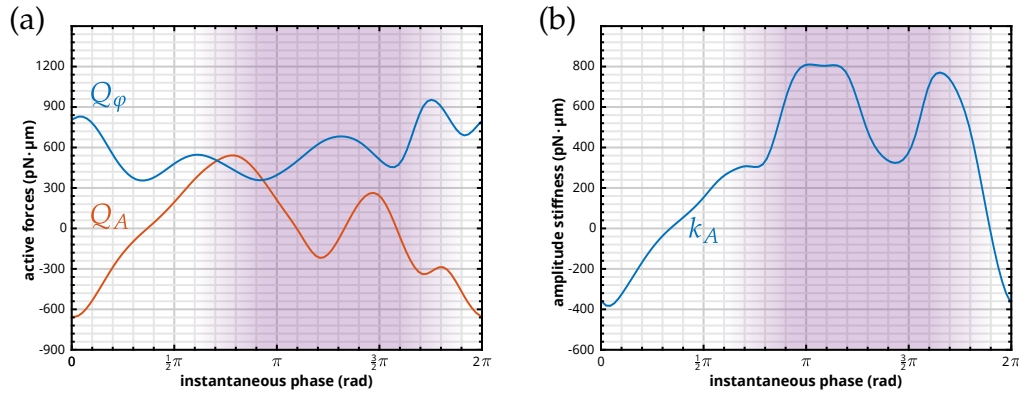


Fig. 3.10: Exemplary computations of (a) the active flagellar driving forces Q_φ and Q_A using $\eta = 0.21$ and (b) the phase-dependent amplitude stiffness $\kappa_A(\varphi)$, the latter providing limit cycle stability. Flagellar phases belonging to the recovery stroke are highlighted in lilac. Underlying numerical data were provided by Gary S. Klindt.

Here, almost all parameter can either be computed or deduced from recordings of flagellar beat pattern under no flow conditions. Only the chemo-mechanical efficiency energy conversion η remains unknown. By comparing simulations and experiments performed in the presence of external flow, η can be obtained by a simple fit. It is noteworthy that this model is applicable to all kinds of flagellar dynamics that can be described as a phase oscillator since neither details on molecular motor dynamics nor control inside the flagellum are required. Yet, the model requires calibration using experimental data under no flow conditions when flagellar dynamics are unperturbed.

3.1.5 Phase speed susceptibility and amplitude susceptibility

Both for experimental data as well as simulations based on the theoretical model, the flagellar phase speed $\dot{\varphi}(\varphi)$ and the corresponding amplitude $A(\varphi)$ were determined for different flow velocities u for each flagellar phase φ . According to eg. 3.6, $\dot{\varphi}(\varphi)$ and $A(\varphi)$ depend linearly on the applied flow with a slope of $\chi_{\dot{\varphi}}(\varphi)$ and $\chi_A(\varphi)$, respectively. Therefore, we can calculate a unique phase speed susceptibility $\chi_{\dot{\varphi}}(\varphi)$ and a unique amplitude susceptibility $\chi_A(\varphi)$ for each flagellar phase φ , see fig.3.11. In detail, we find a strong phase-dependence of both susceptibilities in the experimental data as well as in simulations:

- ▷ In general, the influence of external load on both susceptibilities is less pronounced in the simulations than it is in the experimental data.
- ▷ During the power stroke, $\chi_A < 0(\text{mm/s})^{-1}$. This means that the overall curvature of the flagellar shape is reduced under external load.

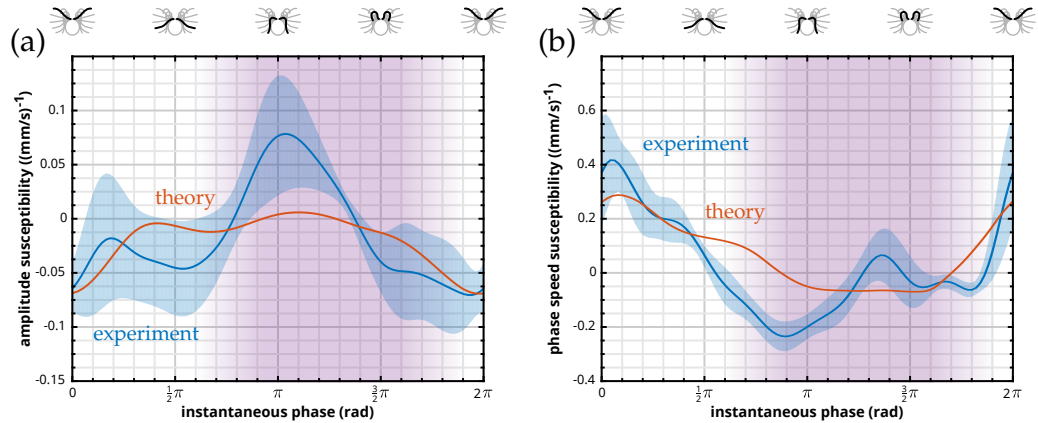


Fig. 3.11: (a) Amplitude susceptibility $\chi_A(\varphi)$ and phase speed susceptibility $\chi_{\dot{\varphi}}(\varphi)$ reveal the phase-dependent response of the flagellar beat to an external flow velocity u , i.e., to an external hydrodynamic load. The model (orange) captures the principle features of the experimental results (blue, mean \pm s.e.): the increased amplitude and the decreased phase speed during the recovery stroke as well as the increased phase speed and the decreased amplitude during the power stroke are predicted by the theoretical model, but not all experimental details are reproduced. Flagellar phases belonging to the recovery stroke are highlighted in lilac. Underlying experimental data were collected by the author, its evaluation was performed by Gary S. Klindt.

- ▷ During the recovery stroke, $\chi_A > 0$ (mm/s)⁻¹ and thus the flagella are more curved and, consequently, closer to the cell body.
- ▷ During the power stroke, $\chi_{\dot{\varphi}} > 0$ (mm/s)⁻¹, i.e., the power stroke speeds up.
- ▷ During the recovery stroke, $\chi_{\dot{\varphi}} < 0$ (mm/s)⁻¹ and the recovery stroke slows down. Yet, this slowing down is hardly overcompensated by the increase of phase speed during the power stroke which leads to a slight increase in the beating frequency.

However, several subtleties in the experimental data are not reproduced by the model. Especially in the transition regions from power stroke to recovery stroke and vice versa, experimental data and simulations differ from each other.

- ▷ In the experiment and during the transition from power stroke to recovery stroke, χ_A changes sign significantly and reaches its maximum at $\varphi = \pi$, the point in the flagellar beat cycle where the flagella start to move entirely against the external flow.
- ▷ In the simulation, χ_A is only slightly positive in a smaller region during the recovery stroke.
- ▷ During the transition from recovery stroke to power stroke, χ_A gradually decreases to its minimum at $\varphi = 0$ in the simulation while it drops faster in

the experimental data and stays almost constant. However, in both cases, the minimum of χ_A is at $\varphi = 0$.

- ▷ During the power stroke, χ_A first increases and then drops again before finally rising to its maximal value in the experimental data. This drop is also present in the simulation but much less pronounced and shifted towards a later stage of the beat cycle.
- ▷ During the recovery stroke, the difference between simulation and experiment is strongly pronounced in χ_φ . While the phase χ_φ remains almost constant but negative during the recovery stroke, χ_φ drops below zero already at the end of the power stroke.
- ▷ During the transition from power stroke to recovery stroke, χ_φ reaches its minimum in the experimental data, directly followed by an increase and even a change in sign at the end of the recovery stroke before dropping below zero again.
- ▷ During the transition from recovery stroke to power stroke, χ_φ changes sign at an earlier stage in the case of the simulation compared to the experiment.

3.1.6 Efficiency of the flagellar beat

In the theoretical model, the internal structure of the flagellum has been modelled by means of a simple ansatz: By representing all flagellar internal contributions to the dynamics of the flagellar beat by a single quantity, the conversion efficiency from ATP consumption to flagellar motion η , the complexity of the problem is heavily reduced. Albeit we do not gain any new insights in how efficient a single dynein motor works, how viscous the interior of the flagellum is, or how stiff the flagellar structure itself is, we can estimate how efficient the entire flagellar

Tab. 3.1: Comparison of flagellar efficiencies for different cell types. Despite for mammalian sperm, typical beating frequencies are in the range of 40Hz. Our value of 0.21 for the flagellar efficiency is in good agreement with reported efficiencies ranging from 0.1 to 0.4.

efficiency	beating frequency	cell type	reference
0.1	40	<i>Paramecium caudatum</i>	[61]
0.15 - 0.35	8	mammalian sperm (rat, mouse)	[25]
0.21	50	<i>C. reinhardtii</i> (SAG 11-32c mt-)	[64]
0.4	30	<i>Tetrahymena pyriformis</i>	[11]

machinery is by fitting the theoretical simulations to the experimental data. For the eukaryotic flagellum of *C. reinhardtii* (SAG 11-32c mt-), we find

$$\eta = \underset{\text{(mean)}}{0.21} \pm \underset{\text{(s.e.)}}{0.06}. \quad (3.17)$$

Previously reported efficiency values, including the one determined in this work, are being compared in tab. 3.1.

3.1.7 Comparison of eukaryotic flagella with a combustion engine

At first sight, a eukaryotic flagellum and a combustion engine do not seem to have much in common. However, appearances are deceiving. Both the eukaryotic flagellum and a combustion engine are complex machines, yet on different length scales, transforming chemical energy to mechanical work by burning fuel: in the case of the flagellum, the fuel is ATP and in the case of the combustion engine, it is petrol or diesel fuel. From an efficiency point of view, both engines are very similar as well. Typically, combustion engines have an efficiency of $\approx 40\%$ if operated under optimal conditions. In real use cases, efficiency significantly drops to $\approx 20\%$ [29]. Similar values are reached by eukaryotic flagella, hence on a much smaller length scale and at much lower temperatures and pressures: In a petrol engine, fuel is burned at 2000°C at a pressure of up to 18 bar, while a flagellum works under standard conditions of 20°C and 1 bar. The Gibbs free energy of ATP hydrolysis used by the flagellum to power its beat is in the range of 50 kJ/mol and thus 100 times smaller than to the energy generated in a combustion engine.

3.2 Dynamic modes of flagellar beating

So far, we only considered the case of flow velocities below 3 mm/s and in opposite direction to the swimming direction. Indeed, in this region, the flagellum responds with a linear increase in beating frequency to increasing load. However, for higher flow velocities, the eukaryotic flagellum of *Chlamydomonas reinhardtii* behaves remarkably: On further increasing load, the flagellum switches dynamically between different beating modes which we call tremor-like beating, see fig. 3.13, and chiral beating, see fig. 3.14. Consequently, the flagellum does not respond solely with a change in frequency, but with a change in flagellar waveform as well. These beating modes are unique to the case of flow in opposite direction to the swimming direction and cannot be observed for the reversed flow direction. Albeit these beating modes haven't been observed experimentally so far, the existence of possible different beating modes has been predicted theoretically in [24]. Above a

certain critical flow velocity, the flagellar beat stalls. However, the required velocity significantly depends on the direction of the applied load.

A third beating mode, see fig. 3.12, is similar to the photoshock response of *C. reinhardtii*, yet the illumination was constant all the time when this beating mode was observed. Since this beating mode does not depend on the direction of the imposed flow and was only observed for three out of 60 cells, its occurrence seems to be related to a defective cell, and is therefore not considered as a regular response of the flagellum to external load.

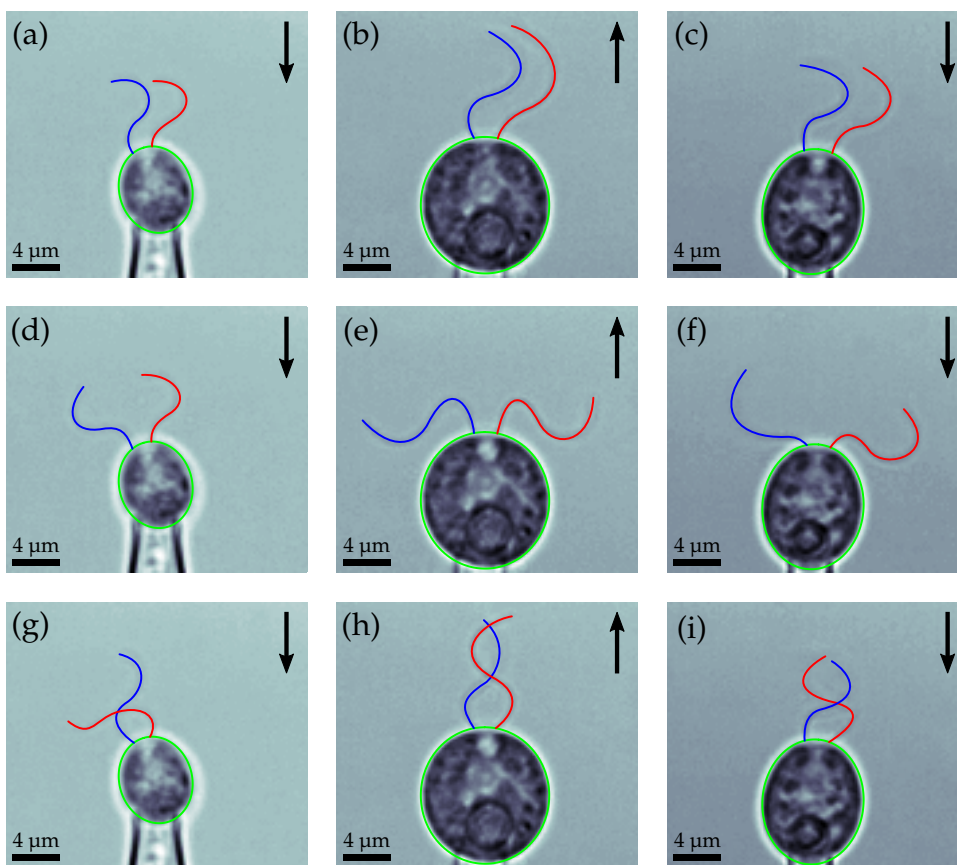


Fig. 3.12: Different stages of a photoshock-like response of *C. reinhardtii*, a whip-like beating pattern which is very rare—it was observed only for three out of 60 cells—and independent of the imposed flow speed or direction. (a–c) shows anti-phase beating of both flagella, (d–f) a stage during in-phase beating when the flagella are separated the most, and (g–i) a stage during in-phase beating when the individual flagellar shapes overlap but not entangle. (a, d, g), (b, e, h), and (c, f, i) correspond to one cell, respectively. Both *cis*-flagellum (red) and *trans*-flagellum (blue) show identical behaviour. The arrows visualise the flow direction.

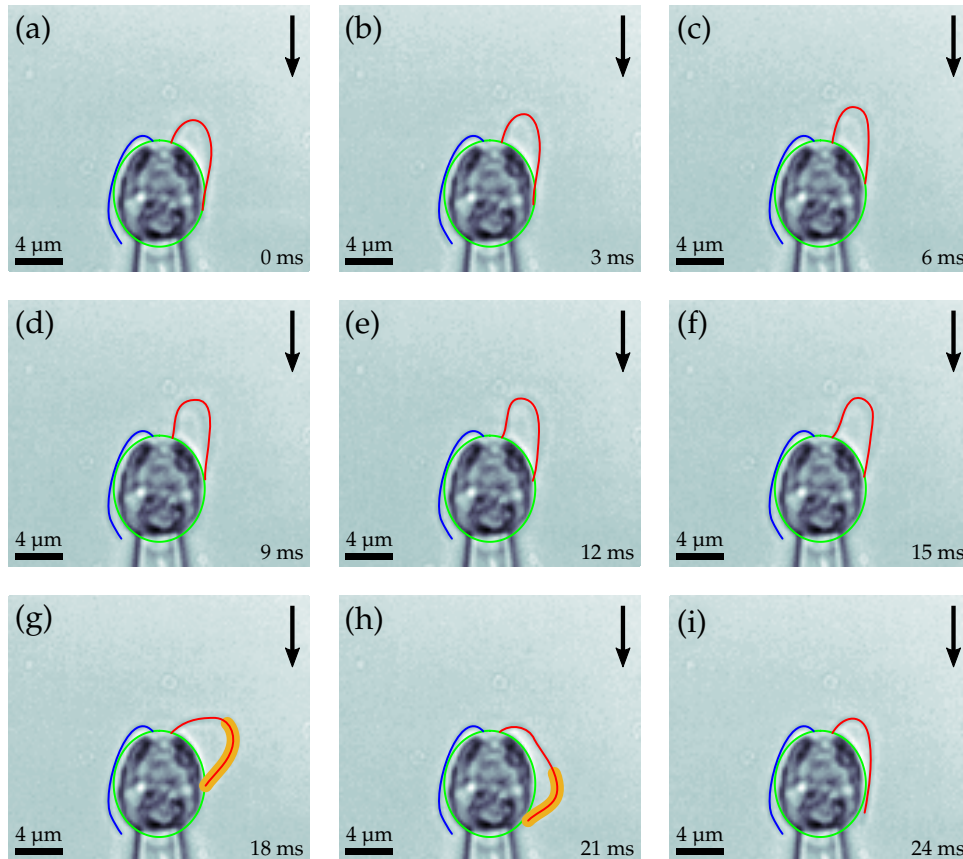


Fig. 3.13: While the *trans*-flagellum (blue) already stalls, the *cis*-flagellum (red) shows tremor-like beating at a flow velocity of 6.8 mm/s. Here, one beat cycle corresponding to a beat frequency of ≈ 50 Hz is shown at increments of 3 ms. Tremor-like beating is characterised by a significant part of the flagellum—usually half of the flagellum (highlighted in yellow)—not contributing to the beating pattern any more, as it can be seen clearly in (g) and (h).

Tremor-like beating. During tremor-like beating, the flagellar bending wave does not propagate to the distal end of the flagellum any more. Throughout the recovery stroke and during the beginning of the power stroke, the first half of the flagellum still performs its beating motion. The rest of the flagellum remains in a slightly curved configuration, see yellow highlight in fig. 3.13. This configuration changes only slightly within the entire beat cycle and can be considered as quasi-constant. In the middle of the power stroke, the first half of the flagellum cannot withstand the flow induced load anymore. The phase speed increases dramatically in this phase of the beat cycle until the transition point to the recovery stroke is reached. From a waveform point of view, both the power stroke and the recovery stroke are altered during tremor-like beating compared to normal beating. As in the case of normal beating, the flagellar bending stays planar, i.e., remains in the focal plane of observation. Tremor-like beating shows the beating frequency does not depend

on the applied flow velocity. For most of the flagella, no matter if *cis* or *trans*, the beating frequency remains at a high value, usually slightly below 50 Hz, see also fig. 3.19.(b, d, e, f). However, some cells show tremor-like beating at around 40 Hz, too, see also fig. 3.19.(a, c).

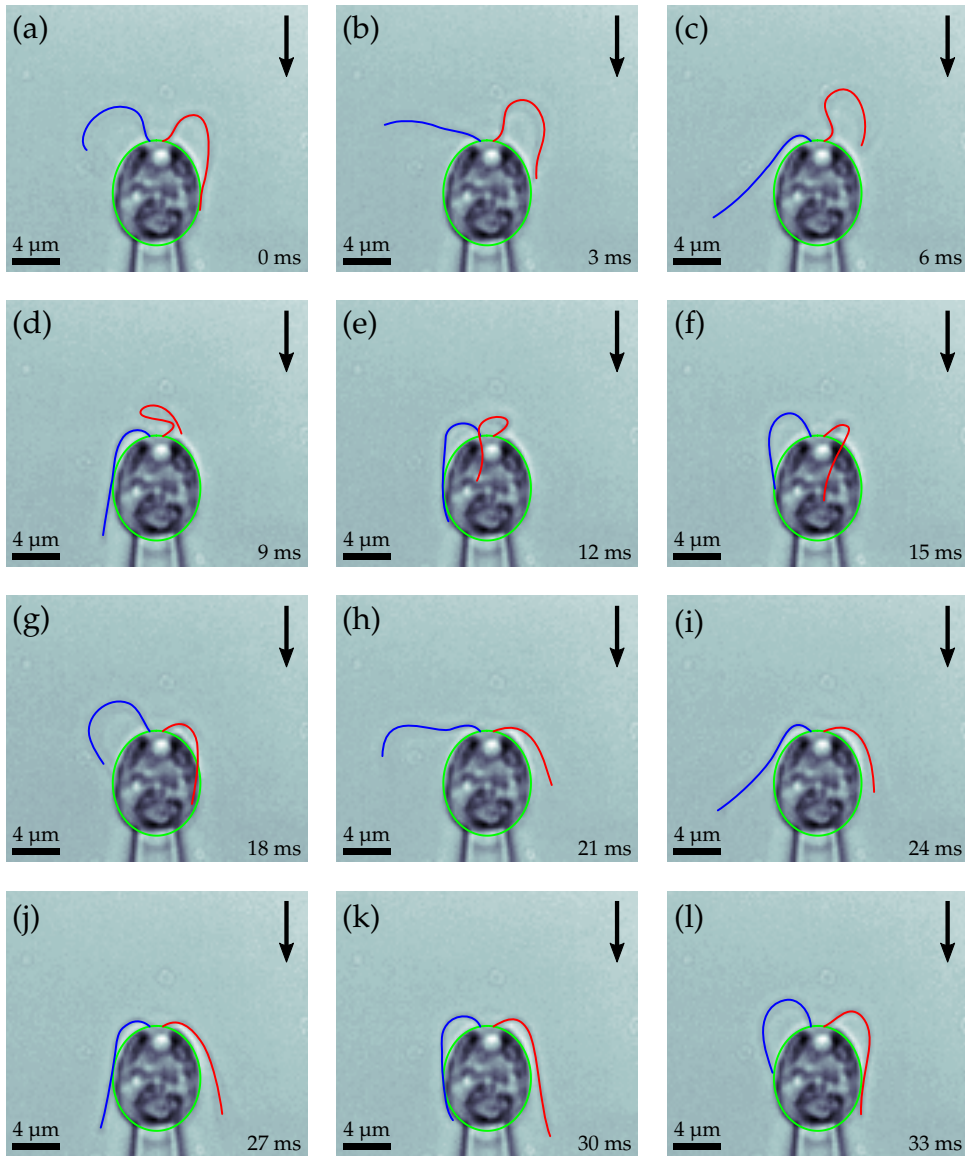


Fig. 3.14: While the *trans*-flagellum (blue) is beating normally, the *cis*-flagellum (red) shows chiral beating at a flow velocity of 5 mm/s. Here, the flagellar movement has a significant out-of-plane component. One beat cycle of chiral beating is shown at increments of 3 ms. Its frequency is with ≈ 30 Hz) way lower than the normal beating frequency of ≈ 55 Hz.

Chiral beating. Chiral beating, which is almost exclusive to the *cis*-flagellum, is different in a sense that it has a pronounced out-of-plane component, see fig. 3.14. On the transition from the recovery stroke to the power stroke, the flagellum does not reach out to its maximum but out of the former beating plane and flips over to the other flagellum. The flagellum then swipes along the cell body until it reaches, both in phase and shape, the transition point from power stroke to recovery stroke. From a waveform point of view, the recovery stroke itself is almost identical to the recovery stroke of normal beating, i.e., only the power stroke is altered during chiral beating. However, the frequency of chiral beating drops significantly to 30 Hz, see also fig. 3.19.(c, e, f), and is mostly independent on the applied load over a wide range of flow velocities

3.2.1 Data evaluation

Minimal flagellar tracking. In order to determine beating frequencies and flagellar synchrony, not the entire flagellum has to be tracked. Since knowledge of the dynamics of the first one to two microns at the proximal end of the flagella is sufficient, only this part is tracked by means of seven arc scans which are performed in an angular range from -45° to 45° centred around the orientation of the cell's major axis, see fig. 3.15. The centre of mass of the cell body acts as the centre of

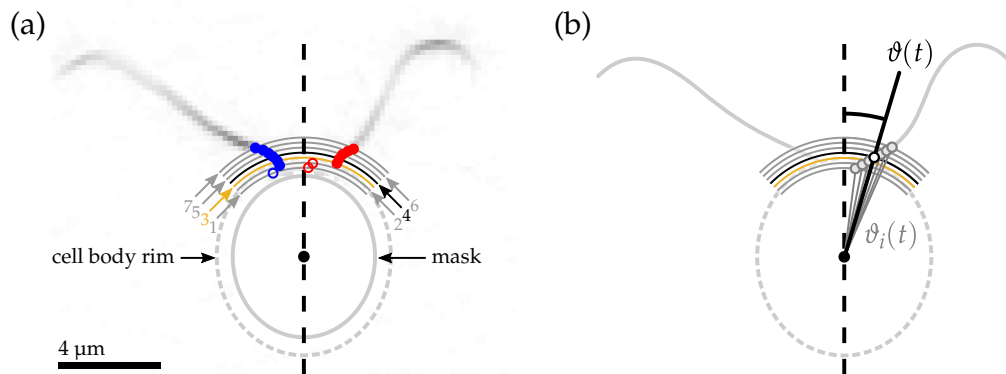


Fig. 3.15: (a) Visualisation of the arc scan procedure in the case of over-estimation of the cell body rim, highlighting the need of using a smaller mask (dashed grey ellipsoid) to remove the cell body. The centre-of-mass of the cell body (black dot) is used to construct seven arc scans (grey lines) with different radii. The previously determined cell body orientation (dashed black line) separates left flagellum (blue dots) from right flagellum (red dots). Solid symbols show true flagellar points while open symbols correspond to outliers. The radius of the yellow highlighted arc scan corresponds to the length of the cell's major axis, i.e., to the position of the cell rim. (b) Radial projection of tracked points onto the central arc (black line) and angular averaging leads to a single point for each flagellum, respectively. Its polar angle $\vartheta(t)$ with respect to the cell body orientation is used to describe flagellar dynamics.

these arc scans which are performed close to the cell body rim. Therefore, over- or under-estimation of the size of the cell body have to be considered:

- ▷ The radius of the third arc scan (see fig. 3.15, yellow arc) matches the size of the cell body, i.e., the radius of this arc scan is half of the length of the major axis determined previously.
- ▷ The mask generated to remove the cell body is calculated using smaller cell body dimensions and the radii of two arc scans (see fig. 3.15.(a), labelled with 1 and 2) are smaller than the determined cell body size by two pixels and one pixel, respectively, which accounts for size over-estimation (one pixel \equiv 233.33 nm, see sec. 2.2). If the cell body size has been determined correctly, these arc scans track points within the cell body, thus adding wrong data.
- ▷ Four arc scans (see fig. 3.15.(a), labelled with 4–7) are by increments of one pixel larger than the determined cell body size in order to account for size under-estimation. If the cell body size has been determined correctly, arcs scans 6 and 7 track wrong or no points at all, thus adding wrong data, too. However, if the size has been under-estimated, arc scans 6 and 7 indeed track flagellar points.

This tracking procedure is faster and less demanding regarding image quality but still, the flagellar phases can be determined reliably: Flagellar points (fig. 3.15.(a), blue and red symbols) are represented by their angular position $\vartheta_i(t)$ on the individual arc scan. After radially projecting the flagellar points onto the central arc (fig. 3.15, black arc), outliers (fig. 3.15.(a), open blue and red symbols) are identified. The tracked point $\vartheta_i(t)$ is removed if angular differences $\Delta\vartheta_i(t) = \vartheta_{i+1}(t) - \vartheta_i(t)$ deviate from their median value by more than half of the respective standard deviation. Finally, removed points are linearly inter- or extrapolated. After angular averaging of the seven flagellar points, flagellar dynamics are described by a single point $\vartheta(t)$ (fig. 3.15.(b), open black point) which is periodically moving left and right along the central arc.

Processing of tracking data. A typical result, obtained by this minimal tracking procedure, is shown in fig. 3.16.(a). In order to assign a unique protophase $\theta(t)$ to every $\vartheta(t)$, which is necessary for the analysis of flagellar synchrony, Hilbert transform of $\vartheta(t)$,

$$\mathcal{H}\{\vartheta(t), \langle\vartheta(t)\rangle_t\} = \frac{1}{\pi} \int_{-\infty}^{\infty} \frac{\vartheta(t) - \langle\vartheta(t)\rangle_t}{t - t'} dt', \quad (3.18)$$

was used to reconstruct the corresponding oscillator variable

$$Z(t) = \vartheta(t) + i\mathcal{H}\{\vartheta(t), \langle\vartheta(t)\rangle_t\} = A(t) e^{i\theta(t)} \quad (3.19)$$

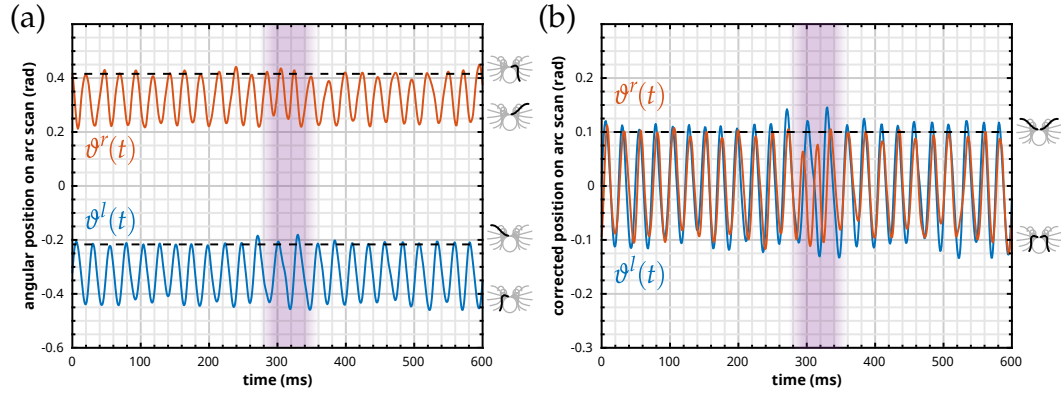


Fig. 3.16: (a) Tracking data of the left flagellum (blue) and the right flagellum (orange) before correction. Local maxima correspond to the protophase $\theta(t) = 0$ after Hilbert transform (dashed black line). In the case of the left flagellum, $\theta(t) = 0$ and the beginning of the power stroke coincide. However, $\theta(t) = 0$ corresponds to the beginning of the recovery stroke of the right flagellum. (b) After correction, $\theta(t) = 0$ indeed indicates the beginning of the power stroke for both the left and the right flagellum. Prior to Hilbert transform, $\vartheta^l(t)$ and $\vartheta^r(t)$ are centred by subtracting the corresponding time average. The lilac shading highlights a phase slip event.

from which the protophase $\theta(t)$ was deduced for each flagellum, individually. The protophase $\theta(t) = 0$ corresponds to the point where $\vartheta(t)$ is maximal. As it can be seen in fig. 3.16.(a) for the left flagellum—the flagellum whose mean value of $\vartheta(t)$ is smaller than the cell body orientation—the maximum of $\vartheta^l(t)$ marks the transition point from recovery stroke to power stroke. However, in the case of the right flagellum, the maximum of $\vartheta^r(t)$ marks the transition point from power to recovery stroke. The transform $\vartheta^r(t) \rightarrow -\vartheta^r(t)$ guarantees that both the maximum of $\vartheta^l(t)$ and the maximum of $\vartheta^r(t)$ indicate the transition from the recovery stroke to the power stroke, see fig. 3.16.(b).

Note that protophases which have been determined by principle component analysis, see chap. 3.1.3, phase lag protophases which have been determined via Hilbert transform: In the first case, the flagellar shape that is solely described by the first fundamental mode ψ_1 , i.e., $\beta_1 \neq 0$ and $\beta_2 = 0$, corresponds to $\theta(t) = 0$, which describes a flagellar shape during the power stroke while in the latter case, the protophase $\theta(t) = 0$ describes the beginning of the power stroke. However, this fact is not important since we are not differentiating between power stroke and recovery stroke anymore but considering phase differences and frequencies.

Determination of the flagellar beating frequency. Flagellar beating frequencies have been determined using *short-time Fourier transform* (STFT). STFT is a Fourier-related transform with a small but notable difference: The signal of total length T ,

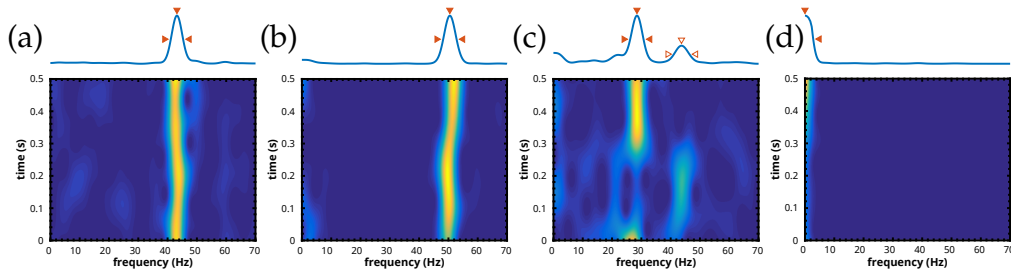


Fig. 3.17: Exemplary spectrograms and corresponding, time averaged frequency spectra in the case of (a) no flow, (b–c) medium flow, and (d) strong flow. The frequency peak is very sharp and well distinguishable from the background. These frequency spectra are typical for normal beating (a–b), chiral beating (c, lower frequency peak) and tremor-like beating (c, higher frequency peak), and stalling of the flagellar beat (d). Solid orange triangles indicate the most prominent beating frequency as well as the corresponding peak width. Open orange triangles indicate less pronounced frequency peaks which are not shown in fig. 3.19 and fig. 3.20 for the sake of clarity.

here the tracked flagellar point $\vartheta(t)$, is split up into smaller blocks of fixed length l . A small block size is desired for high temporal resolution, yet a large block size is mandatory for high frequency resolution. In order to reduce artefacts at the boundaries, these blocks usually overlap. To ensure the periodicity of each block, it is multiplied with a window function. The use of a Gaussian as a window function leads to the best resolution in both frequency and time. In the special case of using a Gaussian as the window function, the SFTF is also called *Gabor transform*. Finally, each block is Fourier-transformed individually, and the magnitude squared yields the frequency spectrum for this specific block and, consequently, for a certain time interval centred around a specific point in time. The spectra of each block are stitched leading to a spectrogram that reveals the points in time at which certain flagellar beating frequencies rise or vanish, see fig. 3.17. The following procedure is performed on a per cell basis for each flow condition, individually:

- ▷ The length of the entire sequence is typically $T = 1022$ ms and was recorded at a framerate of $f = 1$ kHz.
- ▷ Each block, or input signal, has a length of $l = 512$ ms.
- ▷ In order to pick up the temporal resolution of the input signal, blocks are shifted by 1 ms thus overlapping with the neighbouring block by $l - 1$.
- ▷ Since the frequency resolution of the Fourier transformation depends on the length of the input signal, the resolution was increased by zero-padding the input signal, here up to a total length of $L = 2^{14} = 16384$.
- ▷ The Gaussian window $w(n) = \exp(-j^2/2\sigma^2)$, with $j = 0 \dots l - 1$, is chosen such that the beginning and the end of the input signal is approximately zero

in order to not introduce artificial jumps between the end of the input signal and the beginning of the zero-padding. This requirement is fulfilled by using a standard deviation of $\sigma = 64$ ms in the case of a block size of $l = 512$ ms.

- ▷ Individual frequency spectra are obtained by individually Fourier-transforming each windowed and zero-padded block. The spectrogram is generated by stitching these individual spectra in the correct temporal order giving access to the temporal evolution of beating frequencies.
- ▷ By averaging the spectrogram in time, the most prominent frequencies as well as their corresponding peak widths can be reliably extracted, see fig. 3.17 (orange triangles).

3.2.2 Measurement protocol

Especially if imposing high flow velocities, the flagella are pushed very close or even underneath the cell body. Here, the previously developed tracking code fails to distinguish the flagella from the cell body and thus, parts of the flagella remain untracked. Since these experiments are meant to cover a large pressure range, 16 sequences as offered by the camera's *ring mode* are not enough, thus the camera is operated in *burst mode*. Here, the frame size of the image defines the number of recordable sequences each consisting of 1022 images.

Measurements are again performed in a circadian manner, see fig. 3.18: First, the desired pressure was set and *Chlamydomonas reinhardtii* were allowed to acclimatise

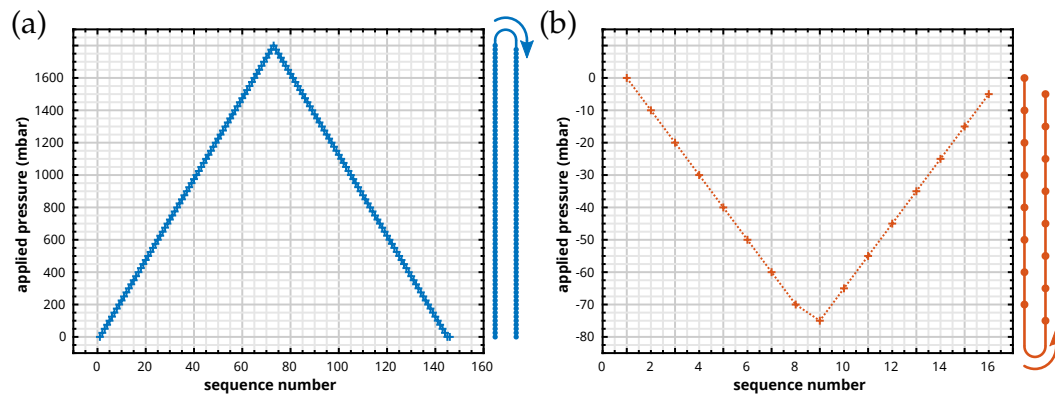


Fig. 3.18: Visualisation of the measurement protocols used for (a) positive stalling experiments and (b) negative stalling experiments. Negative stalling measurements consist of 16 individual sequences, i.e., 16 different applied pressures, while positive stalling measurements consist of 146 sequences of 73 different applied pressures. The identical pressure ramps are used for all microfluidic chips. Using their individual characteristic calibration curve (see fig. 2.10), applied pressures are translated to flow velocities.

for 10 s the applied flow velocity prior to image acquisition for ≈ 1 s at a framerate of 1 kHz. By setting the next pressure, the cycle continues. Using this protocol, 146 different pressures could be recorded until data had to be transferred from the camera to the PC. During the first 73 measurements, the pressure was increased from 0 mbar up to 1800 mbar in steps of 25 mbar immediately followed by decreasing the pressure in steps of 25 mbar during the next 73 sequences. Finally, *cis*- and *trans*-flagellum were differentiated using white light illumination. By means of these waiting times and recording times, the total measurement duration is roughly 30 min easily fulfilling the time constraint of one hour.

3.2.3 The change in beating frequency under load

On changes in external load, the eukaryotic flagellum of *C. reinhardtii* responds with changes in flagellar waveform and beating frequency. Albeit the flagellar waveform is difficult to quantify, especially in the case of chiral beating with its pronounced out-of-plane component, the beating frequency is relatively easy to determine. In fig. 3.19, exemplary results in the case of positive load, i.e., if the flow direction being opposed to the swimming direction of the cell, are shown.

On increasing positive load, the beating frequency depends linearly on the applied flow velocity, starting to flatten gradually at around 3 mm/s. Above 3 mm/s, we find plateaus in the relationship between flow velocity and beating frequency. The upper plateau, usually in the range of 40 Hz or 50 Hz, can be identified with tremor-like beating. The second plateau, usually around 28 Hz, can be related to chiral beating. In general, the flagellum switches dynamically between these two beating modes, see also fig. 3.17.(c), sometimes interrupted by reversible stalling of the flagellar beat. Above a flow velocity of 6–8 mm/s, the flagellar beat stalls.

On decreasing positive load, the flagellum reproducibly resumes normal beating. A more or less pronounced hysteresis between the flow velocity, at which the flagellum starts to stall, and the flow velocity, at which the flagellum leaves the stalling region again, can be observed. Usually, but not necessarily, does the flagellum respond to increasing or decreasing positive load similarly, i.e., if the flagellum, for example, shows chiral beating on increasing load, it most likely shows chiral beating on decreasing positive load as well. In the range below 3 mm/s, no difference between the frequency response on increasing and decreasing positive load is detectable.

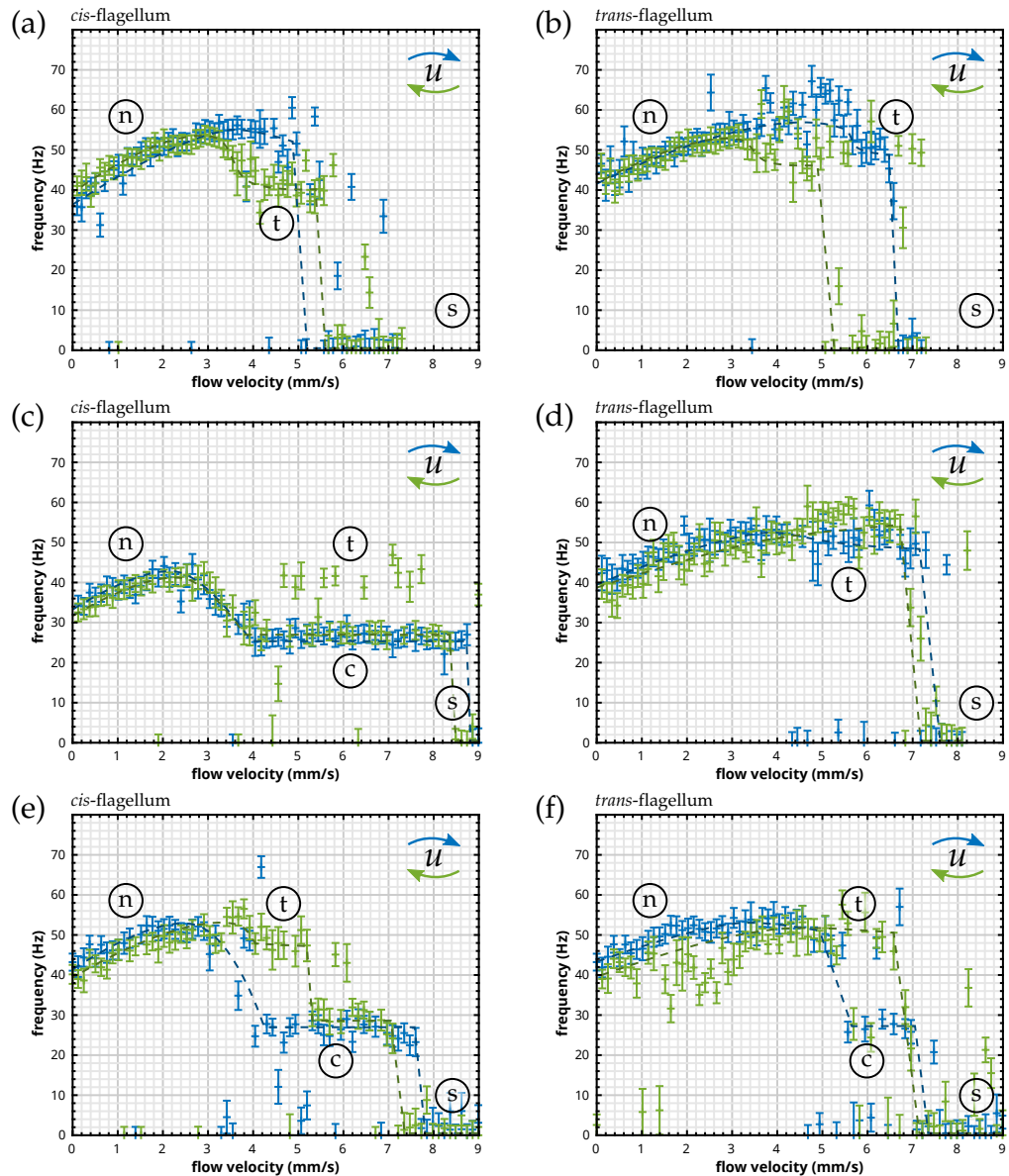


Fig. 3.19: On increasing positive load (blue), the beating frequency for both *cis*-flagellum (a, c, e) and *trans*-flagellum (b, d, f) increase almost linearly. In this region, labelled with (n), the flagellum is beating normally. In the region of intermediate flow velocity between 3 mm/s and 8 mm/s, the beating frequency remains constant on a high frequency level which we associate with tremor-like beating (labelled with (t)), drops to a lower level which we associate with chiral beating (labelled with (c)), switches dynamically between these two states, or is equal to zero which we associate with flagellar stalling (labelled with (s)). On further increasing the positive load, the flagellar beat stalls. On decreasing positive load (green), a more or less pronounced hysteresis in beating behaviour can be observed. Note that only the most prominent frequency in the spectrum per flow condition is shown for the sake of clarity. Dashed lines are only a guide to the eye. (a) shows the anomaly of a significant drop in beating frequency for tremor-like beating. (c) shows an extreme case of chiral beating over a wide range of flow velocities, occasionally interrupted by tremor-like beating, and (f) shows the rare case of a *trans*-flagellum performing chiral beating.

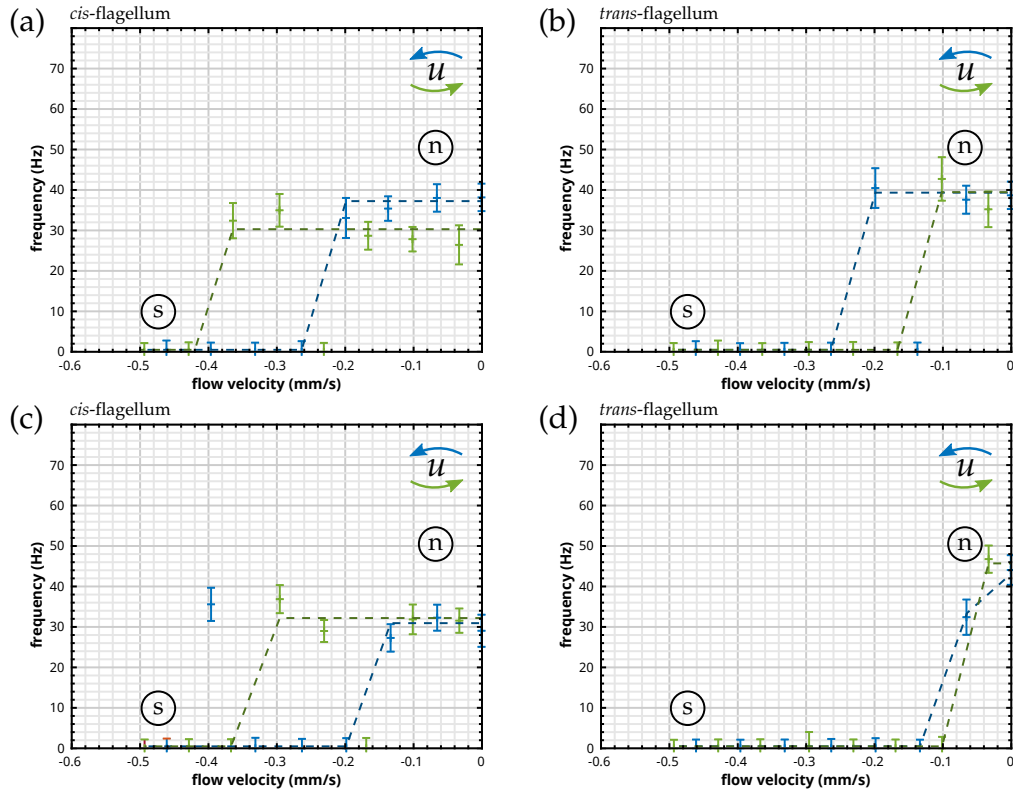


Fig. 3.20: On increasing negative load (blue), the beating frequency for both *cis*-flagellum (a, c) and *trans*-flagellum (b, d) remains almost constant. Starting from -0.1 mm/s, we find an instability region in which the flagella constantly switch between normal beating (labelled with n) and stalling (labelled with s). Around -0.4 mm/s and below, the flagellar beat of both *cis*- and *trans*-flagellum stalls. Note that this value is much lower compared to the case of positive load. Additionally, no significant different between *cis*- and *trans*-flagellum can be observed regarding the velocity at which the flagella start to stall. On decreasing negative load (green), the *cis*-flagellum leaves the stalling state at higher load than the *trans*-flagellum. Both on increasing and decreasing negative load, only normal beating and stalling can be observed. Note that only the most prominent frequency in the frequency spectrum is shown for the sake of clarity. Dashed lines are only a guide to the eye.

The stalling behaviour occurs under reversed flow conditions, termed negative load, too, see fig. 3.20. Yet, the velocity at which the flagellum remains in the stalling state is much smaller, usually around -0.4 mm/s. Between -0.1 mm/s and -0.4 mm/s, the flagellum switches dynamically between normal beating and stalling. Again, a hysteresis in stalling velocities but neither chiral beating nor tremor like beating could be observed under these conditions.

Comparing the experimental results with predictions based on the theoretical model by our collaborators, we find that the model can predict the principle frequency response, see fig. 3.21, yet the model cannot predict the existence of the

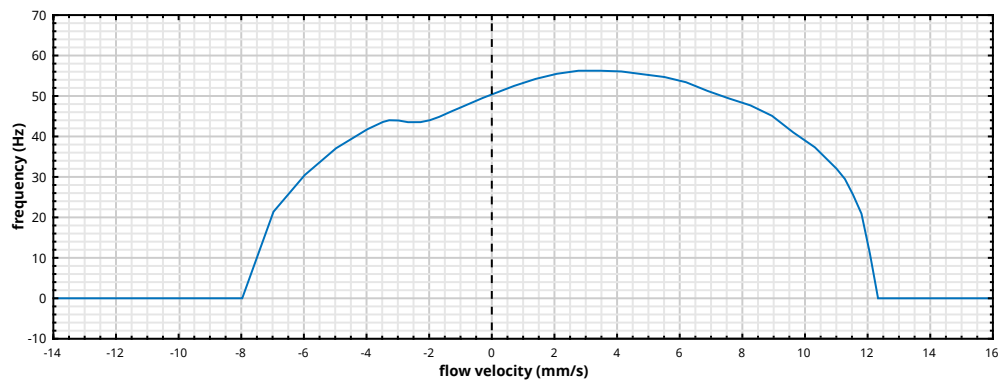


Fig. 3.21: Frequency response of the flagellum to externally applied load as predicted by the theoretical model. Underlying numerical data were provided by Gary S. Klindt.

frequency plateaus which we identified with chiral beating or tremor-like beating. The stalling phenomenon, which we observe in experiments above a certain load in both flow directions, is predicted by the model as well. Under positive load, the flagellum stalls above 12 mm/s in the model which is in good agreement with the experimental result ($\approx 5\text{--}9$ mm/s). Though under negative flow conditions, the model predicts flagellar stalling only below a flow velocity of -8 mm/s, significantly deviating from our experimental results (≈ 0.4 mm/s).

3.2.4 Phase diagram of the dynamic beating modes

The different beating modes of *C. reinhardtii*'s eukaryotic flagella occur more or less pronounced under different flow conditions, see fig. 3.22. In order to rule out a time dependence of the results, cells were measured at least twice, yet only the first ever measurement was used for evaluation while further measurements were used for viability confirmation only. Additionally, out of all performed measurements, only cells with reliable data for both *cis*- and *trans*-flagellum were considered. This means that only cells which enter and leave stalling during the recording were taken into account.

The phase diagram of beating modes is characteristic for the *cis*- and the *trans*-flagellum, respectively, and depends on whether the load is positive, negative, increasing, or decreasing. We find that starting at around 2–3 mm/s, both *cis*- and *trans*-flagellum stop beating normally. For the *cis*-flagellum, the response to increasing positive load, i.e., if the flow in the direction opposed to the swimming direction is gradually increased, is usually a transition from normal beating over dynamically switching between tremor-like beating and chiral beating to stalling.

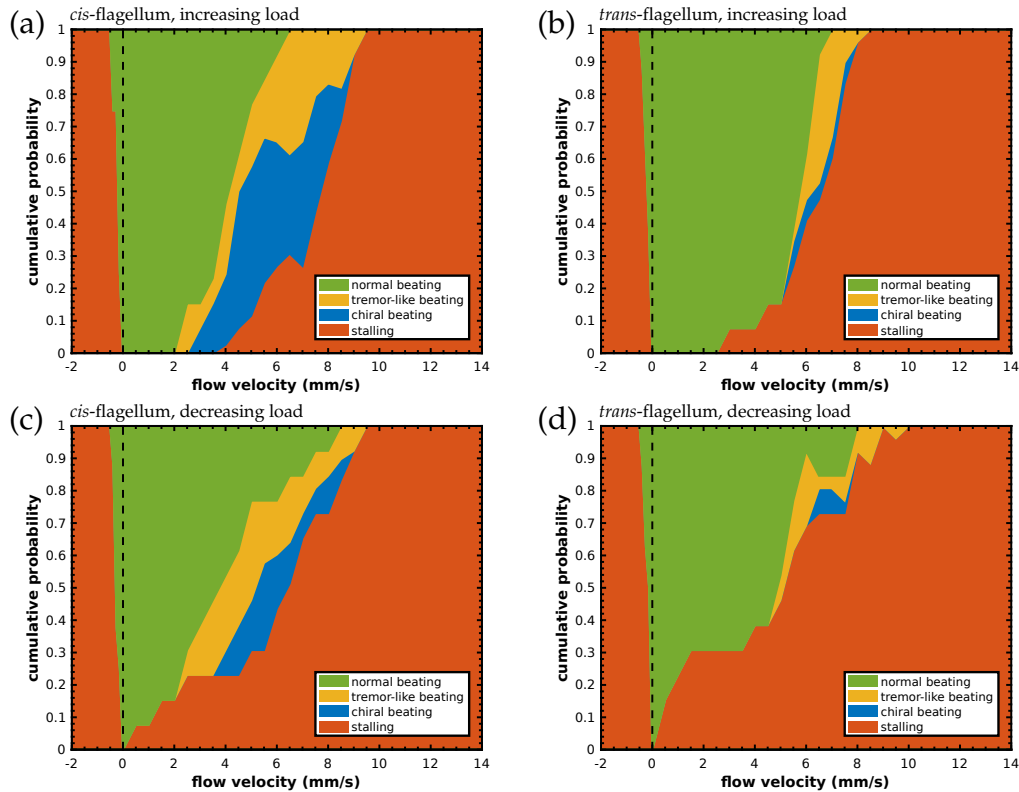


Fig. 3.22: Depending on the applied flow velocity, either normal flagellar beating (green), tremor-like beating (yellow), chiral beating (blue), or stalling (orange) can be observed. In total, $n^+ = 13$ cells for positive flow rates and $n^- = 8$ cells for negative flow rates were measured. (a) and (c) show the cumulative probability of finding normal, chiral, or tremor-like beating as well as stalling for the *cis*-flagellum, (b) and (d) for the *trans*-flagellum. (a–b) summarise measurements gradually increasing positive or negative load until the flagellum remains in the stalling state. (c–d) summarise measurements of gradually decreasing load starting in the stalling region. Above 10 mm/s and below -0.5 mm/s, both *cis*- and *trans*-flagellum show stalling exclusively. Tremor-like beating is in general more pronounced for the *cis*-flagellum than for the *trans*-flagellum, while chiral beating is almost exclusive to the *cis*-flagellum. In case of the *cis*-flagellum and on increasing positive load, both beating modes start to occur at a flow velocity of ≈ 2 mm/s. On decreasing load, tremor-like beating disappears again at flow velocities of ≈ 2 mm/s, while chiral beating already disappears at ≈ 4 mm/s. In case of the *trans*-flagellum, tremor-like beating occurs on increasing load and disappears again on decreasing load at a flow velocity of ≈ 5 mm/s. Neither tremor-like beating nor chiral beating can be observed under negative load conditions. On increasing positive load, the *trans*-flagellum stalls at lower load than the *cis*-flagellum. The occurrence of the different beating modes as well as the stalling region was determined via visual inspection of the recorded measurements.

Tremor-like beating is more pronounced for the *cis*-flagellum than for the *trans*-flagellum, and chiral beating is almost exclusive to the *cis*-flagellum. The number of *cis*- and *trans*-flagella that stalled in the different experimental runs almost linearly increases between 4 mm/s and 9 mm/s with all flagella stalling above a flow velocity of 9 mm/s. The *trans*-flagellum shows tremor-like beating only for a small velocity range and quickly stalls on further increasing positive load. The corresponding velocity at which the *trans*-flagella begin to stall is lower than for the *cis*-flagella, usually at around 2–3 mm/s. On decreasing positive load, both *cis*- and *trans*-flagellum remain in the stalling state for much lower flow velocities, i.e., the flagella show hysteresis. Again, the *cis*-flagellum transitions from the stalling state over dynamical switching between chiral beating and tremor-like beating back to normal beating, and the *trans*-flagellum changes directly from stalling to normal beating with tremor-like beating only during a small velocity range, if at all.

Both on increasing or decreasing negative load, *cis*- and *trans*-flagellum either beat normally or stall. Over a small velocity range, the flagella switch between these two states. Neither chiral beating nor tremor-like beating exist for negative load.

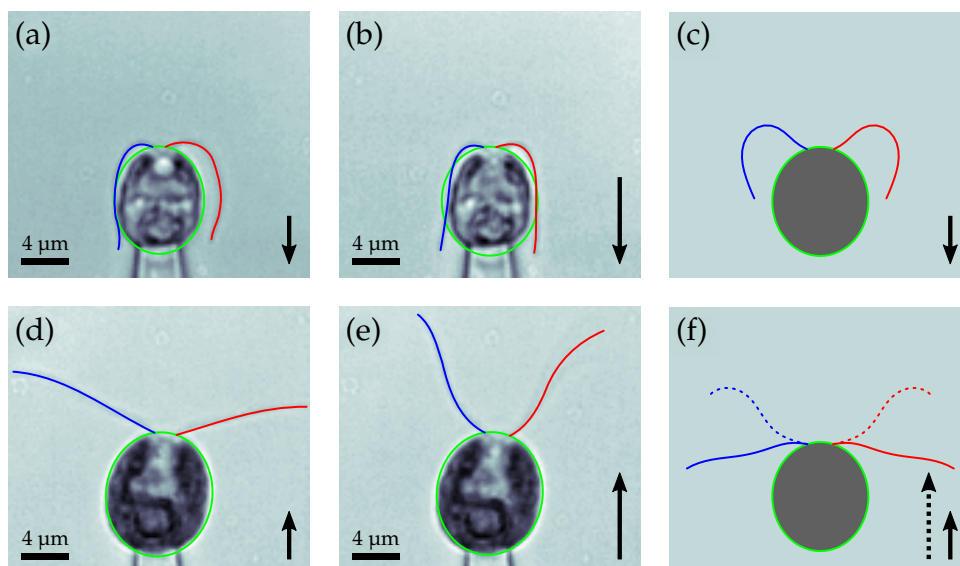


Fig. 3.23: In the case of high positive load (a–c), the flagellar beat is stuck right at the beginning of the recovery stroke, while under reversed flow conditions (c–e), the flagellum stalls right at the beginning of the power stroke. Initially, when the flagellum starts to stall, the flagellum keeps a certain shape due to still present motor activity (a, d), though being insufficient to keep up the beat. However, the flagellum does not remain stationary and is still able to slightly move back and forth. On increasing load, the motors stop working entirely (b, e). In the pictures show here, flow velocities u for (a), (b), (d), and (e) are 8.5 mm/s, 9.1 mm/s, -0.1 mm/s, and -0.5 mm/s, respectively. Simulations, provided by Gary S. Klindt, in the case of positive (c) and negative stalling (f), agree reasonably well with the experimental results. The arrows visualise both strength and direction of the flow.

3.2.5 Stalling behaviour of the flagellar beat under high load

Stalling of the flagellar beat simply means that the beat comes to a halt. Consequently, the beating frequency is zero. Under positive load, the flagellar beat is stuck right at the beginning of the recovery stroke (fig. 3.23.(a–c)) and in case of negative load, the flagellum is stuck right at the beginning of the power stroke (fig. 3.23.(d–f)). However, there is still some residual activity left leading to a very slow and hardly noticeable movement of the flagellum. In fact, two different kinds of stalling exist which we will refer to as initial stalling, see fig. 3.23.(a, d), and final stalling, see fig. 3.23.(b, e).

Initial stalling reflects the case that is also predicted by the theoretical model of our collaborators, see fig.3.23.(c, f). Here, the molecular motors within the flagellum are still active and maintain the flagellum in its current shape. In this state, and albeit the external load is not changed, the flagellum can, due to intraflagellar noise, revive flagellar beating, either directly in the case of negative load, or, in the case of positive load, switch to chiral beating or tremor-like beating, and go back to initial stalling again. On further increasing load, initial stalling transitions to final stalling. Here, the flagellum does not resist to the flow and it aligns with the cell body. This state is stable and as long as the external load is not reduced, the flagellum cannot resume to beat.

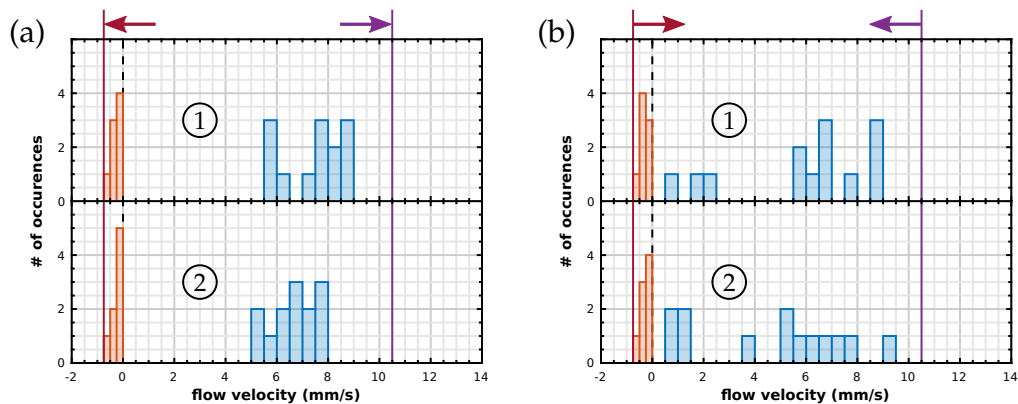


Fig. 3.24: (a) On increasing positive load (blue, $n^+ = 13$), stalling velocities range from 5 mm/s to 9 mm/s. The *trans*-flagellum (2) already stalls at lower velocities than the *cis*-flagellum (1). On increasing negative load (orange, $n^- = 8$), no systematic difference was observed, yet flagella already stalled at small negative flow velocities not being able to sustain a negative flow beyond -0.5 mm/s. (b) On decreasing positive load (blue), the distributions of velocities at which the *cis*-flagellum (1) and the *trans*-flagellum (2) leave the stalling state again are usually lower compared to the velocities at which they stall on increasing positive load. On decreasing negative load (orange), neither *cis*- nor *trans*-flagellum show a significant difference.

Cis- and trans-flagellum differ in stalling behaviour. In fig. 3.24, the velocity at which the flagellar stalling region begins is shown for *cis*- (1) and *trans*-flagellum (2). The stalling velocities under positive load range from 5 mm/s to 9 mm/s for both *cis*- and *trans*-flagellum. In the case of negative load, the stalling velocities are much smaller, only approximately -0.4 mm/s. This difference in stalling velocities between the *cis*- and the *trans*-flagellum, see fig. 3.25, reveals that the *cis*-flagellum can stand higher load than the *trans*-flagellum, yet it is much less pronounced in the case of increasing negative load. The difference for increasing positive load is up to $|u_{cis} - u_{trans}| = 3 \text{ mm/s}$, corresponding to 40–50% of the respective average velocity

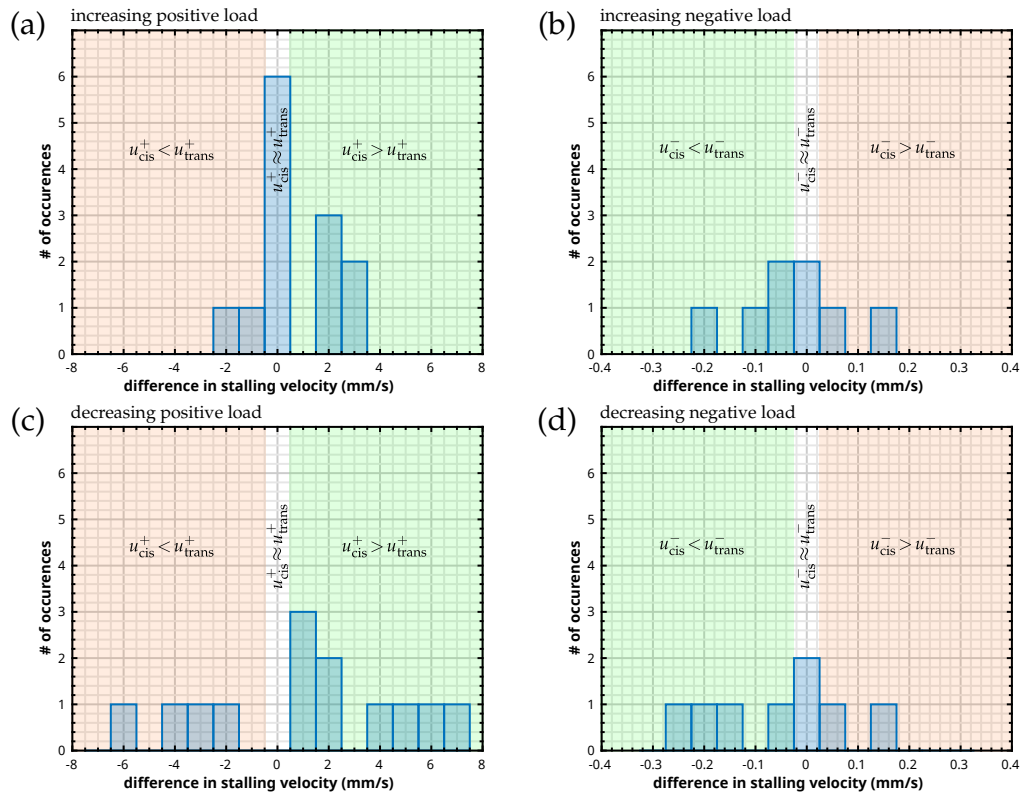


Fig. 3.25: In the case of positive load (a, c, $n^+ = 13$) as well as in the case of negative load (b, d, $n^- = 8$), the *cis*-flagellum performs at least as good as the *trans* flagellum, but usually much better: On increasing positive load (a), the velocity u_{cis}^+ at which the *cis*-flagellum starts to stall is significantly greater, up to 3 mm/s, or at least equal compared to the velocity u_{trans}^+ at which the *trans*-flagellum starts to stall. The case $u_{cis}^+ < u_{trans}^+$ is a rare event. On increasing negative load (b), $|\Delta u| = |u_{cis} - u_{trans}| \leq 0.2 \text{ mm/s}$ and thus much less than in (a). Again, the *cis*-flagellum can stand higher or at least equal load compared to the *trans*-flagellum, thus the case $u_{cis}^- < u_{trans}^-$ is more pronounced. On decreasing positive load (c), the *cis*-flagellum leaves the stalling state already at higher load. However, the difference $|\Delta u|$ is in general larger, up to 7 mm/s, and more distributed. In the case of decreasing negative load (d), $|\Delta u| < 0.3 \text{ mm/s}$. Yet, there is no significant difference compared to (b).

at which flagella start to stall, but only approximately $|u_{cis} - u_{trans}| = 0.2$ mm/s for increasing negative load. On decreasing positive load, the *cis*-flagellum leaves the stalling state again at higher load than the *trans*-flagellum. The difference at which the flagella leave the stalling state is much more pronounced than in the case of increasing positive load, up to $|u_{cis} - u_{trans}| = 7$ mm/s. However, on decreasing negative load, no significant difference compared to the case of increasing negative load can be observed.

Hysteresis of flagellar stalling. Both *cis*- and *trans*-flagellum show pronounced hysteresis in the case of positive and in the case of negative load, see fig. 3.26. For the *cis*-flagellum under positive load conditions, the difference between the stalling velocities for increasing and decreasing positive load is usually significantly positive, i.e., the velocity at which the flagellum enters the stalling region is higher than the velocity at which the flagellum leaves the stalling region again, up to 7 mm/s. Under negative load conditions, we still find hysteresis in stalling behaviour, yet we find no pronounced bias towards one direction, i.e., sometimes the flagellum stalls at a flow velocity which is lower than the velocity at which it leaves the stalling state again, sometimes it is the other way around.

A possible explanation for the hysteretic behaviour of the stalling velocities on external load is based on the existence of the two stalling states, see fig. 3.23: On increasing load, the flagellar beat transitions from normal beating over a multi-stable region, in which the flagellum dynamically switches under chiral beating, tremor-like beating, and stalling in the case of positive load, or between normal beating and stalling for negative load. However, this stalling of the flagellar beat is the initial stalling state in which the molecular motors are still able to maintain the flagellar shape. As long as the flagellum is in the initial stalling state, no hysteresis would be observable on decreasing load. And the theoretical model of our collaborators matches this situation.

Yet, on further increasing load, the stalling state changes from initial stalling to final stalling. Here, the molecular motors are not able to maintain the flagellar shape anymore. From our data, we cannot judge if the motors simply stop moving due to biochemical changes inside the cell, if they lose the connection to the neighbouring microtubules doublet so that they cannot bend the flagellum anymore, or if the force that the motors can apply is simply too low to bend the flagellum against the external load and its own stiffness. No matter the exact cause, the flagellum will not leave this state if the load is not reduced. Though, the flagellar beat will not restart at the flow velocity at which it stopped on increasing load, but for lower external load.

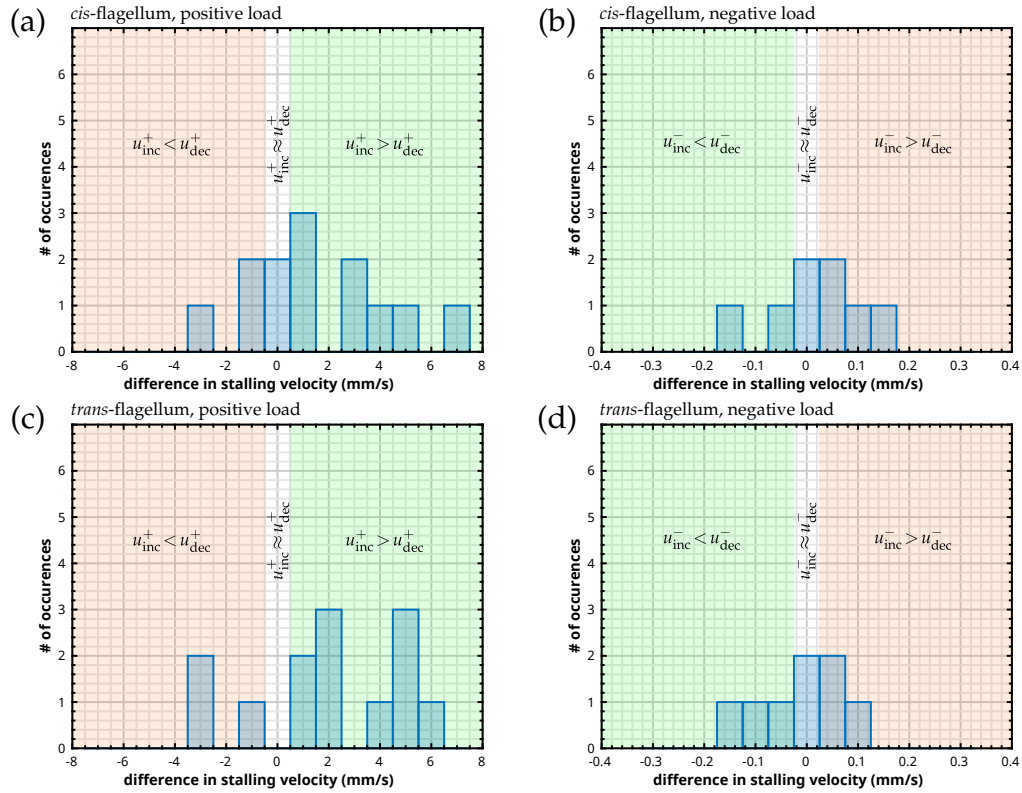


Fig. 3.26: Both in the case of the *cis*-flagellum (a, b) and the *trans*-flagellum (c, d), hysteresis can be observed both for positive load (a, c, $n^+ = 13$) and negative load (b, d, $n^- = 8$): In the case of positive load (a, c), the difference between the velocity at which the flagellum starts to stall on increasing positive load, u_{inc}^+ , and the velocity at which the flagellum starts to beat again on decreasing positive load, u_{dec}^+ , is usually positive with no significant difference between *cis*- (a) and *trans*-flagellum (c). Here, u_{inc}^+ is much larger than u_{dec}^+ , up to $\Delta u = u_{inc}^+ - u_{dec}^+ = 7$ mm/s. In the case of negative load (b, d), hysteresis is also present but not significantly biased towards u_{inc}^- or u_{dec}^- , neither for the *cis*- nor for the *trans*-flagellum and almost symmetrically distributed around $\Delta u = 0$ mm/s.

Considering a flagellum with all its internal structure, but without the molecular motors. If a certain load is applied, and since the flagellum is fixed at the basal body, its behaviour can be described by the Euler-Bernoulli beam theory: On increasing load, it gets deflected, and on decreasing load, it bends back to its original state. If we now identify the flagellum in the final stalling state with an already deflected beam, the shape of the flagellum will relax on decreasing load to a shape from which the flagellum can go back to initial stalling state, see fig. 3.27. From the initial stalling state, the flagellar beat can resume. This means that the flagellum has a specific region in which it can both actively bend as well as externally be bent. However, if the imposed bending exceeds this region, the molecular motors are unable to work anymore. The flagellum can neither beat

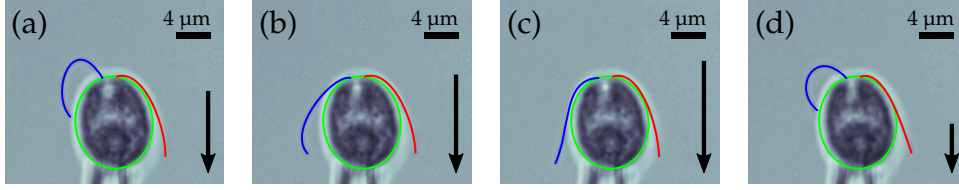


Fig. 3.27: On increasing load (a–c), the left flagellum (blue) transitions from initial stalling to the final stalling state, the right flagellum (red) is always in the final stalling state. On decreasing the load again (d)—in the exemplary case shown here down to a velocity lower than the velocity in (a)—the flagellum returns to the initial stalling state prior to resuming regular beating. The arrows visualise both strength and direction of the flow velocity.

nor maintain the initial stalling state. Yet, the root cause for the final stalling state remains unknown. We can only speculate that the overbending of the flagellum changes the flagellum’s curvature in such a way that the molecular motors detach from the microtubule. According to [115, 116], the regulation of the flagellar beat might indeed be curvature controlled.

3.3 Flagellar synchronisation

In order to swim in a straight manner, both flagella of *Chlamydomonas reinhardtii* have to beat in synchrony. The flagella beat by means of stochastic stepping of their dynein motors [53] which is attended by characteristic level of active noise. We can treat the system of two flagella as a system of two weakly coupled oscillators in the presence of noise:

$$\dot{\theta}_{cis} = \dot{\varphi}_0^{cis} + \frac{\kappa}{2} \sin(\theta_{trans} - \theta_{cis}) + \zeta_{cis}, \quad (3.20)$$

$$\dot{\theta}_{trans} = \dot{\varphi}_0^{trans} + \frac{\kappa}{2} \sin(\theta_{cis} - \theta_{trans}) + \zeta_{trans}. \quad (3.21)$$

With an intrinsic frequency mismatch of $\Delta\omega = \dot{\varphi}_0^{cis} - \dot{\varphi}_0^{trans}$, a phase lag of $\delta = \theta_{cis} - \theta_{trans}$, and $\zeta(t) = \zeta_{cis} - \zeta_{trans}$, we find the noisy Adler equation [97]

$$\dot{\delta} = \Delta\omega - \kappa \sin(\delta) + \zeta(t) \quad (3.22)$$

which models the dynamics of coupled flagella as the overdamped motion of a single particle that is diffusing in a tilted washboard potential [39, 48]:

$$U(\delta) = -\Delta\omega \cdot \delta - \kappa \cos(\delta). \quad (3.23)$$

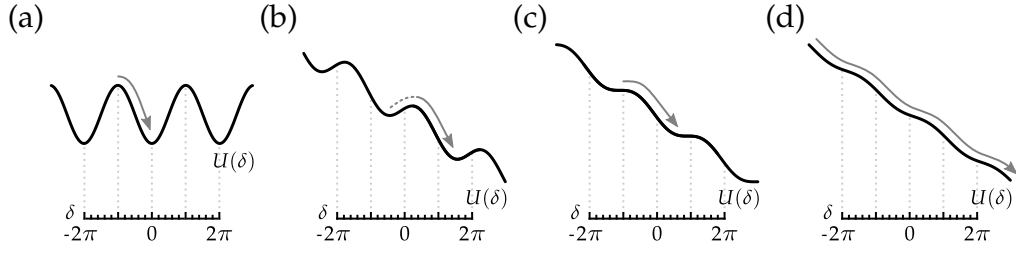


Fig. 3.28: Flagellar dynamics can be visualised as a particle in a washboard potential $U(\delta)$. (a) For $\Delta\omega = 0$, local maxima correspond to AP synchronisation (unstable fixed point at $\delta_{AP}^* = \pm(2n-1)\pi$, $n \in \mathbb{N}$) while local minima correspond to IP synchronisation (stable fixed point at $\delta_{IP}^* = \pm 2n\pi$, $n \in \mathbb{N}$) if $\kappa > 0$ and vice versa if $\kappa < 0$. The grey arrows indicate the direction of the phase slip. (b) In the case of $0 < |\Delta\omega| < |\kappa|$, noise is required for phase slips to happen, see dashed grey line. (c) For $\Delta\omega = \kappa$, there are no local minima or maxima, just unstable fixed points at $\delta_{AP}^* = \pm(2n-1)\pi$, $n \in \mathbb{N}$. (d) Finally, in the case of $|\Delta\omega| > |\kappa|$, there are no fixed points and flagellar synchronisation is impossible.

- ▷ In the case of vanishing frequency mismatch $\Delta\omega \approx 0$, see fig. 3.28.(a), and in the absence of noise, i.e., $\zeta(t) \approx 0$, we find stable fixed points at $\delta_{IP}^* = \pm 2n\pi$, $n \in \mathbb{N}$, and unstable fixed points at $\delta_{AP}^* = \pm(2n-1)\pi$, $n \in \mathbb{N}$, if $\kappa > 0$, i.e., this scenario describes a phase slip event from anti-phase synchronisation (AP) to in-phase synchronisation (IP). Consequently, for $\kappa < 0$, stable and unstable fixed points change places and this scenario describes a phase slip event from IP to AP.
- ▷ If $0 < |\Delta\omega| < |\kappa|$, we find both stable and unstable fixed points, see fig. 3.28.(b). Without noise, the flagella are trapped in local minima at $\delta^* = \text{asin}(\Delta\omega/\kappa)$, carrying the signature of the intrinsic frequency difference between *cis*- and *trans*-flagellum. However, if we allow for active noise in the system, phase slips are possible [39].
- ▷ If the synchronisation strength κ matches the frequency mismatch $\Delta\omega$, i.e., $\Delta\omega = \kappa$, see fig. 3.28.(c), and noise is still negligible, we find only unstable fixed points at $\delta_{AP}^* = \pm(2n-1)\pi$, $n \in \mathbb{N}$.
- ▷ In the case of $|\Delta\omega| > |\kappa|$, we find no more fixed points at all, see fig. 3.28.(d). Here, the flagella are beating almost independently of each other.

In short, we can think of flagellar dynamics as a particle moving in a constantly fluctuating potential landscape. Former stable fixed points turn into unstable fixed points if the coupling constant κ changes sign. The noise level $\zeta(t)$ in the system determines at which frequency difference phase slips can occur in the case of $0 < |\Delta\omega| < |\kappa|$: the larger the frequency difference, the less noise is required for a phase slip to happen. If the coupling constant κ matches the frequency difference $\Delta\omega$, we find unstable fixed points at $\delta_{AP}^* = \pm(2n-1)\pi$, $n \in \mathbb{N}$, but no stable fixed

points at all. Finally, if the frequency difference exceeds the coupling constant, we find no fixed points at all and flagellar synchronisation cannot be achieved.

Phase slip dynamics. In general, periods of flagellar synchrony are interrupted by phase slip events. These phase slips are characterised by one flagellum performing extra beats, see fig. 3.29.(a) and, usually, one flagellum dominates over the other. In the standard laboratory strains of *C. reinhardtii*, namely CC-124 and CC-125, periods of IP synchronisation of the flagella are interrupted by periods of AP synchronisation. The transition event from IP to AP, or vice versa, can be analytically described by solving eq. 3.22 in the case of vanishing frequency mismatch $\Delta\omega \approx 0$, see fig. 3.28.(a), and in the absence of noise, i.e., $\zeta(t) \approx 0$, leading to

$$\delta = 2 \cdot \text{atan}(\exp(-\kappa(t - t_i))). \quad (3.24)$$

For $\kappa > 0$, δ describes a phase slip event from AP to IP synchronisation, while for $\kappa < 0$, it describes the transition from IP to AP synchronisation.

We observe that the *Chlamydomonas reinhardtii* strain we used in our studies (SAG 11-32c mt-) shows almost no anti-phase synchronisation, thus we almost exclusively see phase slips of $\pm 2n\pi$, $n \in \mathbb{N}$. However, we can still find an analytic solution of eq. 3.22 for these slip events if we assume that the synchronisation strength κ matches the frequency mismatch $\Delta\omega$, i.e., $\Delta\omega = \kappa$, see fig. 3.28.(c). If noise is negligible, we find:

$$\delta = 2 \cdot \text{atan}(\kappa(t - t_i)) - \pi. \quad (3.25)$$

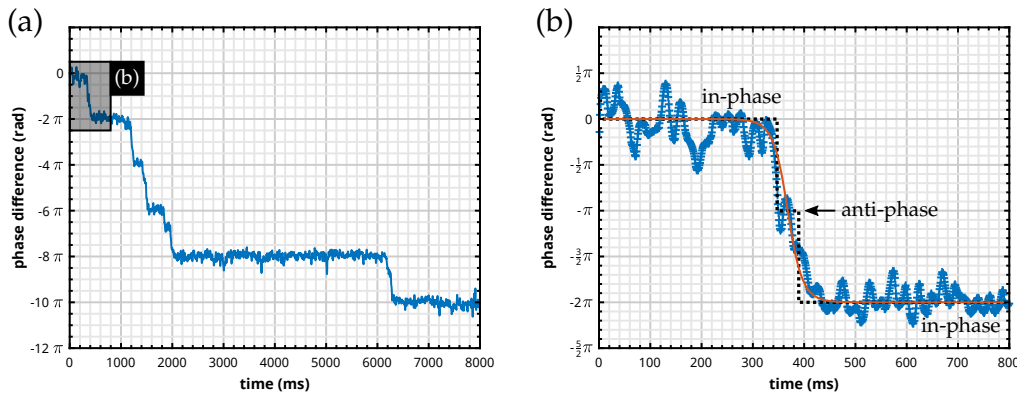


Fig. 3.29: Phase difference as a function of time. Usually, one flagellum dominates over the other, i.e., the phase difference steps up or down, but mostly in the same direction. By rounding to the closest multiple of π , we find plateaus of in-phase synchronisation and periods of unknown synchronisation state. During the latter, the flagella are either in the middle of a phase slip event, or AP synchronised, which is unlikely for the *C. reinhardtii* strain we used.

Theoretically, fitting eq. 3.25 to each slip event would result in good quality measures for the flagellar coupling κ as well as the intrinsic frequency difference $\Delta\omega$. Yet, as it can be seen in the representative example shown in fig. 3.29.(a), one flagellum of the *Chlamydomonas reinhardtii* strain we used typically performs more than just one extra beat, i.e., $|\delta| \geq 2\pi$.

Since we ignore noise to find analytic solutions which we can fit to experimental data, we are restricted to the rare phase slip events of $\pm 2\pi$ so statistics is very poor. Therefore, we use a more phenomenological way to quantify flagellar synchrony: As shown on fig. 3.29.(b), we simply round phase differences to the closest multiple of π and count periods of in-phase synchronisation that are defined by a phase difference of $\delta_{IP}^* = \pm 2n\pi$, $n \in \mathbb{N}$. We identify a high ratio of IP synchronisation periods with a relatively large coupling constant compared to the noise level, and a low ratio with weak coupling compared to noise, yet we do not know if the noise level rises or the coupling constant drops.

Load-dependent flagellar coupling. Depending on the applied load, we find a behaviour similar to the frequency response of individual flagella, see fig. 3.30.(a): With increasing negative load, the amount of in-phase synchronisation and thus the

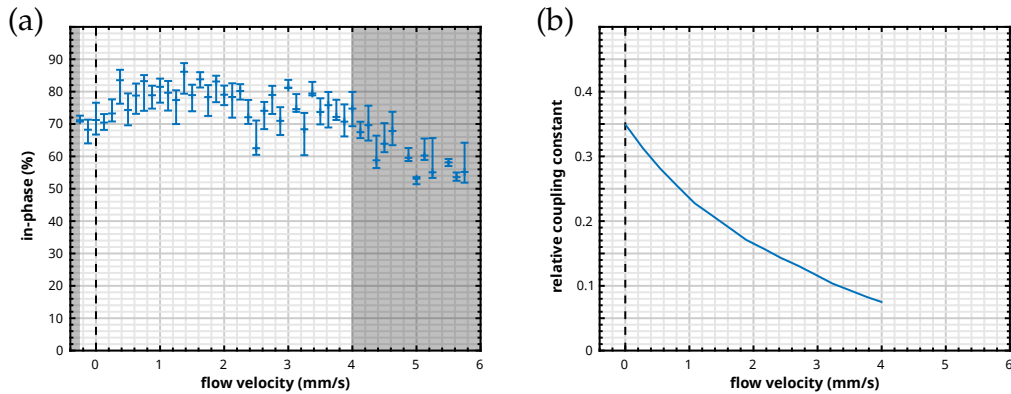


Fig. 3.30: (a) With increasing positive load, i.e., the load that is applied opposed to the swimming direction, the synchronisation first slightly increases, followed by a gradual decrease. On increasing negative load, i.e., if the cell is swimming with the flow, the synchronisation gradually decreases. Black shaded regions are less trustworthy since here, less data is available because flagellar beating differs from normal beating, i.e., different dynamic modes of beating and stalling can be observed. In total, $n^+ = 13$ cells for positive flow rates and $n^- = 8$ cells for negative flow rates were measured. (b) In contrast, we do not find the initial increase in beating frequency in the simulations. The relative coupling constant, which is the quotient of the coupling constant κ and the beating frequency f_0 in the absence of external load, decreases with increasing load. Underlying numerical data were provided by Gary S. Klindt.

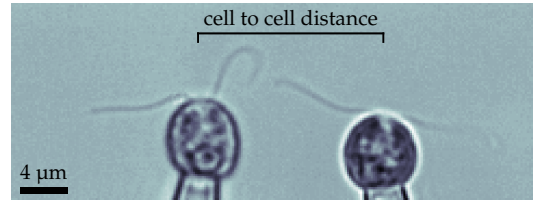


Fig. 3.31: Two *Chlamydomonas reinhardtii* cells swimming next to each other, held at a distance by means of micropipettes.

coupling strength decreases, while it increases with increasing positive load. However, on further increasing positive load, the amount of in-phase synchronisation first saturates and finally drops. A decrease of coupling strength is expected for increasing load, no matter which direction, since perturbations of one flagellum are simply swept away by the external flow. Yet, it remains unclear why a moderate increase in positive load leads to an increase of coupling strength—an effect that we do not observe in simulations, see fig. 3.30.(b).

Flagellar synchronisation of nearby swimming cells. Going one step further, we placed two *C. reinhardtii* cells next to each other, oriented in such a way that they swim in the same direction, see fig. 3.31. In this scenario, flagella belonging to the same cell are connected at their base via distal striated fibres and at the same time part of the chemical signalling system which might also interact with the flagella. Additionally, these flagella are hydrodynamically coupled as well. Flagella of different cells can only interact by means of hydrodynamic interactions. By varying the distance between both cells, we can probe the general interaction strength and test which one is more dominant for flagellar synchronisation: intracellular coupling or hydrodynamic interactions.

Assuming weak noise ζ_i in this system of nearly identical limit cycle oscillators with individual phases θ_i , we can use the Kuramoto model [1, 70] to describe the phase relation of the flagella:

$$\dot{\theta}_i = \dot{\phi}_0^i + \zeta_i(t) + \frac{\kappa}{N} \sum_{j=1}^N \sin(\theta_j(t) - \theta_i(t)). \quad (3.26)$$

In this model, all N flagella are beating with their own intrinsic frequency $\dot{\phi}_0^i$ and are furthermore considered to be equally coupled to all other flagella via the coupling constant κ . Only if the coupling constant κ is strong enough, we are able to find a fully synchronised state in which all flagella phase-lock and beat with identical frequency.

In the limit of $N \rightarrow \infty$, the entirely nonlinear Kuramoto model can be solved analytically by defining a complex order parameter $r \cdot e^{i\psi}$ as the ensemble average

of the oscillator phases θ_i on the unit cycle in \mathbb{C}^1 :

$$\frac{1}{N} \sum_{j=1}^N e^{i\theta_j} = r \cdot e^{i\psi}. \quad (3.27)$$

This order parameter represents a so called mean field with the average oscillator phase ψ and the average amplitude r . Note that in this context, there is no temporal averaging, i.e., the mean field is not necessarily stable in time and can fluctuate. Multiplying eq. 3.27 with $e^{-i\theta_i}$ and only considering the imaginary part, we find

$$\frac{1}{N} \sum_{j=1}^N e^{i(\theta_j - \theta_i)} = r \cdot \sin(\psi - \theta_i). \quad (3.28)$$

Inserting this identity in eq. 3.26 leads to

$$\dot{\theta}_i = \dot{\varphi}_0^i + \zeta_i(t) + \kappa \cdot r \cdot \sin(\psi - \theta_i). \quad (3.29)$$

In this representation, the individual oscillators are no longer coupled and the order parameter r and ψ govern the behaviour of the system. Especially the amplitude r can be used to measure the level of synchronisation which is why this quantity is also known as the order parameter for phase coherence. For $r = 1$, all oscillators are moving in-phase all the time and share a common frequency. If $r = 0$, we see no phase-locking at all, consequently leading to permanent phase drifts. In the case $0 < r < 1$, partial phase-locking can be observed.

Calculating the time averaged phase coherence as a function of the distance d between both cells, $r(d) = \langle r \rangle_t$, we are able to quantify flagellar synchronisation at a certain inter-cellular distance. If we take all $N = 4$ flagella of both cells into account and average over all $n = 6$ measured cell pairs, we find

$$\langle r(d) \rangle_{N=4} = \underset{\text{(mean)}}{0.5} \pm \underset{\text{(s.e.)}}{0.1}, \quad (3.30)$$

i.e., partial phase-locking. In order to investigate synchronisation in more detail, we used, although theoretically not directly applicable, the Kuramoto model to determine the phase coherence of individual flagella pairs, see fig. 3.32.

In general, we find that a flagella pair which belongs to one cell shows stronger phase coherence ($r \approx 0.7$ – 0.8) than a flagella pair of different cells ($r \approx 0.6$). These values are far away from the totally random state of $r = 0$, suggesting that there is some kind of phase-locking of the individual flagella. Long-range hydrodynamic interactions might be responsible for this synchronisation, yet recent experimental studies show that hydrodynamic interactions are much weaker than intracellular coupling [103]. For a flagellar pair belonging to one cell, both intracellular coupling and hydrodynamic interactions contribute to the phase coherence. If the flagella

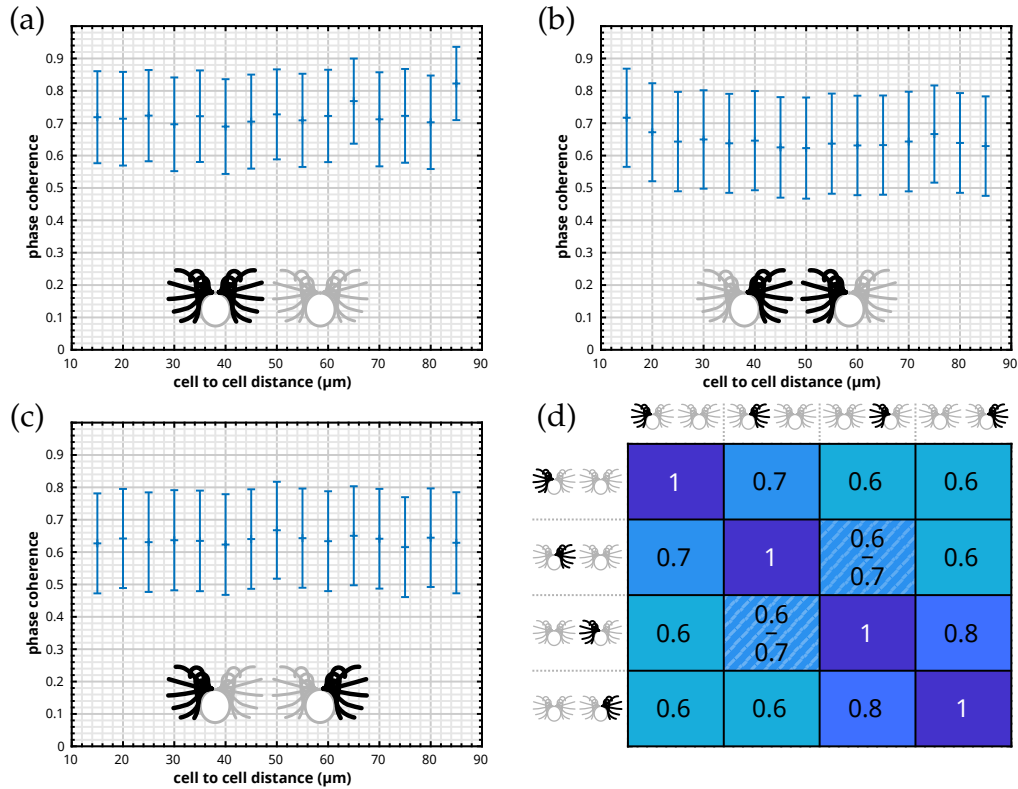


Fig. 3.32: Time averaged phase coherence $r(d)$ as a function of the cell to cell distance in the case of a flagella pair belonging to the same cell (a), of two neighbouring flagella which belong to different cells (b), and an exemplary representation for any other cell pair (c), here the case of two flagella on opposite sides of different cells. Error bars are large due to statistics of only $n = 6$ cell pairs. An overview of the time averaged phase coherence $r(d)$, additionally averaged over all $n = 6$ cell pairs and all distances d , is shown in (d) for each flagella pair, individually. Each value, except the diagonal elements, has a standard error of ≈ 0.1 . In general, the degree of phase coherence is higher if the considered flagella pair belongs to the same cell. Shaded values correspond to a neighbouring flagella pair which belongs to different cells—the sole distance-dependent values.

do not belong to the same cell, they are solely hydrodynamically coupled. In this case, we usually observe no distance dependence and the phase coherence remains constant at ≈ 0.6 . Additionally, we find the same value for large distances between the right flagellum of the left cell and the left flagellum of the right cell. Yet, the phase coherence of this particular flagellar pair depends on the inter-flagellar distance: On approaching each other, the phase coherence does not change over a wide range. However, at an inter-flagellar distance that is comparable to the average distance of a flagellar pair which belongs to the same cell, the phase coherence is in the order of 0.7 to 0.8 in both cases. Therefore, we can draw the conclusion that no matter if the flagella belong to the same cell or to different cells, as long as their

distance is the same, the phase coherence is identical. This result, which is a strong hint that hydrodynamic interactions are indeed important for synchronisation, is in line with previous experimental studies [21] but contradicts the experimental findings of [103].

3.4 Discussion

The eukaryotic flagellum is a remarkable machine. Due to the coordination of thousands of molecular motors inside the axoneme, flagella can beat at frequencies of tens of Hertz, propelling microswimmers with velocities in the range of up to $100\ \mu\text{m/s}$. Thereby, the beating flagellum exerts mechanical work by means of hydrodynamic forces on the surrounding fluid. Since the flagellum can interact with the fluid, the fluid motion can feed back the same way on the flagellum. Previous experiments revealed that hydrodynamic forces acting on the flagellum indeed affect the motor dynamics, altering the shape of the flagellar beat [131]. This interaction between external forces and the response of the flagellum to them is the foundation for synchronisation due to mechanical coupling [21, 33, 125]. Theoretical studies using minimal models representing beating flagella as spheres orbiting in circles showed that flagellar synchronisation is not solely depending on this load response but also on non-isochrony of the flagellar oscillations as well as phase-dependent, active driving forces and amplitude compliance [34, 88, 126, 128].

In recent years, *Chlamydomonas reinhardtii* has become the workhorse for synchronisation studies [36, 39, 73, 103, 108]. With its two flagella and the availability of mutants with a variety of genetic defects, *C. reinhardtii* is perfectly suitable for investigating flagellar synchronisation on a single cell level. In this work, we developed a custom micropipettes and microfluidics setup which enabled us to hold a single *Chlamydomonas reinhardtii* cell in the centre of a microfluidic chamber in order to expose it to homogeneous fluid flows. By means of high-speed video microscopy, combined with custom tracking routines, we were able to extract flagellar shapes, and thus the dynamic load response of *C. reinhardtii*'s flagella, with high temporal and spatial resolution.

High-precision flagellar tracking is required. In close collaboration with Gary S. Klindt and Benjamin M. Friedrich from the Max Planck Institute for the physics of complex systems in Dresden, we developed a tracking algorithm by which flagella are represented as sequences of tangent angles [105] with respect to the orientation of the cell, sorted by their position on the flagellum, and starting at the basal body. By applying a dimension reduction algorithm [133], these flagellar shapes are projected onto two dimensions. Based on this representation, we can reconstruct a

limit cycle [78, 133] which enabled us to obtain both phase and amplitude of a limit cycle oscillator [36, 39, 131]. By defining both amplitude and phase susceptibilities, we are able to quantify the response of the flagellar beat to external load.

A more realistic model for flagellar beating. Based on this analysis, our collaborators developed an effective theoretical model which is calibrated by our experimental data. We think that, compared to previously developed, idealised models [34, 88, 128, 129], this theoretical description is more realistic. Predictions of their model on synchronisation and phase-locking capabilities of the flagellar beat to an oscillatory flow are in good agreement with experimental results [103], verifying the legitimacy of this approach, in which flagellar dynamics are also represented as a limit cycle oscillator. Furthermore, hydrodynamic friction forces, which were computed using tracked flagellar shapes, are balanced by active flagellar driving forces. These active forces, which take intraflagellar friction into account, are per se unknown, yet only assumptions on their contribution can be made. Here, it is assumed that the efficiency of chemo-mechanical energy conversion, i.e., the efficiency of the flagellar beat, links hydrodynamic friction forces to active driving forces. The latter can be calibrated by means of our experimentally determined amplitude and phase speed data that were obtained in the absence of flow. Amplitude compliance is guaranteed by means of an amplitude spring. It is furthermore assumed that perturbations of the flagellar limit cycle are small which is true for low flow speeds. Additionally, active flagellar driving forces do not depend on the externally applied forces. This assumption is consistent with recent experiments performed on a single flagellar level [28]: Neither the beating frequency nor the external load have an influence on the ATP consumption of the flagellum, i.e., an increase in load leads to a decrease of the beating frequency and not to an increased ATP consumption. Indeed, we find that with increasing positive load, i.e., if the swimming direction of the cell is opposed to the flow direction, the phase speed during the recovery stroke is reduced compared to the case of no external load. However, both in the theoretical model, which was calibrated by our experimental data, and in our experiments, the power stroke speeds up more on increasing positive load than the recovery stroke slows down, leading to an increased beating frequency.

The load response is phase-dependent. Taking a closer look at the phase speed susceptibility and the amplitude susceptibility which are defined as the response of phase speed and amplitude, respectively, to external load as a function of the flagellar phase, we find a strong phase-dependence. These susceptibilities are a prerequisite for hydrodynamic synchronisation, i.e., vanishing susceptibility would lead to no entrainment to external mechanical, flow induced forcing. By comparing

experimental results with theoretical predictions of the calibrated model, we can determine the previously unknown mechano-chemical efficiency to $\eta = 0.21$. This means either that the conversion from chemical energy to mechanical work is very inefficient due to the internal structure of the flagellum impeding the molecular motors, or that only a small fraction of the ≈ 30000 molecular motors in the axoneme [87] use one ATP molecule per beat.

Load direction and strength dictate beating frequency and stalling. We find a similar dependence of the beat frequency on the applied flow velocity, even beyond the flow range in which the assumptions apply. For positive load, the beating frequency increases linearly with the flow velocity both in model based simulations as well as in experiments. Additionally, theoretically predicted velocities at which flagellar oscillations come to a halt are in good quantitative agreement with our experimental results. In the case of negative load, i.e., if the flow direction accords with the swimming direction, theory predicts a stalling velocity of comparable magnitude to the case of positive load. However, in our experiments, we observed flagellar stalling at negative load which is by a factor of more than 10 smaller. In any case, stalling is totally reversible, i.e., as long as the cell is not dead, it will always recover from stalling. Even beyond the stalling velocity, we find some residual activity in the flagellum observable as slight but sporadic movements of the flagellum. This remaining motion is a clear indication for a fluctuating noise level within the axoneme.

Hysteresis in flagellar stalling due to different stalling states. We observe a pronounced hysteresis in the flagellar response to increasing and decreasing load: In general, the velocity at which the flagellum enters the stalling state is different from the velocity at which the flagellum leaves the stalling state again. Usually, the velocity necessary to enter stalling is higher than the velocity of leaving stalling again. Although the *cis*-flagellum responds to external loads already at low values, usually it can stand higher load than the *trans*-flagellum before stalling occurs. In experiments, we observe two different stalling states: initial stalling and final stalling. In the initial stalling state, the flagellar oscillation seems to freeze at the transition point from power stroke to recovery stroke (in the case of positive load) or at the transition point from recovery stroke to power stroke (in the case of negative load). These stalling shapes are indistinguishable from still images taken at exact these flagellar phases. On further increasing load, we enter the final stalling state, when the flagella do not retain their shape anymore and align with the flow direction, and the transition from initial stalling to final stalling can be compared to a puppet who got its strings cut. The existence of these two stalling states might be an explanation for the hysteresis in the system and a hint towards

curvature based motor control [116]: During initial stalling, when the molecular motors are still able to maintain the flagellar shape, the flagellum can recover from the stalling state easily. However, in the final stalling state, the flagella are bent beyond their natural range of action, i.e., the flagella are now in a state where local curvature is beyond the range which is accessible during normal beating. Consequently, flagellar activity rapidly breaks down. In order to be able to resume regular beating, the load on the flagellum has to be reduced so that the flagella can relax from the unnatural bending. As soon as the flagella are back in their natural range of action, flagellar oscillations restart. Yet, we cannot definitely rule out that biochemical changes inside the flagellum, a lost connection to the neighbouring microtubules of molecular motors, or a reduced motor activity also play a role.

Previously unknown flagellar beating modes emerge under load. For intermediate positive load, we observed two previously unknown flagellar beating modes: chiral beating and tremor-like beating. Tremor-like beating can be thought of as incomplete flagellar beats during which the flagellum does not manage to perform a full transition from recovery stroke to power stroke, i.e., when the flagella reach out to begin with the power stroke, they are quickly pushed to the rear end of the cell. Mostly, this beat pattern is accompanied by the proximal part of the flagellum not showing any bending activity any more and the flagellum remains in a slightly curved shape. This beating mode is associated with a beating frequency which is in the order of the beating frequency in the absence of flow and independent of the applied positive load. For both *cis*- and *trans*-flagellum, tremor-like beating is equally present. Chiral beating is fundamentally different from all previously known beating patterns. It has a pronounced out-of-plane component, i.e., the flagellum leaves the beating plane in a regular manner. The corresponding beating frequency of this mode is independent of the applied flow velocity, too, but in the order of half the beating frequency under no external flow. We find that chiral beating is almost exclusive to the *cis*-flagellum. Neither chiral beating nor tremor-like beating could be observed in experiments under negative load conditions or in general in theoretical predictions.

External load influences flagellar synchronisation. Over the entire flow range in which flagella are beating regularly, we determined the phase coherence of the flagella pair of a single *C. reinhardtii* cell. In the regime of low flow speeds, we find that the synchronisation strength decreases linearly with increasing negative load and increases linearly with increasing positive load. On further increasing positive load, the synchronisation strength saturates and finally decreases again. While a decrease of synchronisation strength with increasing load is expected [66], the initial increase on positive load is at first totally unexpected. We can

only speculate that due to micropipettes fixation and the accompanying stress on the cell body, displacement of cell organelles might also influence the flagellar bases whose properties are known to be important for flagellar synchronisation [54, 66, 81, 111–113, 138].

Hydrodynamic interactions dominate over intracellular coupling. In a system of two *Chlamydomonas reinhardtii* cells, we find similar values in phase coherence for similar values of inter-flagellar distance, no matter if the flagella belong to the same cell or not, suggesting that hydrodynamic interactions play a more important role for flagellar synchronisation than intracellular coupling by means of basal bodies and distal striated fibres [21]. However, currently, the deviations in our data are relatively large, which is why more refined measurements, also with different mutants of *C. reinhardtii* and somatic *Volvox* cells, and additional statistics are mandatory in order to finally conclude on the roots of flagellar synchronisation.

Conclusion. So far, theories on flagellar beating, an active process which is powered by the collective dynamics of thousands of molecular motors, are mostly based on simple toy models which provide quantitative but often not qualitative descriptions. We envision that our results—phase-dependent flagellar load response, emergence of previously unknown beating modes, the characterisation of flagellar stalling, hysteresic behaviour on load changes, and the general asymmetry regarding the flow direction—may help to gain more knowledge on flagellar beating itself, leading to refined theories of the dynamics of molecular motors inside the flagellum [12, 24, 74, 105, 116].

4

Outlook

Albeit our joint project led to some new insights in the dynamics of flagellar beating and its synchronisation mechanism, we are not yet at the end of the road. So far, we only gradually applied a hydrodynamic load on the flagella, yet it might be interesting to investigate dynamic responses to the application of sudden external load as well, mimicing the collisions of a cell with an obstacle or another cell. Furthermore, the extended theoretical model [66], developed by our collaborators should be tested against different experimental conditions, e.g., changing the hydrodynamic interactions or manipulating basal body coupling. Especially, answering the question of how the basal body influences the synchronisation is challenging from an experimental point. In the following, suggestions for possible future experiments and enhancements are made.

Dynamic response of the flagellar beat to sudden load. In the measurements presented in this work so far, the cell was always allowed to acclimatise to the new environmental conditions, i.e., to the applied load. However, in nature, sudden events are more likely. The flagellar response to a sudden change in external load might reveal new insights in the characteristics of the molecular motors. Fig. 4.1 shows exemplary results of first experiments in which the external load was suddenly increased from zero flow to a flow speed at which the flagellar beat stalls, and vice versa. It has to be noted that the flow velocity cannot be changed instantaneously because it simply takes some time for the new flow profile to develop on changing the pressure drop at the microfluidics chip. Thus, the flow velocity changes gradually in less than two seconds from no load to high load, and within four seconds from high load back to zero load.

On suddenly increasing load, the beating frequency first increases rapidly, then quickly drops to zero, and the flagellar beat stalls. However, the response of the flagellum to this sudden increase seems to be delayed. On decreasing the external load, this delay is even more pronounced. Furthermore, the beating frequency quickly increases to the natural beating frequency of the flagellum but does not rise above it. Out of this preliminary measurement data, it is not possible to judge whether it is a temporal effect, i.e., that the flagellum simple needs some time to adapt to the new conditions, or if it is simply a hydrodynamic effect that is hidden by experimental deficiency: Partially, the delay might be due to a delay in triggering which is why the synchronisation between the high-speed camera

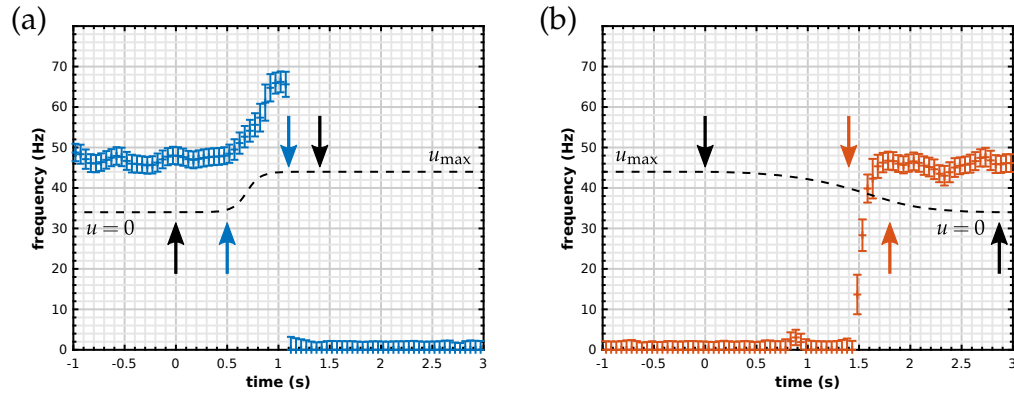


Fig. 4.1: (a) The response in beating frequency (mean \pm s.e.) of the the eukaryotic flagellum on a sudden increase in external load, and (b) the response to suddenly decreasing load. The black arrows indicate the start and the end of the change in flow velocity, and the coloured arrows indicate the start and the end of the frequency response of the flagellum, respectively. On increasing load, the beating frequency rises first, then rapidly drops to zero. On decreasing load, the beating frequency quickly rises from zero to the natural beating frequency of the flagellum. In both cases, the response is more or less delayed. Note that the transition time from high load to zero load is twice as long as the time needed to change from zero load to high load, see black dashed lines, which indicates the current flow velocity.

and the pressure controller should be improved. Additionally, μ PIV data are only available up to flow velocities of 3 mm/s, see fig. 2.11. Reliable recording of higher flow velocities in order to perform μ PIV analysis would require higher recording framerates, yet this is attended by a need for a more quantum-efficient camera since the fluorescence signal if the tracer particles is very low. Therefore, the development of the flow velocity can only be estimated assuming a temporal symmetry in the transition itself, i.e., the beginning and the end of the transition are similar.

Variation of hydrodynamic interactions. Since the synchronisation of the flagellar beat depends on hydrodynamic interactions, it would be interesting to test the synchronisation dynamics under different viscosity conditions. An increase in viscosity is expected to lead to a decrease of waveform amplitude and beating frequency [10, 14]. *Chlamydomonas reinhardtii* is known not to be biologically influenced by dextran, a polysaccharide made of many glucose molecules. Furthermore, dextran is available in different molecular weights, easy to handle, and thus perfectly suited for adjusting the viscosity of the background medium. It is best to use dextran with a chain length which is short enough so that there are no non-Newtonian effects, but also long enough so that the cells are not damaged due to osmotic effects [35]. Therefore, measurements at viscosities up to four times the TAP viscosity are feasible.

Influence of basal body movement on synchronisation. The synchronisation of the flagellar beat does not depend solely on hydrodynamic interactions but on basal coupling, too. It is known that the distal striated fibres can contract or elongated depending on the concentration of Ca^{2+} [113] resulting in a reduced or an increased distance of the flagella at the basal body, respectively. Alternatively, external mechanical load, applied in opposite direction to the swimming direction of the cell, can at least induce an increased flagellar distance at its base. The applied load will bend the flagella and drag them to the back of the cell. Thus, the distance between the two flagella might increase if the basal region is soft enough, i.e., if the striated fibres are not able to keep the flagellar base in place. Recent theoretical work suggests that an increase in this distance leads to a decrease in stability of in-phase synchronisation and, consequently, the coupling constant decreases [66].

Using the tracking data of the proximal end of the flagella, see sec. 3.2.1, we define the time averaged angular difference of both flagella as the flagellar distance. We assume that due to the flagella being bend back, this distance increases under load conditions if the basal region allows for some flexibility. Hence, the ability of both flagella to synchronise should decrease with increasing load, according to theoretical predictions [66] and partially to our experimental results, see sec. 3.3. Our preliminary results seem to indicate that the flagellar distance does not change under load, see fig. 4.2. However, since the error due to tracking inaccuracies or image quality is relatively large, the quality of these results is simply not good enough to reliably rule out a load-dependence of the flagellar distance.

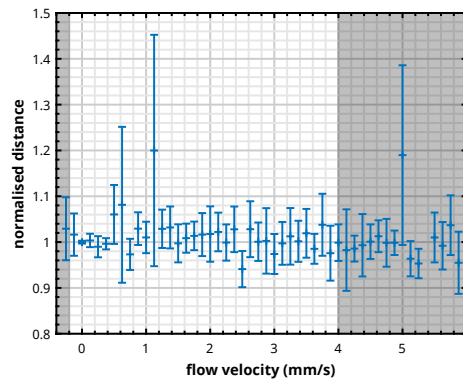


Fig. 4.2: The normalised distance of the flagellar distance (mean \pm s.e.), which is the current distance of the flagella divided by the flagellar distance under no external load, shows no dependence on the the applied load. Note that only cells whose flagella show normal beating, i.e., neither chiral beating, tremor-like beating, or stalling, were taken into account. Black shadings indicate the regions where not all flagella were beating normally, thus, less data is available here and not as reliable as in the flow region between -0.6 mm/s and 4 mm/s. In total, $n^+ = 13$ cells for positive flow rates and $n^- = 8$ cells for negative flow rates were measured.

Especially the image quality should be improved in future experiments, including a staining of the striated fibres to enhance their visibility and allow for direct determination of their length. So far, this length was determined indirectly by tracking the flagella right at the cell rim. In case staining of the fibres is not possible or if their visibility can not be guaranteed since the fluorescent markers do not shine bright enough for high-speed recordings, and indirect measurements by tracking the entire basal region is the only way, phase-contrast microscopy, in combination with higher magnification, might provide an adequate image quality.

Experiments with mutants of *Chlamydomonas reinhardtii*. One very useful feature of *C. reinhardtii* is the availability of a wide range of mutants, e.g., cells without a functioning eyespot, cells with defective striated fibres, or cells whose flagella are lacking certain dynein motors. The influence of the distal striated fibres on synchronisation could also be investigated by repeating the load response experiments with a different strain of *C. reinhardtii* with missing or defective striated fibres. The mutant *vfl-3* [138] fulfils this requirement. Without the distal striated fibres, anti-phase synchronisation should be stabilised instead of in-phase synchronisation. Other mutants are lacking different molecular motors, namely the inner dynein arms in the case of the mutant *ida3*, and the outer dynein arms in the case of the mutant *oda2*. Both mutants could be suitable to investigate the frequency response and the amplitude compliance of the flagellar beat. While *oda2* cells beat with a similar waveform than *wild type* cells but with reduced frequency [18, 59], the beating frequency of *ida3* cells is unaffected but the waveform is significantly altered [18]. Hence, both cell types might show different behaviour on external load compared to *wild type* cells, allowing to infer on the characteristics of the different dynein motor types.

Technical enhancements to the experimental setup. Regarding the experimental setup, it would be desirable to record longer sequences per flow condition. At the same time, the total number of recordable flow conditions per experimental run should be retained. Currently, we are limited to recording times of one second only. Therefore, especially in the flow range where we find dynamical switching between different beating modes, reliable statistics are impossible to determine since we most of the time only observe one mode at a time. Additionally, it would be interesting to quantify how the cell switches between these modes. Finally, not only the frequency response to external load, but also the slip dynamics and thus the coupling between the flagella could be determined in a better and more reliable way. Therefore, a camera with either increased internal memory or a camera directly streaming to a connected PC would be a reasonable upgrade to the current experimental setup.

Bibliography

- [1] J. A. ACEBRÓN, L. L. BONILLA, C. J. P. VICENTE, F. RITORT, AND R. SPIGLER, *The Kuramoto model: A simple paradigm for synchronization phenomena*, *Rev. Mod. Phys.*, 77 (2005), p. 137.
- [2] C. AINSWORTH, *Cilia: Tails of the unexpected*, *Nature*, 448 (2007), pp. 638–641.
- [3] B. ALBERTS, A. JOHNSON, J. LEWIS, M. RAFF, K. ROBERTS, AND P. WALTER, *Molecular Biology of the Cell*, Garland Science, 4th ed., 2002.
- [4] J. ALPER, V. GEYER, V. MUKUNDAN, AND J. HOWARD, *Reconstitution of Flagellar Sliding*, in *Methods in Enzymology*, vol. 524 of *Cilia*, Part A, Academic Press, Jan. 2013, pp. 343–369.
- [5] P. V. BAYLY AND K. S. WILSON, *Analysis of unstable modes distinguishes mathematical models of flagellar motion*, *J. R. Soc. Interface*, 12 (2015), p. 20150124.
- [6] R. R. BENNETT AND R. GOLESTANIAN, *A steering mechanism for phototaxis in Chlamydomonas*, *J. R. Soc. Interface*, 12 (2015).
- [7] H. C. BERG AND R. A. ANDERSON, *Bacteria Swim by Rotating their Flagellar Filaments*, *Nature*, 245 (1973), p. 245380a0.
- [8] M. BESSEN, R. B. FAY, AND G. B. WITMAN, *Calcium control of waveform in isolated flagellar axonemes of Chlamydomonas*, *J. Cell Biol.*, 86 (1980), pp. 446–455.
- [9] C. BRENNEN AND H. WINET, *Fluid mechanics of propulsion by cilia and flagella*, *Annu. Rev. Fluid Mech.*, 9 (1977), pp. 339–398.
- [10] C. J. BROKAW, *Effects of Increased Viscosity on the Move Ments of Some Invertebrate Spermatozoa*, *J. Exp. Biol.*, 45 (1966), pp. 113–139.
- [11] ———, *Adenosine Triphosphate Usage by Flagella*, *Science*, 156 (1967), pp. 76–78.
- [12] ———, *Bend Propagation by a Sliding Filament Model for Flagella*, *J. Exp. Biol.*, 55 (1971), pp. 289–304.
- [13] ———, *Flagellar Movement: A Sliding Filament Model: An explanation is suggested for the spontaneous propagation of bending waves by flagella*, *Science*, 178 (1972), pp. 455–462.
- [14] ———, *Effects of viscosity and ATP concentration on the movement of reactivated sea-urchin sperm flagella*, *J. Exp. Biol.*, 62 (1975), pp. 701–719.

- [15] ———, *Direct measurements of sliding between outer doublet microtubules in swimming sperm flagella*, *Science*, 243 (1989), pp. 1593–1596.
- [16] ———, *Microtubule sliding in swimming sperm flagella: Direct and indirect measurements on sea urchin and tunicate spermatozoa*, *J. Cell Biol.*, 114 (1991), pp. 1201–1215.
- [17] ———, *Thinking about flagellar oscillation*, *Cell Motil. Cytoskeleton*, 66 (2009), pp. 425–436.
- [18] C. J. BROKAW AND R. KAMIYA, *Bending patterns of Chlamydomonas flagella: IV. Mutants with defects in inner and outer dynein arms indicate differences in dynein arm function*, *Cell Motil. Cytoskeleton*, 8 (1987), pp. 68–75.
- [19] D. R. BRUMLEY, M. POLIN, T. J. PEDLEY, AND R. E. GOLDSTEIN, *Hydrodynamic Synchronization and Metachronal Waves on the Surface of the Colonial Alga Volvox carteri*, *Phys. Rev. Lett.*, 109 (2012).
- [20] ———, *Metachronal waves in the flagellar beating of Volvox and their hydrodynamic origin*, *J. R. Soc. Interface*, 12 (2015), p. 20141358.
- [21] D. R. BRUMLEY, K. Y. WAN, M. POLIN, AND R. E. GOLDSTEIN, *Flagellar synchronization through direct hydrodynamic interactions*, *eLife*, 3 (2014), p. e02750.
- [22] K. H. BUI, H. SAKAKIBARA, T. MOVASSAGH, K. OIWA, AND T. ISHIKAWA, *Asymmetry of inner dynein arms and inter-doublet links in Chlamydomonas flagella*, *J. Cell Biol.*, 186 (2009), pp. 437–446.
- [23] B. BUTTON, L.-H. CAI, C. EHRE, M. KESIMER, D. B. HILL, J. K. SHEEHAN, R. C. BOUCHER, AND M. RUBINSTEIN, *A Periciliary Brush Promotes the Lung Health by Separating the Mucus Layer from Airway Epithelia*, *Science*, 337 (2012), pp. 937–941.
- [24] S. CAMALET AND F. JÜLICHER, *Generic aspects of axonemal beating*, *New J. Phys.*, 2 (2000), p. 24.
- [25] R. A. CARDULLO AND J. M. BALTZ, *Metabolic regulation in mammalian sperm: Mitochondrial volume determines sperm length and flagellar beat frequency*, *Cytoskeleton*, 19 (1991), pp. 180–188.
- [26] J. H. CARTWRIGHT, O. PIRO, AND I. TUVAL, *Fluid-dynamical basis of the embryonic development of left-right asymmetry in vertebrates*, *Proc. Natl. Acad. Sci.*, 101 (2004), pp. 7234–7239.
- [27] Z. CARVALHO-SANTOS, J. AZIMZADEH, J. B. PEREIRA-LEAL, AND M. BETTENCOURT-DIAS, *Tracing the origins of centrioles, cilia, and flagella*, *J. Cell Biol.*, 194 (2011), pp. 165–175.

- [28] D. T. CHEN, M. HEYMANN, S. FRADEN, D. NICASTRO, AND Z. DOGIC, *ATP Consumption of Eukaryotic Flagella Measured at a Single-Cell Level*, *Biophys. J.*, 109 (2015), pp. 2562–2573.
- [29] V. CRASTAN, *Elektrische Energieversorgung 2*, Springer Berlin Heidelberg, Berlin, Heidelberg, 2nd ed., 2008.
- [30] S. K. DUTCHER AND E. T. O'TOOLE, *The basal bodies of Chlamydomonas reinhardtii*, *Cilia*, 5 (2016).
- [31] J. ELGETI AND G. GOMPPER, *Emergence of metachronal waves in cilia arrays*, *Proc. Natl. Acad. Sci.*, 110 (2013), pp. 4470–4475.
- [32] J. ELGETI, R. G. WINKLER, AND G. GOMPPER, *Physics of microswimmers—single particle motion and collective behavior: A review*, *Rep. Prog. Phys.*, 78 (2015), p. 056601.
- [33] B. FRIEDRICH, *Hydrodynamic synchronization of flagellar oscillators*, *Eur. Phys. J. Spec. Top.*, 225 (2016), pp. 2353–2368.
- [34] B. M. FRIEDRICH AND F. JÜLICHER, *Flagellar Synchronization Independent of Hydrodynamic Interactions*, *Phys. Rev. Lett.*, 109 (2012).
- [35] M. GARCIA, S. BERTI, P. PEYLA, AND S. RAFAÏ, *Random walk of a swimmer in a low-Reynolds-number medium*, *Phys. Rev. E*, 83 (2011).
- [36] V. F. GEYER, F. JÜLICHER, J. HOWARD, AND B. M. FRIEDRICH, *Cell-body rocking is a dominant mechanism for flagellar synchronization in a swimming alga*, *Proc. Natl. Acad. Sci.*, 110 (2013), pp. 18058–18063.
- [37] V. F. GEYER, P. SARTORI, B. M. FRIEDRICH, F. JÜLICHER, AND J. HOWARD, *Independent Control of the Static and Dynamic Components of the Chlamydomonas Flagellar Beat*, *Curr. Biol.*, 26 (2016), pp. 1098–1103.
- [38] I. R. GIBBONS, *The relationship between the fine structure and direction of beat in gill cilia of a lamellibranch mollusc*, *J. Biophys. Biochem. Cytol.*, 11 (1961), pp. 179–205.
- [39] R. GOLDSTEIN, M. POLIN, AND I. TUVAL, *Noise and Synchronization in Pairs of Beating Eukaryotic Flagella*, *Phys. Rev. Lett.*, 103 (2009).
- [40] R. E. GOLDSTEIN, M. POLIN, AND I. TUVAL, *Emergence of Synchronized Beating during the Regrowth of Eukaryotic Flagella*, *Phys. Rev. Lett.*, 107 (2011).
- [41] R. GOLESTANIAN, J. M. YEOMANS, AND N. UCHIDA, *Hydrodynamic synchronization at low Reynolds number*, *Soft Matter*, 7 (2011), p. 3074.

- [42] D. S. GORMAN AND R. P. LEVINE, *Cytochrome f and plastocyanin: Their sequence in the photosynthetic electron transport chain of Chlamydomonas reinhardi*, Proc. Natl. Acad. Sci., 54 (1965), pp. 1665–1669.
- [43] J. GRAY, *Ciliary Movement*, Cambridge University Press, 1928.
- [44] J. GRAY AND G. J. HANCOCK, *The propulsion of sea-urchin spermatozoa*, J. Exp. Biol., 32 (1955), pp. 802–814.
- [45] S. GUERON AND K. LEVIT-GUREVICH, *Energetic considerations of ciliary beating and the advantage of metachronal coordination*, Proc. Natl. Acad. Sci., 96 (1999), pp. 12240–12245.
- [46] B. GUIRAO AND J.-F. JOANNY, *Spontaneous Creation of Macroscopic Flow and Metachronal Waves in an Array of Cilia*, Biophys. J., 92 (2007), pp. 1900–1917.
- [47] A. HALLMANN, *Extracellular Matrix and Sex-Inducing Pheromone in Volvox*, in International Review of Cytology, vol. 227, Elsevier, 2003, pp. 131–182.
- [48] P. HÄNGGI, P. TALKNER, AND M. BORKOVEC, *Reaction-rate theory: Fifty years after Kramers*, Rev. Mod. Phys., 62 (1990), pp. 251–341.
- [49] D. B. HILL, V. SWAMINATHAN, A. ESTES, J. CRIBB, E. T. O'BRIEN, C. W. DAVIS, AND R. SUPERFINE, *Force Generation and Dynamics of Individual Cilia under External Loading*, Biophys. J., 98 (2010), pp. 57–66.
- [50] J. A. HOLLM, R. P. KHAN, E. N. MARONGELLI, AND W. H. GUILFORD, *Laser Trap Characterization and Modeling of Phototaxis in Chlamydomonas reinhardtii*, Cell. Mol. Bioeng., 2 (2009), pp. 244–254.
- [51] J. P. HOLMAN, *Heat Transfer*, McGraw-Hill series in mechanical engineering, McGraw-Hill Higher Education, Boston, 10th ed., 2010.
- [52] H. J. HOOPS, R. L. WRIGHT, J. W. JARVIK, AND G. B. WITMAN, *Flagellar waveform and rotational orientation in a Chlamydomonas mutant lacking normal striated fibers*, J. Cell Biol., 98 (1984), pp. 818–824.
- [53] J. HOWARD, *Mechanics of Motor Proteins and the Cytoskeleton*, in Mechanics of Motor Proteins and the Cytoskeleton, Sinauer Associates Inc., U.S., 2001, p. 384.
- [54] J. S. HYAMS AND G. G. BORISY, *Flagellar coordination in Chlamydomonas reinhardtii: Isolation and reactivation of the flagellar apparatus*, Science, 189 (1975), pp. 891–893.
- [55] I. IBANEZ-TALLON, *To beat or not to beat: Roles of cilia in development and disease*, Hum. Mol. Genet., 12 (2003), pp. 27R–35.

- [56] A. W. JAY, *Viscoelastic properties of the human red blood cell membrane: I. Deformation, volume loss, and rupture of red cells in micropipettes*, *Biophys. J.*, 13 (1973), pp. 1166–1182.
- [57] F. JÜLICHER AND J. PROST, *Spontaneous Oscillations of Collective Molecular Motors*, *Phys. Rev. Lett.*, 78 (1997), pp. 4510–4513.
- [58] A. KAGE, C. HOSOYA, S. A. BABA, AND Y. MOGAMI, *Drastic reorganization of the bioconvection pattern of Chlamydomonas: Quantitative analysis of the pattern transition response*, *J. Exp. Biol.*, 216 (2013), pp. 4557–4566.
- [59] R. KAMIYA, *Exploring the function of inner and outer dynein arms with Chlamydomonas mutants*, *Cytoskeleton*, 32 (1995), pp. 98–102.
- [60] R. KAMIYA AND G. B. WITMAN, *Submicromolar levels of calcium control the balance of beating between the two flagella in demembrated models of Chlamydomonas*, *J. Cell Biol.*, 98 (1984), pp. 97–107.
- [61] Y. KATSU-KIMURA, F. NAKAYA, S. A. BABA, AND Y. MOGAMI, *Substantial energy expenditure for locomotion in ciliates verified by means of simultaneous measurement of oxygen consumption rate and swimming speed*, *J. Exp. Biol.*, 212 (2009), pp. 1819–1824.
- [62] R. D. KEANE AND R. J. ADRIAN, *Theory of cross-correlation analysis of PIV images*, *Appl. Sci. Res.*, 49 (1992), pp. 191–215.
- [63] M. KIM AND T. R. POWERS, *Hydrodynamic interactions between rotating helices*, *Phys. Rev. E*, 69 (2004).
- [64] G. S. KLINDT, *Hydrodynamics of Flagellar Swimming and Synchronization*, PhD thesis, Technische Universität, Dresden, 2017.
- [65] G. S. KLINDT, C. RULOFF, C. WAGNER, AND B. M. FRIEDRICH, *Load Response of the Flagellar Beat*, *Phys. Rev. Lett.*, 117 (2016).
- [66] G. S. KLINDT, C. RULOFF, C. WAGNER, AND B. M. FRIEDRICH, *In-phase and anti-phase flagellar synchronization by waveform compliance and basal coupling*, *New J. Phys.*, 19 (2017), p. 113052.
- [67] J. KOTAR, M. LEONI, B. BASSETTI, M. C. LAGOMARSINO, AND P. CICUTA, *Hydrodynamic synchronization of colloidal oscillators*, *Proc. Natl. Acad. Sci.*, 107 (2010), pp. 7669–7673.
- [68] B. KRALEMANN, L. CIMPONERIU, M. ROSENBLUM, A. PIKOVSKY, AND R. MROWKA, *Phase dynamics of coupled oscillators reconstructed from data*, *Phys. Rev. E*, 77 (2008).

- [69] M. KRYUCHKOVA, A. DANILUSHKINA, Y. LVOV, AND R. FAKHRULLIN, *Evaluation of toxicity of nanoclays and graphene oxide in vivo: A Paramecium caudatum study*, *Environ. Sci. Nano*, 3 (2016), pp. 442–452.
- [70] Y. KURAMOTO, *Chemical Oscillations, Waves and Turbulence*, in *Chemical Oscillations, Waves and Turbulence*, Springer, Berlin, 1984, pp. 75–76.
- [71] E. LAUGA AND T. R. POWERS, *The hydrodynamics of swimming microorganisms*, *Rep. Prog. Phys.*, 72 (2009), p. 096601.
- [72] P. P. LELE, B. G. HOSU, AND H. C. BERG, *Dynamics of mechanosensing in the bacterial flagellar motor*, *Proc. Natl. Acad. Sci.*, 110 (2013), pp. 11839–11844.
- [73] K. C. LEPTOS, K. Y. WAN, M. POLIN, I. TUVAL, A. I. PESCI, AND R. E. GOLDSTEIN, *Antiphase Synchronization in a Flagellar-Dominance Mutant of Chlamydomonas*, *Phys. Rev. Lett.*, 111 (2013).
- [74] C. B. LINDEMANN, *A "Geometric Clutch" Hypothesis to Explain Oscillations of the Axoneme of Cilia and Flagella*, *J. Theor. Biol.*, 168 (1994), pp. 175–189.
- [75] ———, *A model of flagellar and ciliary functioning which uses the forces transverse to the axoneme as the regulator of dynein activation*, *Cell Motil. Cytoskeleton*, 29 (1994), pp. 141–154.
- [76] R. LINDKEN, M. ROSSI, S. GROSSE, AND J. WESTERWEEL, *Micro-Particle Image Velocimetry (μ PIV): Recent developments, applications, and guidelines*, *Lab. Chip*, 9 (2009), p. 2551.
- [77] R. LYONS, E. SARIDOGAN, AND O. DJAHANBAKHCH, *The reproductive significance of human Fallopian tube cilia*, *Hum. Reprod. Update*, 12 (2006), pp. 363–372.
- [78] R. MA, G. S. KLINDT, I. H. RIEDEL-KRUSE, F. JÜLICHER, AND B. M. FRIEDRICH, *Active Phase and Amplitude Fluctuations of Flagellar Beating*, *Phys. Rev. Lett.*, 113 (2014).
- [79] K. E. MACHIN, *Wave propagation along flagella*, *J. Exp. Biol.*, 35 (1958), pp. 796–806.
- [80] W. F. MARSHALL AND S. NONAKA, *Cilia: Tuning in to the Cell's Antenna*, *Curr. Biol.*, 16 (2006), pp. R604–R614.
- [81] G. I. MCFADDEN, D. SCHULZE, B. SUREK, J. L. SALISBURY, AND M. MELKONIAN, *Basal body reorientation mediated by a Ca^{2+} -modulated contractile protein*, *J. Cell Biol.*, 105 (1987), pp. 903–912.
- [82] D. R. MITCHELL, *Chlamydomonas flagella*, *J. Phycol.*, 36 (2000), pp. 261–273.
- [83] ———, *The evolution of eukaryotic cilia and flagella as motile and sensory organelles*, in *Eukaryotic Membranes and Cytoskeleton*, Springer, 2007, pp. 130–140.

- [84] Y. MORITA AND C. SHINGYOJI, *Effects of Imposed Bending on Microtubule Sliding in Sperm Flagella*, *Curr. Biol.*, 14 (2004), pp. 2113–2118.
- [85] N. NAREMATSU, R. QUEK, K.-H. CHIAM, AND Y. IWADATE, *Ciliary metachronal wave propagation on the compliant surface of Paramecium cells*, *Cytoskeleton*, 72 (2015), pp. 633–646.
- [86] N. NATARAJAN AND M. LAKSHMANAN, *Laminar flow in rectangular ducts: Prediction of velocity profiles and friction factor*, 10 (1972), pp. 435–438.
- [87] D. NICASTRO, C. SCHWARTZ, J. PIERSON, R. GAUDETTE, M. E. PORTER, AND J. R. MCINTOSH, *The Molecular Architecture of Axonemes Revealed by Cryoelectron Tomography*, *Science*, 313 (2006), pp. 944–948.
- [88] T. NIEDERMAYER, B. ECKHARDT, AND P. LENZ, *Synchronization, phase locking, and metachronal wave formation in ciliary chains*, *Chaos Interdiscip. J. Nonlinear Sci.*, 18 (2008), p. 037128.
- [89] S. NONAKA, H. SHIRATORI, Y. SAJIOH, AND H. HAMADA, *Determination of left–right patterning of the mouse embryo by artificial nodal flow*, *Nature*, 418 (2002), pp. 96–99.
- [90] S. NONAKA, Y. TANAKA, Y. OKADA, S. TAKEDA, A. HARADA, Y. KANAI, M. KIDO, AND N. HIROKAWA, *Randomization of left–right asymmetry due to loss of nodal cilia generating leftward flow of extraembryonic fluid in mice lacking KIF3B motor protein*, *Cell*, 95 (1998), pp. 829–837.
- [91] H. M. OLIVEIRA AND L. V. MELO, *Huygens synchronization of two clocks*, *Sci. Rep.*, 5 (2015).
- [92] C. K. OMOTO AND C. KUNG, *The pair of central tubules rotates during ciliary beat in Paramecium*, *Nature*, 279 (1979), pp. 532–534.
- [93] N. OSTERMAN AND A. VILFAN, *Finding the ciliary beating pattern with optimal efficiency*, *Proc. Natl. Acad. Sci.*, 108 (2011), pp. 15727–15732.
- [94] J. PANTALEONE, *Synchronization of metronomes*, *Am. J. Phys.*, 70 (2002), pp. 992–1000.
- [95] G. J. PAZOUR, N. AGRIN, J. LESZYK, AND G. B. WITMAN, *Proteomic analysis of a eukaryotic cilium*, *J. Cell Biol.*, 170 (2005), pp. 103–113.
- [96] G. J. PAZOUR, O. A. SINESHCHEKOV, AND G. B. WITMAN, *Mutational analysis of the phototransduction pathway of *Chlamydomonas reinhardtii**, *J. Cell Biol.*, 131 (1995), pp. 427–440.
- [97] A. PIKOVSKY, M. ROSENBLUM, AND J. KURTHS, *Synchronization: A Universal Concept in Nonlinear Sciences*, vol. 12, Cambridge university press, 2003.

- [98] J. R. PLATT, "Bioconvection Patterns" in *Cultures of Free-Swimming Organisms*, Science, 133 (1961), pp. 1766–1767.
- [99] M. POLIN, I. TUVAL, K. DRESCHER, J. P. GOLLUB, AND R. E. GOLDSTEIN, *Chlamydomonas Swims with Two "Gears" in a Eukaryotic Version of Run-and-Tumble Locomotion*, Science, 325 (2009), pp. 487–490.
- [100] K. POLOTZEK AND B. M. FRIEDRICH, *A three-sphere swimmer for flagellar synchronization*, New J. Phys., 15 (2013), p. 045005.
- [101] E. M. PURCELL, *Life at low Reynolds number*, Am. J. Phys., 45 (1977), pp. 3–11.
- [102] H. F. P. PURDAY, *Streamline Flow: An Introduction to the Mechanics of Viscous Flow, Film Lubrication, the Flow of Heat by Conduction, and Heat Transfer by Convection*, Dover, New York, United States, 1949.
- [103] G. QUARANTA, M.-E. AUBIN-TAM, AND D. TAM, *Hydrodynamics Versus Intracellular Coupling in the Synchronization of Eukaryotic Flagella*, Phys. Rev. Lett., 115 (2015).
- [104] M. REICHERT AND H. STARK, *Synchronization of rotating helices by hydrodynamic interactions*, Eur. Phys. J. E, 17 (2005), pp. 493–500.
- [105] I. H. RIEDEL-KRUSE, A. HILFINGER, J. HOWARD, AND F. JÜLICHER, *How molecular motors shape the flagellar beat*, HFSP J., 1 (2007), pp. 192–208.
- [106] D. L. RINGO, *Flagellar motion and fine structure of the flagellar apparatus in Chlamydomonas*, J. Cell Biol., 33 (1967), pp. 543–571.
- [107] U. RÜFFER AND W. NULTSCH, *High-speed cinematographic analysis of the movement of Chlamydomonas*, Cell Motil., 5 (1985), pp. 251–263.
- [108] ———, *Comparison of the beating of cis- and trans-flagella of Chlamydomonas cells held on micropipettes*, Cell Motil. Cytoskeleton, 7 (1987), pp. 87–93.
- [109] ———, *Flagellar photoresponses of Chlamydomonas cells held on micropipettes: I. Change in flagellar beat frequency*, Cell Motil. Cytoskeleton, 15 (1990), pp. 162–167.
- [110] ———, *Flagellar photoresponses of ptx1, a nonphototactic mutant of Chlamydomonas*, Cell Motil. Cytoskeleton, 37 (1997), pp. 111–119.
- [111] ———, *Flagellar coordination in Chlamydomonas cells held on micropipettes*, Cell Motil. Cytoskeleton, 41 (1998), pp. 297–307.
- [112] J. L. SALISBURY AND G. L. FLOYD, *Calcium-Induced Contraction of the Rhizoplast of a Quadriflagellate Green Alga*, Science, 202 (1978), pp. 975–977.

- [113] J. L. SALISBURY, M. A. SANDERS, AND L. HARPST, *Flagellar root contraction and nuclear movement during flagellar regeneration in Chlamydomonas reinhardtii*, *J. Cell Biol.*, 105 (1987), pp. 1799–1805.
- [114] M. J. SANDERSON AND M. A. SLEIGH, *Ciliary activity of cultured rabbit tracheal epithelium: Beat pattern and metachrony*, *J. Cell Sci.*, 47 (1981), pp. 331–347.
- [115] P. SARTORI, V. F. GEYER, J. HOWARD, AND F. JÜLICHER, *Curvature regulation of the ciliary beat through axonemal twist*, *Phys. Rev. E*, 94 (2016).
- [116] P. SARTORI, V. F. GEYER, A. SCHOLICH, F. JÜLICHER, AND J. HOWARD, *Dynamic curvature regulation accounts for the symmetric and asymmetric beats of Chlamydomonas flagella*, *eLife*, 5 (2016), p. e13258.
- [117] P. SATIR, *Studies on Cilia: II. Examination of the Distal Region of the Ciliary Shaft and the Role of the Filaments in Motility*, *J. Cell Biol.*, 26 (1965), pp. 805–834.
- [118] P. SATIR AND T. MATSUOKA, *Splitting the ciliary axoneme: Implications for a “Switch-Point” model of dynein arm activity in ciliary motion*, *Cell Motil. Cytoskeleton*, 14 (1989), pp. 345–358.
- [119] K. A. SCHMITZ, D. L. HOLCOMB-WYGLE, D. J. OBERSKI, AND C. B. LINDEMANN, *Measurement of the force produced by an intact bull sperm flagellum in isometric arrest and estimation of the dynein stall force*, *Biophys. J.*, 79 (2000), pp. 468–478.
- [120] J. W. SHAEVITZ, J. Y. LEE, AND D. A. FLETCHER, *Spiroplasma Swim by a Processive Change in Body Helicity*, *Cell*, 122 (2005), pp. 941–945.
- [121] S. C. STRALEY AND V. G. BRUCE, *Stickiness to glass circadian changes in the cell surface of Chlamydomonas reinhardi*, *Plant Physiol.*, 63 (1979), pp. 1175–1181.
- [122] K. E. SUMMERS AND I. R. GIBBONS, *Adenosine Triphosphate-Induced Sliding of Tubules in Trypsin-Treated Flagella of Sea-Urchin Sperm*, *Proc. Natl. Acad. Sci.*, 68 (1971), pp. 3092–3096.
- [123] J. K. SVEEN, *An introduction to MatPIV v. 1.6. 1*, Univ. Oslo Dep. Math., (2004).
- [124] B. E. TAILLON, S. A. ADLER, J. P. SUHAN, AND J. W. JARVIK, *Mutational analysis of centrin: An EF-hand protein associated with three distinct contractile fibers in the basal body apparatus of Chlamydomonas*, *J. Cell Biol.*, 119 (1992), pp. 1613–1624.
- [125] S. G. TAYLOR, F. R. S., *Analysis of the swimming of microscopic organisms*, *Proc. R. Soc. Lond. A*, 209 (1951), pp. 447–461.
- [126] M. THEERS AND R. G. WINKLER, *Synchronization of rigid microrotors by time-dependent hydrodynamic interactions*, *Phys. Rev. E*, 88 (2013).

- [127] M. J. TIPPING, N. J. DELALEZ, R. LIM, R. M. BERRY, AND J. P. ARMITAGE, *Load-dependent assembly of the bacterial flagellar motor*, *mBio*, 4 (2013).
- [128] N. UCHIDA AND R. GOLESTANIAN, *Generic Conditions for Hydrodynamic Synchronization*, *Phys. Rev. Lett.*, 106 (2011).
- [129] A. VILFAN AND F. JÜLICHER, *Hydrodynamic Flow Patterns and Synchronization of Beating Cilia*, *Phys. Rev. Lett.*, 96 (2006), p. 058102.
- [130] H. WAGER, *On the Effect of Gravity upon the Movements and Aggregation of Euglena viridis, Ehrb., and Other Micro-Organisms*, *Philos. Trans. R. Soc. Lond. B Biol. Sci.*, 201 (1911), pp. 333–390.
- [131] K. Y. WAN AND R. E. GOLDSTEIN, *Rhythmicity, Recurrence, and Recovery of Flagellar Beating*, *Phys. Rev. Lett.*, 113 (2014).
- [132] ———, *Coordinated beating of algal flagella is mediated by basal coupling*, *Proc. Natl. Acad. Sci.*, 113 (2016), pp. E2784–E2793.
- [133] S. WERNER, J. C. RINK, I. H. RIEDEL-KRUSE, AND B. M. FRIEDRICH, *Shape Mode Analysis Exposes Movement Patterns in Biology: Flagella and Flatworms as Case Studies*, *PLoS ONE*, 9 (2014), p. e113083.
- [134] F. M. WHITE, *Viscous Fluid Flow*, McGraw-Hill, Jan. 1991.
- [135] ———, *Fluid Mechanics*, McGraw-Hill, 2003.
- [136] D. M. WOOLLEY, R. F. CROCKETT, W. D. I. GROOM, AND S. G. REVELL, *A study of synchronisation between the flagella of bull spermatozoa, with related observations*, *J. Exp. Biol.*, 212 (2009), pp. 2215–2223.
- [137] W. C. WORTHINGTON AND R. S. CATHCART, *Ependymal Cilia: Distribution and Activity in the Adult Human Brain*, *Science*, 139 (1963), pp. 221–222.
- [138] R. L. WRIGHT, B. CHOJNACKI, AND J. W. JARVIK, *Abnormal basal-body number, location, and orientation in a striated fiber-defective mutant of Chlamydomonas reinhardtii*, *J. Cell Biol.*, 96 (1983), pp. 1697–1707.
- [139] X. ZHENG AND Z.-H. SILBER-LI, *Measurement of velocity profiles in a rectangular microchannel with aspect ratio $\alpha = 0.35$* , *Exp. Fluids*, 44 (2008), pp. 951–959.

List of used materials and devices

- ▷ ***Chlamydomonas reinhardtii* SAG 11-32c mt- (wild type):** SAG is the acronym for “Sammlung von Algenkulturen” of Göttingen University, 11-32c stands for the strain number, and mt- denotes negative mating type.
- ▷ **Compact fluorescent lamp:** Müller Licht, 11 W, 2700 K, 630 lm
- ▷ **Microscope:** Nikon TE2000-S
- ▷ **Red light illumination:** Zett Optics ZLED CLS 9000 MV-R, $\lambda = 640 \text{ nm} \pm 20 \text{ nm}$
- ▷ **White light illumination:** Schott KL 2500 LCD
- ▷ **Objective:** Nikon Plan Apo VC 60 \times , NA 1.4
- ▷ **High-speed camera:** Fastec HiSpec 1, memory: 2 GB, chip size: 1280 px \times 1024 px, pixel size: 14 μm \times 14 μm
- ▷ **Micropipettes:** World Precision Instruments Ltd., TIP2TW1, average tip diameter: 2 $\mu\text{m} \pm 20\%$
- ▷ **MicroFil:** World Precision Instruments Ltd., MF34G-5, length: 67 mm, inner diameter: 100 μm , outer diameter: 164 μm , gauge: 34
- ▷ **Piezo stages:** Physik Instrumente GmbH & Co. KG, P-622.1CD and P-622.ZCD
- ▷ **Piezo controller:** Physik Instrumente GmbH & Co. KG, E-665 (used with P-622.1CD) and E-509.X3 (used with P-622.ZCD)
- ▷ **Pressure controller:** Elvsys[®] Elveflow OB1-MkII, 2 bar maximum pressure, 0.005% pressure stability, 9 ms response time, 40 ms settling time
- ▷ **Damping table:** Accurion Halcyonics Vario
- ▷ **Microcontroller:** Arduino[®] Mega 2560 and Adafruit Industries LLC Motor/Step-per/Servo Shield for Arduino[®] v2
- ▷ **Tubings:** Deutsch & Neumann #355 0501, inner diameter: 0.5 mm, outer diameter: 1 mm, polyethylene
- ▷ **Microfluidics high resolution film mask:** Micro Lithography Services Ltd., 102 Haltwhistle Road, South Woodham Ferrers, Chelmsford, Essex, CM3 5ZF, microlitho.co.uk
- ▷ **Tracer particles:** Sigma Aldrich L3280-1ML, carboxylate-modified polystyrene beads, fluorescent red ($\lambda_{ex} \approx 575 \text{ nm}$, $\lambda_{em} \approx 610 \text{ nm}$), average diameter: 0.5 μm , aqueous suspension, 2.5% solids

Acknowledgement

First of all, I want to thank Prof. Dr. Christian Wagner for giving me the opportunity to work on this fascinating topic in a great and supporting atmosphere. Albeit the scientific work was not always easy and sometimes a bit frustrating, he supported me all the time and gave me the confidence to continue.

Additionally, I want to thank our collaborators Dr. Benjamin M. Friedrich and Dr. Gary S. Klindt for the great work, fruitful discussions, and—until now—two publications.

In experimental physics, there is also some technical work involved. Therefore, I want to thank all members of our precision tool shop under the supervision of Michael Schmitt. I do not know how often you guys fabricated adaptors, rails, and more for me despite some “minimal” conceptional inaccuracies from my side. Furthermore, I want to thank our electrician Stefan Loew who helped me a lot with all the wiring, soldering, and everything else related to electrics.

Since growing algae highly depends on the skills of the experimentalist in a biology lab, I want to thank Karin Kretsch for maintaining my cultures, and all the cheerful disappointments we faced in the lab.

The current and former members of the Wagner group as well as our secretary Elke Huschens shall not remain unnamed. Thank you very much for all the fun we had in the last years.

Talking about fun, my time at the university was great not despite but because of all my new friends. I do not want to make you feel upset due to the order of mentioning—and since there is not enough space to mention all of you—feel free to insert your name here.

Carsten, Denis, Dominic, Dominik, Sebastian, and Manu—we had a blast.

I also want to thank my entire family for their constant support and help. Thank you very much.

Special thanks to the proofreaders who do not want to be mentioned explicitly due to their fear of having missed something.

Last but not least, I want to thank you, Julia, for your ongoing support, everlasting motivation, and simply everything—you are the love of my life.

